

An Investigation of the Aryl and Methyl  
CH Stretching Overtones of Substituted  
Benzenes and Aromatic Heterocycles  
Using Absorption and Photoacoustic Spectroscopy

A thesis presented to the University of Manitoba  
in partial fulfillment of the requirements for the  
degree of Ph. D.

by

Michael G. Sowa

Department of Chemistry

University of Manitoba

Winnipeg, Manitoba

(C) Copyrite by Michael G. Sowa, 1990.



National Library  
of Canada

Bibliothèque nationale  
du Canada

Canadian Theses Service    Service des thèses canadiennes

Ottawa, Canada  
K1A 0N4

The author has granted an irrevocable non-exclusive licence allowing the National Library of Canada to reproduce, loan, distribute or sell copies of his/her thesis by any means and in any form or format; making this thesis available to interested persons.

The author retains ownership of the copyright in his/her thesis. Neither the thesis nor substantial extracts from it may be printed or otherwise reproduced without his/her permission.

L'auteur a accordé une licence irrévocable et non exclusive permettant à la Bibliothèque nationale du Canada de reproduire, prêter, distribuer ou vendre des copies de sa thèse de quelque manière et sous quelque forme que ce soit pour mettre des exemplaires de cette thèse à la disposition des personnes intéressées.

L'auteur conserve la propriété du droit d'auteur qui protège sa thèse. Ni la thèse ni des extraits substantiels de celle-ci ne doivent être imprimés ou autrement reproduits sans son autorisation.

ISBN 0-315-63378-6

Canada

**AN INVESTIGATION OF THE ARYL AND METHYL CH STRETCHING  
OVERTONES OF SUBSTITUTED BENZENES AND AROMATIC  
HETEROCYCLES USING ABSORPTION AND PHOTOACOUSTIC SPECTROSCOPY**

**BY**

**MICHAEL G. SOWA**

A thesis submitted to the Faculty of Graduate Studies of  
the University of Manitoba in partial fulfillment of the requirements  
of the degree of

**DOCTOR OF PHILOSOPHY**

**© 1990**

Permission has been granted to the LIBRARY OF THE UNIVER-  
SITY OF MANITOBA to lend or sell copies of this thesis, to  
the NATIONAL LIBRARY OF CANADA to microfilm this  
thesis and to lend or sell copies of the film, and UNIVERSITY  
MICROFILMS to publish an abstract of this thesis.

The author reserves other publication rights, and neither the  
thesis nor extensive extracts from it may be printed or other-  
wise reproduced without the author's written permission.

## ABSTRACT

Three aspects of vibrational overtone spectroscopy are presented. The first aspect discusses instrumental developments. In particular, the construction of an automated intracavity dye laser photoacoustic spectrometer is detailed. The increased sensitivity of photoacoustic spectroscopy (PAS) over conventional absorption methods enables the very weak, high vibrational overtone regions of molecules in the gas phase to be studied. This enhanced capability provided by PAS is exploited throughout these investigations.

The aryl CH stretching overtone spectra of a number of 5-membered aromatic heterocycles were examined. Most of the spectral features can be understood in terms of a zero order local mode assignment. Substituent effects on the aryl CH stretching regions of the aromatic heterocycles were found to be similar to the effects observed in substituted benzenes. Halogens increase the aryl CH stretching frequency of neighbouring oscillators while methyl substituents have the opposite effect on the aryl CH stretching overtones.

At the third overtone ( $\Delta\nu_{\text{CH}} = 4$ ) of furan the distinct overtone transitions arising from the structurally nonequivalent aryl CH oscillators coalesce. The coalescence of overtone features can be explained by the near resonance of the zero order overtone levels with nearby "door-way" states. This coalescence is consistent with a "diffuse" IVR (intramolecular

vibrational energy redistribution) interpretation. Unlike furan, thiophene exhibits features at  $\Delta\nu_{\text{CH}} = 3$  and 5 similar to Fermi resonances observed in the low density of states regime. These overtone Fermi resonances are sensitive to the resonance condition and can be tuned through substitution on the thiophene ring. The sensitivity of these resonances clearly shows certain states are more effectively coupled to the overtone state. This is consistent with the idea of "door-way" states in IVR models. However the data suggests that, initially at least, IVR is mode-specific as opposed to being a "diffuse" interaction.

The final aspect of the study concerns the methyl CH stretching overtone regions of low barrier, methyl rotor molecules. Previous experimental results suggested the simultaneous presence of the "frozen-out" and the rotationally averaged methyl conformers. A central peak which has been assigned to the "averaged" conformer is observable in the  $\Delta\nu_{\text{CH}} \geq 3$  regions of most of the low barrier molecules studied. However, several very important exceptions are discovered. The most notable exceptions are 2-butyne, pentafluorotoluene, and 2,3,5,6 tetrafluorotoluene. The usually narrow linewidths encountered in these molecules resolves additional structure not observed in the spectra of the other methyl rotor systems. Previously unnoticed is the presence of a weak central peak in the ortho substituted toluenes and methylfurans. This peak grows in intensity and becomes clearly resolved at the  $\Delta\nu_{\text{CH}}=5$  overtone region. With the exception

of the central peak, the high overtone spectra  $\Delta\nu_{\text{CH}} \geq 3$  have a structural interpretation. In molecules like neopentane the spectra can be understood in terms of a rigid methyl group with local  $C_{3v}$  symmetry. However the methyl substituted furans, thiophenes, pyridines, and benzenes are best described by a  $C_{2v}$  methyl group symmetry which acknowledges the conformational nonequivalence of the methyl CH oscillators. At  $\Delta\nu_{\text{CH}}=2$  the spectra of the various methyl rotors converge, neither the  $C_{2v}$  nor  $C_{3v}$  limits seem to rigorously hold. This is interpreted as a breakdown of the rigid methyl group approximation.

## List of Publications

- 1.) Henry B. R. and Sowa M. G., "Intracavity Dye Laser Photoacoustic Spectroscopy and its Application to High Energy Vibrational Overtone Spectra", *Prog. analyt. Spec.* **12**,349,(1989).
- 2.) Henry B. R., Gough K. M., and Sowa M. G., "The Application of Overtone Spectroscopy to Investigation of Carbon-Hydrogen Bond Lengths and Molecular Conformations", *Int. Rev. Phys. Chem.* **5**,133,(1986).

## Acknowledgements

There are many people who made my time as a graduate student most enjoyable and scientifically highly stimulating. I would like to thank some of them here.

First of all I thank my parents, George and Irene, for their constant support and encouragement. I'd also like to thank Leslie Lockhart for her understanding and devotion.

I'd sincerely like to thank Dr. Bryan Henry for his guidance and patience through my graduate work. I'd also like to thank my advisory committee Dr. Schaefer, Dr. Hunter, and Dr. Woods. I also thank Dr. Bernstein for his efforts.

I was indeed fortunate through my graduate program to have worked with Allan Tarr, Kathy Gough, Wayne Buchanon, Khalique Ahmed, David Swanton, Eric Sweinson, Prabhat Goswami, and Yoshiro Mizugai.

I would also like to acknowledge some people whose direct technical contributions made my research possible. I thank Ian Ward for constructing our various photoacoustic cells, Wayne Buchanon for his help with the dye lasers and electronics, Kirk Marat and Allan Tarr for their help with the Nicolet 1280, and Rudy Sebastian for all

his help with the Amdahl mainframe and M.O. calculations.

I am grateful for the financial assistance of postgraduate fellowships which were provided by the Natural Sciences and Engineering Research Council of Canada, and later, by the University of Manitoba.

## Table of Contents

### PART A : INTRODUCTION

#### CHAPTER 1 : Descriptions of Molecular Vibration

- Molecular Vibrations and Our Picture of the Molecule 2
- i.) The Normal Mode Model 5
- ii.) The Zero Order Local Mode Description 16
- iii.) Harmonic Coupling Schemes in the Local Mode Model 27

#### CHAPTER 2 : Introduction to the Problem 37

Table of Contents (cont'd)

**PART B : EXPERIMENTAL**

<b>CHAPTER 3 :</b>	<b>Samples and Sample Handling</b>	<b>44</b>
i.)	Materials	44
ii.)	Sample Preparation	44
<b>CHAPTER 4 :</b>	<b>Conventional Absorption Spectrometers</b>	<b>50</b>
i.)	FTIR	50
ii.)	Beckman	51
<b>CHAPTER 5 :</b>	<b>Intracavity Dye Laser Vibrational Overtone Photoacoustic Spectroscopy</b>	<b>57</b>
i.)	Introduction to Photoacoustic Spectroscopy (PAS)	57
ii.)	Overview of the Analysis of Amplitude Modulated, Continuous Wave PAS.	67
iii.)	PAS Laser System	75
iv.)	PA Cell Design	87
v.)	PA Detection Scheme	101
vi.)	PA Spectrometer Performance	111

Table of Contents (cont'd)

<b>CHAPTER 6 : PA Instrument Control and Data Acquisition</b>	122
i.) Description of the GPIB-IEEE 488 Bus	122
ii.) GPIB-IEEE 488 Photoacoustic Configuration	131
iii.) PAS Control and Acquisition Software	149
<b>CHAPTER 7 : Photoacoustic Data Analysis Software</b>	158
i.) Data Transfer and Rudimentary Data	160
Processing in the Filter Angle Domain	
ii.) Wavelength Calibration Procedures	168
iii.) PA Data Calibration and BECKMA Conversion Routines	175
<b>CHAPTER 8 : Molecular Orbital Calculations</b>	181
i.) Geometry Optimizations	182
ii.) Torsional Potentials	184
iii.) Vibrational Force Fields	185
iv.) Dipole Moment Derivatives and Overtone Intensity	191
Calculations	

Table of Contents (cont'd)

**PART C : VIBRATIONAL OVERTONE STUDY OF  
5-MEMBERED AROMATIC HETEROCYCLES**

<b>CHAPTER 9</b>	<b>: Zero Order Interpretations of the Aryl CH- Stretching Spectral Regions of Aromatic Heterocycles</b>	<b>196</b>
i.)	The Zero Order Local Mode Assignment	196
ii.)	Substituent Effects on Local Mode Parameters	242
iii.)	Bondlength-Frequency Correlations	258
<b>CHAPTER 10</b>	<b>: Local Mode Dynamics of the Aromatic Heterocycles</b>	<b>269</b>
i.)	Deviations from Zero Order Local Mode Predictions	269
ii.)	Fermi Resonance and Intramolecular Vibrational Energy Redistribution	279
iii.)	Tuning Near Resonant Interactions Through Substitution	295

**PART D : AN INVESTIGATION OF THE EFFECTS OF METHYL INTERNAL  
ROTATION ON THE VIBRATIONAL OVERTONE SPECTRA  
OF METHYL CONTAINING MOLECULES**

- Introduction	313
<b>CHAPTER 11 : The Rigid Methyl Rotor Local Mode Interpretation</b>	<b>318</b>
i.) LM Analysis of Some Methyl Substituted Aromatic Heterocycles	318
ii.) Ground State Mixing: An Additional Source of Intensity	373
<b>CHAPTER 12 : Breakdown of the Rigid Methyl Rotor Interpretation</b>	<b>388</b>
i.) Previous Work on Low Barrier Methyl Rotor Systems	388
ii.) Barrier Height Dependence of Methyl Overtone Features	394
iii.) 2-Butyne, the Homogeneous Rotor Limit	429
iv.) Line Narrowing in the Methyl Overtone Spectrum	436
v.) The $\Delta\nu_{\text{CH}} = 2$ Results and Conclusion.	447
- Summary and Future Challenges	463

## List of Tables

<u>TABLES</u>		<u>PAGE</u>
6.1	Pin-outs of Aerotech stepper motor remote connector	136
9.1	Observed liquid phase overtone peak positions and local mode parameters of thiophene.	213
9.2	Observed liquid phase overtone peak positions and local mode parameters of furan.	228
9.3	<i>Ab initio</i> CH stretching force constants of furan and thiophene	232
9.4	<i>Ab initio</i> CH stretching frequencies of furan, pyrrole and thiophene	235
9.5	Observed liquid phase overtone peak positions and local mode parameters of disubstituted thiophenes.	253
9.6	Observed liquid phase overtone peak positions and local mode parameters of substituted furans.	254
9.7	<i>Ab initio</i> CH stretching frequencies of substituted furans and thiophenes	255

9.8	<i>Ab initio</i> aryl CH bondlengths of substituted thiophenes	265
9.9	<i>Ab initio</i> aryl CH bondlengths of selected furans	266
10.1	Mid-frequency A <sub>1</sub> and B <sub>1</sub> modes of furan and thiophene	292
11.1	Torsional barrier heights of methyl substituted furans and thiophenes	320
11.2	<i>Ab initio</i> CH bondlengths of methyl substituted furans and thiophenes	325
11.3	<i>Ab initio</i> CH stretching frequencies of methyl substituted furans and thiophenes	327
11.4	Liquid phase local mode parameters of methyl substituted furans and thiophenes	328
11.5	Kinetic and potential energy interoscillator methyl coupling constants	340
11.6	Observed and predicted overtone and combination positions in the $\Delta\nu_{\text{CH}}=3$ region of 2,5 dimethyl- thiophene	354
11.7	Predicted overtone and combination intensities in the $\Delta\nu_{\text{CH}}=3$ region of 2,5 dimethylthiophene	355

11.8	Observed and predicted overtone and combination positions in the $\Delta\nu_{\text{CH}}=3$ region of 2,5 dimethylfuran	356
11.9	Predicted overtone and combination intensities in the $\Delta\nu_{\text{CH}}=3$ region of 2,5 dimethylfuran	357
11.10	Observed and predicted overtone and combination positions in the $\Delta\nu_{\text{CH}}=1$ and 2 regions of 2,5 dimethylthiophene	366
11.11	Predicted overtone and combination intensities in the $\Delta\nu_{\text{CH}}=2$ region of 2,5 dimethylthiophene	367
11.12	Observed and predicted overtone and combination positions in the $\Delta\nu_{\text{CH}}=1$ and 2 regions of 2,5 dimethylfuran	368
11.13	Predicted overtone and combination intensities in the $\Delta\nu_{\text{CH}}=2$ region of 2,5 dimethylfuran	369
11.14	Ground state mixing contribution to the intensities of the symmetric $\Delta\nu_{\text{CH}}=2$ transitions of 2,5 dimethylthiophene	384

11.15	Ground state mixing contribution to the intensities of the symmetric $\Delta\nu_{\text{CH}}=2$ transitions of 2,5 dimethylfuran	385
12.1	<u>Ab initio</u> Aryl CH bondlengths of selected toluenes	406

11.15	Ground state mixing contribution to the intensities of the symmetric $\Delta\nu_{\text{CH}}=2$ transitions of 2,5 dimethylfuran	385
12.1	<i>Ab initio</i> Aryl CH bondlengths of selected toluenes	406

## List of Figures

<b><u>FIGURE</u></b>	<b><u>PAGE</u></b>
5.1 Steps involved in the generation and detection of the photoacoustic effect	69
5.2 Transmission of the Birefringent Tuning Element	85
5.3 Single-piece photoacoustic cell	93
5.4 Multi-piece photoacoustic cell	98
5.5 Gas phase photoacoustic and absorption spectrum of neopentane in the $\Delta\nu_{CH}=5$ region	113
5.6 Gas phase $\Delta\nu_{CH}=4$ absorption and $\Delta\nu_{CH}=6$ photoacoustic spectrum of o-xylene	116
5.7 Block diagram of the photoacoustic spectrometer	119
5.8 Schematic of the photoacoustic experiment	121
6.1 IEEE-488 Three wire handshake protocol	127
6.2 Stepper motor IEEE-488 interface circuitry	141
6.3 Upper wiring diagram stepper motor interface	146
6.4 Lower wiring diagram stepper motor interface	148

( List of figures cont.)

9.1	Labelling scheme used for the aryl CH oscillators of the aromatic heterocycles	201
9.2	Liquid phase $\Delta\nu_{\text{CH}}=4$ overtone spectrum of thiophene	203
9.3	Gas phase $\Delta\nu_{\text{CH}}=6$ overtone photoacoustic spectrum of thiophene	205
9.4	Liquid phase $\Delta\nu_{\text{CH}}=4$ overtone spectrum of 2,5 dichlorothiophene	207
9.5	Liquid phase $\Delta\nu_{\text{CH}}=4$ overtone spectra of 2,5 dibromo and 3,4 dibromothiophene	209
9.6	Birge-Sponer plot of the liquid phase aryl overtone progressions of thiophene	212
9.7	Liquid phase $\Delta\nu_{\text{CH}}=3$ overtone spectrum of furan	216
9.8	Gas phase $\Delta\nu_{\text{CH}}=4$ overtone spectrum of furan	218
9.9	Liquid phase $\Delta\nu_{\text{CH}}=5$ overtone spectrum of furan	220
9.10	Gas phase $\Delta\nu_{\text{CH}}=5$ photoacoustic overtone spectrum of furan	222
9.11	Gas phase $\Delta\nu_{\text{CH}}=6$ photoacoustic overtone spectrum of furan	224

(List of figures cont.)

9.12 Gas phase $\Delta\nu_{\text{CH}}=5$ photoacoustic overtone spectra of 2 methyl and 2,5 dimethylfuran	226
9.13 Birge-Sponer plot of the liquid phase aryl overtone progressions of furan	230
9.14 Gas phase $\Delta\nu_{\text{CH}}=3$ overtone spectrum of pyrrole	239
9.15 Liquid phase $\Delta\nu_{\text{CH}}=4$ overtone spectra of 3 methyl, 2 methyl and 2,5 dimethylthiophene	245
9.16 Liquid phase $\Delta\nu_{\text{CH}}=4$ overtone spectra of 2,5 dichloro and 2,5 dimethylthiophene	247
10.1 Liquid phase $\Delta\nu_{\text{CH}}=3$ overtone spectrum of thiophene	274
10.2 Gas phase $\Delta\nu_{\text{CH}}=3$ overtone spectrum of thiophene	276
10.3 Gas phase $\Delta\nu_{\text{CH}}=5$ photoacoustic overtone spectrum of thiophene	278
10.4 Liquid phase $\Delta\nu_{\text{CH}}=3$ overtone spectra of 2,5 dibromo and 3,4 dibromothiophene	299
10.5 Liquid phase $\Delta\nu_{\text{CH}}=3$ overtone spectra of 2,5 dichloro and 2,5 dimethylthiophene	301

(List of figures cont.)

10.6	Gas phase $\Delta\nu_{\text{CH}}=3$ overtone spectrum of 2 methyl- thiophene	305
10.7	Liquid phase $\Delta\nu_{\text{CH}}=4$ overtone spectrum of 2 methyl- furan	308
10.8	Liquid phase $\Delta\nu_{\text{CH}}=5$ overtone spectra of 2 methyl and and 2,5 dimethylfuran	310
11.1	<i>Ab initio</i> methyl torsional barrier in 2 methylfuran	322
11.2	Minimum energy rotamers of 2 and 3 methyl furans and thiophenes.	324
11.3	Gas phase $\Delta\nu_{\text{CH}}=2$ overtone spectrum of 2,5 dimethyl- thiophene	331
11.4	Gas phase $\Delta\nu_{\text{CH}}=2$ overtone spectrum of 2,5 dimethyl- furan	333
11.5	Energy level diagram of the effects of interoscillator coupling on the fundamental methyl CH stretching states	342
11.6	Gas phase $\Delta\nu_{\text{CH}}=3$ overtone spectrum of 2,5 dimethyl- furan	350

(List of figures cont.)

11.7	Gas phase $\Delta\nu_{\text{CH}}=3$ overtone spectra of 2 methyl and 2,5 dimethylfuran	352
11.8	Gas phase $\Delta\nu_{\text{CH}}=2$ overtone spectra of 2 methylfuran and 2,5 dimethylthiophene	361
11.9	Gas phase $\Delta\nu_{\text{CH}}=2$ overtone spectra of 3 methyl, 2 methyl and 2,5 dimethylthiophene	363
12.1	Gas phase $\Delta\nu_{\text{CH}}=3$ overtone spectra of ortho, meta, and para fluorotoluene	396
12.2	Gas phase $\Delta\nu_{\text{CH}}=3$ overtone spectra of ortho, meta, and para chlorotoluene	398
12.3	Gas phase $\Delta\nu_{\text{CH}}=4$ overtone spectrum of parafluoro- toluene	401
12.4	Gas phase $\Delta\nu_{\text{CH}}=5$ photoacoustic overtone spectra of ortho, meta, and para fluorotoluene	405
12.5	Minimum energy methyl conformation of ortho substituted toluenes	410
12.6	Gas phase $\Delta\nu_{\text{CH}}=5$ photoacoustic overtone spectrum of toluene	413

( List of figures cont.)

- 12.7 Gas phase photoacoustic spectrum of the  $\Delta\nu_{\text{CH}}=5$  methyl 416  
overtone region of 2 methylfuran
- 12.8 Gas phase  $\Delta\nu_{\text{CH}}=5$  photoacoustic overtone spectrum of 419  
nitromethane
- 12.9 Gas phase  $\Delta\nu_{\text{CH}}=3$  overtone spectrum of N-methylpyrrole 422
- 12.10 Variable temperature liquid phase  $\Delta\nu_{\text{CH}}=5$  overtone 425  
spectrum of toluene
- 12.11 Variable temperature liquid phase  $\Delta\nu_{\text{CH}}= 3$  and 4 427  
overtone spectrum of orthobromotoluene
- 12.12 Gas phase  $\Delta\nu_{\text{CH}}= 3$  and 4 overtone spectra of 2-butyne 432
- 12.13 Gas phase  $\Delta\nu_{\text{CH}}= 5$  photoacoustic spectrum of 2-butyne 434
- 12.14 Gas phase  $\Delta\nu_{\text{CH}}= 3$  overtone spectra of 2,3,5,6 tetra- 438  
fluoro and 2,3,4,5,6 pentafluoro toluene
- 12.15 Gas phase  $\Delta\nu_{\text{CH}}= 3$  overtone spectrum of 440  
2,6 dichlorotoluene
- 12.16 Gas phase  $\Delta\nu_{\text{CH}}= 2$  overtone spectra of toluene, 450  
o-, m-, p-xylene

( List of figures cont.)

12.17 Gas phase $\Delta\nu_{\text{CH}} = 2$ overtone spectra of 2,3,5,6 tetra- fluorotoluene and p-xylene	452
12.18 Gas phase $\Delta\nu_{\text{CH}} = 2$ overtone spectrum of 2-butyne and 2,3,4,5,6 pentafluorotoluene	454
12.19 Gas phase $\Delta\nu_{\text{CH}} = 2$ overtone spectrum of 2-butyne and neopentane- $\text{d}_9$	457
12.20 Energy level diagram of the $\text{C}_{3v}$ and $\text{C}_{2v}$ limits of the $\nu = 2$ methyl CH stretching states	460

**PART A : INTRODUCTION**

## CHAPTER 1 : DESCRIPTIONS OF MOLECULAR VIBRATION

### - Molecular Vibration and Our Picture of the Molecule

Vibrational degrees of freedom play an important role in determining spectroscopic, thermodynamic, and chemical properties of molecules. Unimolecular and bimolecular reactions rates can be influenced by vibrational excitation<sup>1</sup>. The nature of radiationless transitions and intramolecular energy redistribution are largely governed by the dynamics of the vibrational state<sup>2</sup>. An accurate and detailed description of molecular vibration is requisite for our understanding of these and other fundamental chemical processes.

The vast majority of the models of molecular vibration essentially stem from the pictorial representation of a molecule. Typically a molecule is represented as a collection of nuclei rigidly interconnected by bonds. The bonds signify areas of "attractive" electron density overlap. In this description the nuclei "see" the average coulombic field of the fast electronic motion. Implicit in this picture, is the definition of an equilibrium or instantaneous

geometry of the molecule. This pictorial representation of a molecule is the starting point for most chemical phenomena including molecular vibration. Formally the picture emerges from an adiabatic separation of electronic and nuclear motion of the molecule. This was first carried out for molecules by Born and Oppenheimer<sup>3</sup>.

The adiabatic, Born-Oppenheimer (BO) separation relies on the large differences in the masses of electrons and nuclei. The large mass difference permits one to consider the electronic degrees of freedom as being fast relative to the nuclear degrees of freedom. In the adiabatic BO approximation, the sole influence of the electronic Schrödinger equation on the nuclear Hamiltonian is the appearance of an additional term, the electronic eigenvalue(s), dependent on the nuclear coordinates. This term can be considered part of the internuclear potential  $V(R)$ . Once the form of the internuclear potential is determined, the molecular vibration problem involves solving the BO nuclear Schrödinger equation.

In principle, the potential energy surface of a molecule,  $V(R)$ , is available from the BO electronic Schrödinger equation. Even at modest levels of theory, electronic structure calculations are

capable of predicting many molecular properties and phenomena with reasonable accuracy. However, to obtain potential energy surfaces of spectroscopic quality requires very high levels of theory. Currently such high levels of calculation are only practical for light diatomic or triatomic systems<sup>4,5</sup>. Such a completely *ab initio* approach is not generally possible. Tractable models typically use potentials of an assumed general form. Most models of molecular vibration can be distinguished in their treatment of the vibrational potential.

i.) The Normal Mode Model<sup>6,7</sup>

Much of the effort involved in developing an accurate model of molecular vibration concerns determining the form of the nuclear potential. The central assumption in most treatments of molecular vibration is that the relative displacements of nuclei are infinitesimal. Thus the introduction of a reference molecular geometry in the ~~B.O.~~ separation offers a convenient starting point for the model. The nuclear potential can be expanded in a multicoordinate Taylor series about the reference geometry

X  
Consistency  
B.O. v  
B.O.

$$V = V_0 + \sum_i^{3N-6} \left( \frac{\partial V}{\partial q_i} \right)_0 q_i + \frac{1}{2} \sum_{i,j}^{3N-6} \left( \frac{\partial^2 V}{\partial q_i \partial q_j} \right)_0 q_i q_j + \frac{1}{6} \sum_{i,j,k}^{3N-6} \left( \frac{\partial^3 V}{\partial q_i \partial q_j \partial q_k} \right)_0 q_i q_j q_k + \dots \quad (1.1)$$

Choosing the equilibrium geometry of the system as the reference causes the first partial derivatives to vanish. Recall that by definition the equilibrium configuration is at the minimum of the potential energy. The  $V_0$  term may be arbitrarily set to zero, thus

establishing the energy origin. The second partial derivatives correspond to the first nonzero terms in the potential expansion. Normal mode treatments retain only these quadratic terms in the potential expansion.

$$V_{\text{NM}} = \sum_{i,j}^{3N-6} f_{ij} q_i q_j \quad (1.2a)$$

where

$$f_{ij} = \left( \frac{\partial^2 V}{\partial q_i \partial q_j} \right)_0 \quad (1.2b)$$

In cartesian coordinates the momentum operator has the familiar, simple form

$$\hat{p}_i = - \frac{i\hbar}{2\pi} \left( \frac{\partial}{\partial q_i} \right) \quad (1.3)$$

In a general coordinate system, the operator takes on a more

complicated form in order to preserve the canonical commutation relation with the position operator<sup>8,9</sup>. Within the infinitesimal amplitude approximation, the kinetic energy operator takes on the form

$$2T = \sum_{i,j}^{3N-6} (g^{ij})_0 p_i p_j \quad (1.4)$$

where  $p_i$  has the usual form (1.3) and the constant terms  $(g^{ij})_0$  are the contravariant elements of the metric tensor describing the transformation from cartesian to the general coordinate system of the static molecule<sup>10</sup>. Typically, the molecule is described in internal coordinates. In this case the  $(g^{ij})_0$  are simply the Wilson G matrix elements<sup>6,11</sup>,  $G_{ij}$ .

The normal mode Hamiltonian expressed in  $3N-6$  internal vibrational coordinates is,

$$H_{NM} = \sum_{i,j}^{3N-6} (G_{ij} p_i p_j + f_{ij} q_i q_j) \quad (1.5)$$

There exists a canonical transformation in which an equation of the type (1.5) becomes exactly separable<sup>12</sup>.

$$H_{\text{NM}} = \frac{1}{2} \left[ \sum_i^{3N-6} \dot{Q}_i^2 + \sum_i^{3N-6} \lambda_i Q_i^2 \right] \quad (1.6)$$

These new  $3N-6$  coordinates ( $Q_i$ ) are known as the normal vibrational coordinates of the molecule. In these normal coordinates, the infinitesimal amplitude kinetic energy operator and the quadratic potential energy operator are diagonal. Equation (1.6) is simply the Hamiltonian equation for  $3N-6$  independent one-dimensional harmonic oscillators. The Schrodinger equation for a harmonic oscillator (HO) has well known solutions<sup>12</sup>,

$$\epsilon_i = h\nu_i \left( n_i + \frac{1}{2} \right) \quad (1.7a)$$

where  $\nu_i$  is the harmonic frequency,

$$\lambda_i = 4 \pi^2 \nu_i^2 \quad (1.7b)$$

and  $n_i$  is the vibrational quantum number. The  $n^{\text{th}}$  HO eigenfunction is given by,

$$\psi_{n_i} = N_n H_n \exp\left(-\frac{1}{2} Q_i^2\right) \quad (1.7c)$$

where  $H_n$  are Hermite polynomials<sup>13</sup> of degree  $n$  in variable  $Q_i$  and  $N_n$  is the HO normalization constant<sup>12</sup>. A basis for the vibrational state space of the normal mode Hamiltonian is provided by the  $3N-6$  fold tensor product of the complete space of the one - dimensional eigenfunctions. A single state vector is simply written as  $\psi_{\text{NM}} = |a_1 b_2 c_3 \dots v_{3N-6}\rangle$  where the  $3N-6$  vibrational modes have  $a, b, c, \dots$  and  $v$  quanta of excitation respectively. These are the stationary states of

the  $3N-6$  dimensional normal mode Hamiltonian.

The treatment of molecular vibration has so far considered an isolated molecule in field-free space. The molecular states however are typically probed through their interaction with a radiation field. The radiation field is typically treated classically while the molecule is handled in a quantum mechanical description. This treatment of molecule-field interactions is known as the semi-classical treatment. In its most usual form the interaction is described perturbatively within the the electric dipole approximation<sup>14,15</sup>. For an electric dipole vibrational transition to occur, the matrix element  $\langle \phi^{NM} | \mu | \phi^{NM} \rangle$  must be nonzero, where  $\mu$  is the electric dipole moment operator for the particle system. Again within the infinitesimal amplitude approximation,  $\mu$  can be expanded about the reference geometry.

$$\mu = \mu_0 + \sum_i^{3N-6} \left( \frac{\partial \mu}{\partial Q_i} \right)_0 Q_i + \frac{1}{2} \sum_{i,j}^{3N-6} \left( \frac{\partial^2 \mu}{\partial Q_i \partial Q_j} \right)_0 Q_i Q_j + \dots \quad (1.8)$$

The term  $\mu_0$  is the static dipole moment of the molecule in its

equilibrium configuration. This static term makes no contribution to the transition intensity. In practice it is customary to consider only the linear dipole terms ( $Q_i$ ). Retention of only the linear terms leads to strict vibrational electric dipole selection rules. Dipole allowed transitions are restricted between states which differ by one in the total vibrational quantum number and where only one vibrational mode is excited. For example, ( $|0_1 0_2 \dots 1_i \dots 3_k \dots 0_{3N-6}\rangle \rightarrow |0_1 0_2 \dots 2_i \dots 3_k \dots 0_{3N-6}\rangle$ ) is dipole allowed but ( $|0_1 0_2 \dots 1_i \dots 3_k \dots 0_{3N-6}\rangle \rightarrow |0_1 0_2 \dots 0_i \dots 2_j \dots 3_k \dots 0_{3N-6}\rangle$ ) is not despite the fact that the latter transition satisfies the  $\Delta v = \pm 1$  selection rule. The vibrational energy level spacing is such that molecules are predominantly in their ground vibrational state under usual equilibrium situations. The dominant transitions are thus predicted to be to states with one vibrational quantum of excitation ( $|0_1 0_2 \dots 0_{3N-6}\rangle \rightarrow |0_1 0_2 \dots 1_i \dots 0_{3N-6}\rangle$ ). These are the fundamental vibrational transitions of the molecule.

Since the energies of all the normal mode vibrational states of a molecule are implicitly known once the fundamental states have been determined, most NM treatments explicitly only consider the solution of the NM Hamiltonian in the  $v = 1$  manifold of vibrational excitation. Although the fundamental transitions can be reasonably

understood within the NM treatment, the motivation for a quadratic vibrational potential (equation 1.2) was really because it led to the simple equation of motion of  $3N-6$  independent harmonic oscillators. From the outset, the unrealistic nature of the potential was recognized. The harmonic oscillator has an infinite number of bound states and therefore cannot predict the chemically very important phenomenon of vibrational dissociation. Spectroscopic investigations of the vibrational energy levels of molecules also clearly point out the inadequacies of the model. The energy levels of a particular vibrational mode are rarely evenly spaced (harmonic) and transitions which are forbidden by the harmonic oscillator dipole selection rules are often observed. To account for these anharmonicities, higher order terms in the potential energy expansion (1.1) are required. These "anharmonic" terms in the potential are often referred to as the mechanical anharmonicity of the modes. Not to be confused, the higher order terms in the dipole expansion (1.8) are sometimes referred to as electrical anharmonicity. Mechanical anharmonicity leads to the prediction of a finite number of bound levels for an oscillator and hence vibrational dissociation. Retention of only the linear dipole terms

but inclusion of mechanical anharmonicity relaxes the vibrational selection rules. Weak vibrational overtone transitions ( $|0_1 0_2 \dots 0_{3N-6}\rangle \rightarrow |0_1 0_2 \dots n_i \dots 0_{3N-6}\rangle$  for  $n_i > 1$ ) in addition to the fundamental transitions are predicted. Mechanical anharmonicity breaks the  $\Delta v = \pm 1$  selection rule but the linear dipole approximation enforces that only one mode is excited.

It would appear that by including higher order expansion terms in the potential many of the problems encountered in the NM description are resolved. The inclusion of these terms however leads to a complicated equation of motion which in general cannot be transformed into simple forms like the NM equations (1.6). Typically this problem is approached by assuming that the higher order, anharmonic terms are small relative to the quadratic (harmonic) terms. The NM Hamiltonian can therefore be used as a zero order description of the motion, while the anharmonic terms are treated as perturbations on this zero order Hamiltonian. Since the NM Hamiltonian is expressed in normal coordinates, the anharmonic expansion must be expressed in these normal coordinates. The perturbative corrections due to the higher order terms are determined within the harmonic oscillator product function basis.

The perturbative approach essentially assumes that the anharmonicity corrections are small or at least much smaller than the effects of the quadratic terms. There are many cases however where the vibrational motion is highly anharmonic. Torsions, inversions, and XH stretching vibrations ( $X=C,O,N,S,\dots$ ) are specific examples of modes which are usually highly anharmonic. In these cases the NM picture provides a poor zero order description of these modes. In other words partitioning of the Hamiltonian as described above often yields large terms in the perturbing Hamiltonian. In addition, the potential when expressed in normal coordinates is often highly nonseparable<sup>16</sup>. Thus although the quadratic terms are separable in normal coordinates, the perturbative approach must not only consider the diagonal higher order terms but also a large number of the other off-diagonal terms at the various orders of the expansion.

In this thesis, we are primarily concerned with the description of the highly anharmonic XH stretching motion of the molecule. As already discussed, such modes are poorly described in the NM model. We are particularly interested in the high energy features of the vibrational spectra of polyatomic molecules. The NM description

fails totally in these higher energy regions. The perturbative NM approach provides a complicated and unilluminating description of these features. A simpler description is preferable. Experimental observations in the high energy vibrational regions of polyatomic molecules provide the guide for the development of a simple, yet accurate treatment of such modes. One such model is the local mode (LM) model.

## ii.) The Zero Order Local Mode Description

The extension of the normal mode approach to include anharmonicity often leads to complications. The root of the complications lies in the magnitudes of the anharmonicity corrections relative to the quadratic terms. This problem is particularly acute for hydrogen containing molecules which are noted to have highly anharmonic XH stretching modes. The problem is further compounded by the nonseparability of the anharmonicity corrections when expressed in normal coordinates. In order for the normal coordinate approach to adequately represent the higher vibrationally excited states of hydrogen containing molecules, a large number of terms in the potential expansion must be retained. Simplifications to the Hamiltonian description of the high energy vibrational features are desirable. The local mode (LM) model is one such approach at finding a simplified description of the highly anharmonic XH stretching motion of hydrogen containing molecules.

The LM description integrates many of the observations from vibrational overtone spectroscopy into its model. Vibrational

spectroscopy in the near infrared and visible regions had its origins circa 1930<sup>17,18</sup>. These early investigations made several important observations. It was generally found that these spectral regions were very sparsely populated with vibrational features. The one major exception was in the spectra of hydrogen containing molecules. These spectra displayed progressions of absorption bands which could be associated with the vibrational motion of the light hydrogen atom. The dominant peaks in the spectra were typically assigned as overtones of the XH stretching mode. The frequencies and intensities of these features clearly demonstrated the breakdown of the harmonic approximation. The XH stretching progressions of a polyatomic molecule were very similar to the progression of the stretching mode of a diatomic molecule. The overtone progressions could successfully be fit to the empirical potential functions developed for diatomics. The two parameter anharmonic oscillator equation often provides a good fit to the observed overtone progressions.

$$\epsilon_i = \omega_i n_i - \chi_i (n_i^2 + n_i) \quad (1.9)$$

The terms  $\omega_i$  and  $\chi_i$  are known as the frequency and anharmonicity of the progression.

Interest in overtone spectroscopy waned throughout the 40's and 50's. The observations remained essentially unexploited over this period. In 1968 interest in XH stretching overtones was renewed due to their role as acceptor modes in radiationless transitions<sup>19,20</sup>. This work led to the development of the LM description in the early 1970's<sup>21,22,23</sup>. Since the XH stretching vibrations dominate the high energy regions, the LM approach is typically only concerned with these modes. Due to the light mass of the hydrogen compared to the central X atom, the XH stretching frequency ( $\approx 3000 \text{ cm}^{-1}$ ) is much higher than the remaining vibrational modes of motion of the molecule ( $\leq 2000 \text{ cm}^{-1}$ ). It is this frequency mismatch which causes the XH stretching motion to be relatively independent of the other vibrational motion. Quantum mechanically this independence arises from the small off resonant character of the interaction between modes of disparate frequencies. The vibrational Hamiltonian can effectively be partitioned into terms involving the XH-stretching motion and terms involving the

other vibrations. The LM approach takes advantage of this partitioning and ignores the small interaction terms.

$$H_{\text{vib}} = H_{\text{XH-stretch}} + H_{\text{other}} + H_{\text{interaction}} \quad (1.10)$$

In normal coordinates the anharmonic terms of the XH-stretching potential are usually highly nonseparable. In valence coordinates however, the potential is nearly separable. Expressing the XH-stretching Hamiltonian in internal coordinates leads to an approximate partitioning of the terms. The leading terms involve only single oscillators, while the smaller interoscillator coupling terms are ignored at zero order in the LM model description.

$$H_{\text{LM}} = \sum_i^{\text{XH}} h_i + \sum_{i,j}^{\text{XH}} h'_{ij} + \dots \quad (1.11)$$

At zero order the LM model considers each XH stretching vibration to be completely separable from the remaining internal and

external degrees of freedom of the molecule. This is consistent with the "diatomic like" progressions observed in the vibrational spectra. Each XH group is modelled as an independent diatomic anharmonic oscillator,

$$h_i = \frac{1}{2} G_{ii} p_i^2 + V_i(q_i) \quad (1.12a)$$

where typically the XH-stretching potential is approximated by an empirical Morse function<sup>24</sup>.

$$V_i(q_i) = D_i \left[ 1 - \exp(-a_i q_i) \right]^2 \quad (1.12b)$$

The symbols  $D_i$  and  $a_i$  are the Morse dissociation energy and the inverse length parameter respectively,  $G_{ii}$  is the diagonal G matrix element of the XH oscillator, while  $p_i$  and  $q_i$  are the momentum and position operators of the  $i^{\text{th}}$  oscillator.

The one-dimensional Morse oscillator Schrodinger equation has known analytical solutions<sup>24,25</sup>.

$$\epsilon_i^n (\text{cm}^{-1}) = \left[ \frac{a_i (2 G_{ii} D_i)^{\frac{1}{2}}}{2\pi c} (n_i + \frac{1}{2}) - \frac{h a_i^2 G_{ii}}{8\pi^2 c} (n_i + \frac{1}{2})^2 \right] \quad (1.13a)$$

The Morse oscillator eigenfunctions are given by:

$$|n_i\rangle = N_{n_i} \exp\left(-\frac{y_i}{2}\right) y_i^{\frac{1}{2}(k_i-2n_i-1)} L_{n_i}^{(k_i-2n_i-1)}(y_i) \quad (1.13b)$$

where

$$k_i = \frac{4\pi}{h a_i} \left( \frac{2 D_i}{G_{ii}} \right)^{\frac{1}{2}} \quad (1.13c)$$

$$y_i = k_i \exp(-a_i q_i) \quad (1.13d)$$

and

$$L_{n_i}^{(k_i-2n_i-1)}(y_i) = \sum_{m=0}^{n_i} \frac{(-y)^m \Gamma(k_i-n_i)}{m! (n_i-m)! \Gamma(k_i-2n_i+m)} \quad (1.13e)$$

$$N_{n_i} = \left( \frac{n_i! a_i (k_i - 2n_i - 1)}{\Gamma(k_i - n_i)} \right)^{\frac{1}{2}} \quad (1.13f)$$

are the associated Laguerre polynomials<sup>13</sup> and the normalization constants respectively.

The eigenvalues expressed in Morse potential parameters can be equated to the two parameter anharmonic oscillator equation (1.9),

$$\omega_i = \frac{a_i (2 D_i G_{ii})^{\frac{1}{2}}}{2\pi c} \quad (1.14a)$$

$$\chi_i = \frac{h a_i^2 G_{ii}}{8\pi^2 c} \quad (1.14b)$$

which is used to fit the observed XH stretching overtone progressions.

A basis for the N oscillator state space is provided by the product space of Morse oscillator eigenfunctions. A single vector in the state space is represented as  $\phi^{LM} = |a_1 b_2 c_3 \dots n_N\rangle$  where  $a_1, b_2, \dots, n_N$  are Morse oscillator quantum numbers for the particular oscillator. For a system of N distinguishable oscillators, this primitive basis also defines the physical eigenvectors of the system. We will distinguish between two types of zero order local mode eigenstates of the system; pure local mode overtone and combination states. Pure local mode overtone states correspond to states in which the vibrational excitation is localized in a single XH bond. States in which two or more oscillators have nonzero vibrational quantum numbers will be called local mode combination states.

In an oscillator system where there are two or more chemically equivalent oscillators, the primitive Morse oscillator product functions are not in general the physical eigenstates of the system. A physical basis can be constructed by symmetry adapting

the primitive basis functions which span the degenerate subspaces of the complete state space. Consider a system consisting of two equivalent oscillators. The primitive states  $|n_1 m_2\rangle$  and  $|m_1 n_2\rangle$  span a two dimensional degenerate subspace of the complete state space. The state  $|n_1 m_2\rangle$  corresponds to a state with  $n$  quanta in the oscillator labelled number one and  $m$  quanta in oscillator two. Due to the indistinguishability of the oscillators however, this state has no physical meaning. Instead physically we can only discuss preparing states with  $n$  quanta in one bond and  $m$  quanta in the other, without specifying which bond has a particular level of excitation. The physical states spanning the degenerate subspace are the permutationally symmetry adapted states. In this case, the states

$$\phi_{LM} = \frac{1}{\sqrt{2}} [ |n_1 m_2\rangle \pm |m_1 n_2\rangle ] \quad (1.15)$$

are the physical states spanning the degenerate subspace.

The zero order LM model is more successful at describing the dominant XH stretching spectral features than a low order NM based

approach. The zero order NM linear dipole selection rules restrict transitions from the ground state ( $v = 0$ ) to the fundamental ( $v=1$ ) states. In the zero order LM model, transitions from the ground state to the fundamental and local mode overtone states are allowed within the linear dipole approximation. Transitions to the LM combinations however are forbidden. Typically, the LM fundamental and overtone states are the dominant dipole transitions involving the XH stretching states of the molecule. For the usual XH stretching parameters the model predicts a decrease in overtone intensity with increasing excitation<sup>26,27</sup>. This fall-off in intensities is commonly observed in the XH stretching fundamental-overtone progressions.

Along with predicting the general features of the high energy XH stretching features, the LM approach affords a structural and chemical interpretation. The distinct nature of chemically nonequivalent oscillators appears in their frequency and anharmonicity parameters. A characteristic overtone progression is predicted for each of the chemically nonequivalent oscillators of the system. Unique progressions can be identified not only between distinct oscillator types (eg CH from OH) but also between the same oscillator types in differing chemical environments. For example,

overtone features associated with methyl, methylene, methyne, and aromatic CH oscillators occur at characteristic energies within the CH stretching regions. Shifts between features within these characteristic energy ranges reflect subtle differences in local chemical environments. These shifts have been used to infer structural and conformational information about the XH oscillators of a molecule<sup>28</sup>. Such information is particularly important since many other structural techniques have difficulty "locating" the light hydrogen atoms. The structural interpretations which arise from a zero order LM description are used throughout this thesis. The aromatic CH stretching features of the substituted benzenes and aromatic heterocycles can be understood in these simple terms. As discussed at the end of the thesis, structural interpretations are also reasonably successful in describing the CH stretching behaviour of molecules normally considered as nonrigid systems.

### iii.) Harmonic Coupling Schemes in the Local Mode Model

Comparing the NM and LM treatments, it is the form of the internuclear potential that determines which approach is the most suitable starting point for the description of the vibrational motion. Both descriptions essentially assume that the amplitudes of vibration are small. The main difference is in the partitioning of the small amplitude nuclear Hamiltonian. When the off-diagonal quadratic coupling terms dominate the potential expansion, the NM partitioning provides a better zero order description of the motion. When mechanical anharmonicity is important a local mode type approach is probably preferable. The spectral features which are of interest in this thesis are the CH stretching modes of simple organic molecules. These modes are known to be highly anharmonic and hence would seem best suited to a LM type treatment. The zero order LM model can predict the general features of the higher energy vibrational spectra of many molecules. In addition, chemical and structural arguments based on the LM description are consistent and agree with theory. However, the zero order LM model often cannot account for the detailed features observed in the fundamental and

lower CH stretching overtone regions. Inclusion of interoscillator harmonic coupling in the LM model extends the applicability of the model to the lower CH stretching energy regions<sup>29-39</sup>. This section reviews such a harmonic coupling extension of the LM model. The approach and notation most closely follows that used by Mortensen et al<sup>29</sup> and Mortensen<sup>31</sup>.

The zero order LM Hamiltonian considers only the terms involving single oscillators. The next higher term, considers the interactions between two oscillators. The lowest order of the two-body interaction terms are the quadratic kinetic and potential energy couplings.

$$H'_{ij} = \sum_{i < j}^{3N-6} \left( G_{ij} p_i p_j + f_{ij} q_i q_j \right) \quad (1.16)$$

In the multicoordinate Taylor expansion of the potential, the cubic ( $f_{ijj}$ ), quartic ( $f_{ijjj}$ ) and higher order two-body force constants are assumed to decrease monotonically. Models retaining only the dominant quadratic two-body terms will be termed harmonic

coupling models.

Since we are generally concerned with the XH stretching degrees of freedom, we focus on interaction terms involving these modes. We distinguish between two types of quadratic couplings. Terms describing the interaction of two XH stretching modes will be known as the interoscillator couplings. The other type of term involves the quadratic interaction between a XH stretch and another, lower frequency mode. Harmonic raising and lowering operators,  $a_j^+$  and  $a_j$  respectively, will be used to examine the interactions.

$$a_j = \frac{1}{\sqrt{2}}(Q_j + iP_j) \quad (1.17a)$$

$$a_j^+ = \frac{1}{\sqrt{2}}(Q_j - iP_j) \quad (1.17b)$$

The variables  $Q_j$  and  $P_j$  are the dimensionless coordinate and position operator for the  $j^{\text{th}}$  degree of freedom<sup>12</sup>. The usefulness of a set of raising and lowering operators for coupled oscillators depends on their ability to accurately represent the coupling operator and their

suitability to the zero order uncoupled problem. Quadratic interactions can be expressed in terms of the harmonic oscillator raising-lowering operators,

$$H'_{ij} = \sum_{i < j} \left( -\gamma_{ij} P_i P_j + \phi_{ij} Q_i Q_j \right) \quad (1.18a)$$

$$H'_{ij} = \sum_{i < j} \left[ -\gamma_{ij} \left( a_i^+ a_j^+ - a_i^+ a_j - a_i a_j^+ + a_i a_j \right) + \phi_{ij} \left( a_i^+ a_j^+ + a_i^+ a_j + a_i a_j^+ + a_i a_j \right) \right] \quad (1.18b)$$

where

$$\gamma_{ij} = \frac{G_{ij}}{2\pi c} \left( \frac{f_{ii} f_{jj}}{G_{ii} G_{jj}} \right)^{\frac{1}{4}} \quad (1.19a)$$

$$\phi_{ij} = \frac{f_{ij}}{2\pi c} \left( \frac{G_{ii} G_{jj}}{f_{ii} f_{jj}} \right)^{\frac{1}{4}} \quad (1.19b)$$

are the kinetic and potential energy coupling parameters in units of wavenumbers.

A system of harmonic oscillators with harmonic coupling, is exactly represented by equation (1.18b). The situation is more complex for a system of Morse oscillators. The operators  $a_{j+}$ ,  $a_j$  are not the exact raising and lower operators for the Morse oscillator. The matrix elements of the harmonic raising-lowering operators between bound Morse states differ from those between harmonic states. For the lower Morse states however, the raising and lowering properties are approximately satisfied by  $a_{j+}$  and  $a_j$ . Also, for typical Morse parameters, the matrix elements do not differ drastically from the harmonic oscillator values<sup>29</sup>. Since we will be predominantly concerned with the harmonic coupling of Morse oscillators at the lower levels of excitation, we will use the  $a_{j+}$  and  $a_j$  operators as the exact Morse raising and lower operators yielding the harmonic oscillator matrix elements. The validity of this assumption is discussed later in the thesis.

Three factors determine the importance of the

interaction on the XH stretching spectral features. The strength of the interaction depends on the magnitude of the coupling ( $G_{ij}$  and  $f_{ij}$  in the case of harmonic coupling), the zero order energy mismatch between the coupled levels, and the coupling matrix element. When expressed in terms of raising and lowering operators, the quadratic couplings partition into two classes of terms. Terms like  $a_i^+ a_j$ , preserve the total vibrational quantum number while the second class of terms,  $a_i^+ a_j^+$  or  $a_i a_j$ , couple states which differ by two in total vibrational quanta. We shall often refer to the two classes of terms as intramanifold and intermanifold coupling terms respectively. The effects of these two classes of coupling terms will be considered separately for the description of both the interoscillator coupling and the coupling of an XH stretch and another internal mode of the molecule.

Partitioning the couplings into two classes leads to simplifications in model descriptions of the quadratic interactions involving anharmonic XH stretching modes. Initially, consider only the interoscillator XH harmonic coupling. Except in the very high energy realm, the vibrational XH stretching manifolds are distinct. The disparate energies between the  $v-2$ ,  $v$ , and  $v+2$  manifolds, where

$v$  is the total quanta of XH stretch vibration, suggest that the second class of couplings which couple XH stretching states between these manifolds will be of minor importance. The first class of terms which couple XH stretching states within a vibrational manifold are more favourable on energetic grounds. Since the magnitude of the coupling and the coupling matrix element are expected to be similar between intra and intermanifold XH stretching states, the first class of coupling terms are expected to be the dominant quadratic interoscillator interactions.

The second class of terms describing the coupling of a zero order local mode XH stretching state and a zero order state involving other modes suffers from the same energy mismatch problem. Although the  $v \pm 2$  energy mismatch will be less severe than between the zero order XH stretching states, for typical XH stretching anharmonicity parameters the energy mismatch is still considerable over a wide range of energies. Therefore on energetic grounds, the intermanifold coupling terms whether describing interoscillator or the other quadratic couplings involving XH oscillators are not likely to be important. The intramanifold coupling terms involving XH stretching and other lower frequency

modes can become energetically favourable at much lower energies than the intermanifold couplings. In the highly anharmonic regime where the XH-stretching  $v \pm 1$  manifold separation approaches the frequency of another interacting mode, the first class of coupling may become important. For typical mode frequencies and XH oscillator anharmonicities this will only occur at very high levels of XH stretch excitation. The sensitivity of current experimental methods limits the energy range over which vibrational overtone spectra can be observed. Typically spectral features at very high levels of XH stretch excitation can not currently be observed. On the basis of the energy mismatch, the quadratic interactions between XH stretching and lower frequency modes as well as the intermanifold interoscillator couplings are expected to be of minor importance in the accessible overtone regions.

Harmonic coupling extensions of the zero order LM model which retain only the intramanifold component of the interoscillator coupling have been used by several people<sup>29-39</sup>. Such a model is attractive for several reasons. Harmonic oscillator algebra leads to simple expressions for the off-diagonal coupling matrix elements. Like the zero order LM model, the XH stretching motion is treated

independently from the remaining degrees of freedom of the molecule. By considering only the intramanifold component of the interoscillator coupling, the dimensionality of the problem is drastically reduced. Each manifold of XH stretching states with the same total quanta of vibrational excitation can be considered independently. This leads to a model of very modest complexity which is capable of describing XH stretching spectral properties over a relative wide energy range.

Further simplifications to coupling models have been applied. One such simplification is the exclusion of long range interoscillator coupling terms from the coupling operator. In the infinitesimal amplitude approximation, the quadratic kinetic energy coupling constant,  $G_{ij}$ , vanishes between XH oscillators which do not share the same central X atom. The long range potential force constants between such oscillators are generally thought to be small. Retaining only the one-bond XH stretch - stretch interaction terms leads to a simplified coupling operator. The vibrational overtone spectra of many molecules can be successfully analysed using this simpler form of the coupling operator. The intramanifold and one-bond intramanifold coupling approximations are used in

many parts of this thesis. For many cases, the spectra clearly show the quality of the approximations.

## CHAPTER 2 : INTRODUCTION TO THE PROBLEM

The understanding of vibrational overtone spectroscopy and dynamics involves many concepts from physics and chemistry, as well as technology. This diversity is reflected in this thesis. The work presented here deals with instrumental techniques, correlates spectroscopic data with chemical structure and theoretical models with the aim of contributing, in some modest way, to a deeper understanding of the highly vibrationally excited states of molecules. Owing to the diversity of the work contained in this thesis, providing a single comprehensive introduction at this point is rather difficult. Instead, the central problems addressed in this work will be briefly introduced. More detailed introductions to the specific subject areas will be given in the appropriate Chapters of this thesis.

Three central problems can be identified as the driving force behind the thesis work. The first motivation was to extend our laboratory's experimental capability. The enhanced sensitivity of laser photoacoustic techniques over conventional absorption

spectroscopic methods enable the weaker, higher energy vibrational overtone spectra of low vapour pressure samples to be recorded. Part B which is composed of Chapters 3 through 9 explains the methods employed in the experimental investigations. The main topic of this part of the thesis is the construction of a laser photoacoustic spectrometer and its application to vibrational overtone spectroscopy. Since this represents the first application of laser photoacoustic spectroscopy in our laboratory, the sections are quite detailed. It is hoped that the information provided in these sections will allow future investigators to use and extend the performance and applications of the spectrometer.

Included in Part B are Chapters briefly describing other methodology employed in the spectroscopic and theoretical studies. The other sections of the thesis concern specific results of such studies.

A second central motivation behind this thesis is the comparison of the behaviour of the aryl CH stretching overtones of 5-membered aromatic heterocycles to the substituted benzenes. It was anticipated that the spectral behaviour would be very similar. In particular, it was hoped that bondlength - frequency correlations

developed for substituted benzenes could be applied to the aromatic heterocycles. There are a number of similarities between the two types of molecules. The effects of substituents on the aryl overtones of 5-member aromatic heterocycles follow the same patterns as the substituted benzenes. The substituent effects have simple structural - electronic interpretations which follow from the zero order LM description.

Despite the overall similarity between the aromatic heterocycles and benzene molecules, there are subtle but important differences. Perhaps the most important difference is the breakdown of the bondlength - frequency correlation equations for the aromatic heterocycles. The investigation of the aryl CH stretching regions and the breakdown of the bondlength - frequency correlations for the 5-member aromatic heterocycles, lead to a number of intriguing questions. Experimental and theoretical evidence suggests that an important source of the bondlength-frequency correlation breakdown lies in the different relative ratios of aryl CH stretching frequencies to anharmonicities between substituted benzenes and 5-member aromatic heterocycles. However, Fermi resonant interactions are clearly visible in the aryl CH

stretching overtone progressions of the aromatic heterocycles.

These near resonant interactions also contribute to the breakdown of the established correlation equations for the aromatic heterocycles.

In addition, the role of Fermi resonant interactions in determining the structure of aryl overtone regions and in particular aryl overtone linewidths has been an on-going question in vibrational overtone spectroscopy. Again the comparison between 5-member aromatic heterocycles and benzene systems offers further insight into their role at various regimes of vibrational state densities.

The main thrust of Part D, Chapters 11 and 12, has been to attempt to understand the methyl CH stretching fundamental and overtone spectral features. Both normal mode and local mode treatments of the vibrational motion of a methyl group considers the group as being rigid. Methyl groups display a widely varying nature depending upon the frame to which they are attached. Spectroscopic as well as theoretical findings reveal that there are a large class of methyl top-frame systems which have exceptionally low ground and excited state barriers to internal rotation. The vibrational spectra of this class of methyl top - frame molecule are generally not well described by conventional NM and LM approaches. The spectra of a

wide variety of methyl rotor systems are reported and compared to earlier work and interpretations. Chapter 11 applies various rigid harmonic coupled LM schemes to the high barrier methylthiophenes. A structural interpretation arising from the conformational nonequivalence of the methyl CH oscillators emerges for the overtone regions. The success of this structural interpretation is more fully explored. Also the importance of intermanifold coupling terms to account for the intensities of the  $\Delta\nu_{\text{CH}} = 2$  methyl combination transitions is clearly demonstrated.

Chapter 12 attempts to explain the features in the methyl overtone spectra that could not be accounted for by the rigid or structural interpretation of the features. Methyl substituted benzenes are the most studied molecules and provide the most information. In the high overtone regions ( $\Delta\nu_{\text{CH}} \geq 3$ ), the molecules seem to span the range between nonrigid and rigid methyl rotor systems depending on the substitution pattern. At  $\Delta\nu_{\text{CH}} = 2$  the spectra of low and high barrier systems seem to converge. At this overtone the rigid  $C_{2v}$  analysis which acknowledges the conformational nonequivalence of the methyl oscillators seems to provide a better description than the equivalent oscillator  $C_{3v}$

analysis. Neither analysis is completely satisfying. This is interpreted as a breakdown of the rigid methyl group approximation.

**PART B : EXPERIMENTAL**

## Chapter 3 : Samples and Sample Handling

### i) Materials

The compounds used in these studies were available commercially from Aldrich Chemical Company. The stated compound purities ranged from 97+ to 99+%. All compounds were used without further purification.

### ii) Sample Preparation

#### - Liquid Phase Spectra

The liquid phase overtone absorption spectra of a number of room temperature liquids and low melting solids are presented in this work. Samples were placed in cells of pathlengths ranging from 0.10 to 10.0 cm. The longer pathlengths were used for the higher, less intense overtone regions.

Some of the liquid phase experiments were carried out at both low and high temperatures. The low temperature absorption spectra were obtained using a glass Dewar cell filled with the appropriate low temperature bath mixture. Variable high temperature spectra

were obtained in two ways. In first method the optical cell was wrapped with heating tape and the temperature was raised and controlled with a Variac power supply. The second method employed a cell wrapped with copper tubing. A variable temperature, water circulating bath (Haake, Berlin) was used to control the temperature. The former method allowed one to run spectra at temperatures exceeding 90°C, however electrical interference from the Variac tended to deteriorate the signal-to-noise of the high temperature experiment. In both methods, the temperature was monitored by mounting a thermometer inside the liquid cell.

Low melting solids were added to heated cells and the absorption spectra of the melted samples were obtained.

#### - Gas Phase Spectra

Gas phase photoacoustic and absorption spectra represent the bulk of the experimental work. Overtone transitions are weak. The low sensitivity of absorption spectroscopy coupled with the low chromophore densities encountered in the gas phase make it necessary to use long sample pathlengths. Low energy overtone,

$\Delta\nu_{\text{CH}}=2-4$ , absorption spectra were obtained with Wilks Model 5720 gas cell (Wilks Scientific Corp., South Norwalk, CT). The pathlength of the gas cell can be varied in 1.5 m increments from 0.75 m to 21.75 m. NaCl or KBr cell windows were used for all the absorption spectra. The Wilks cell was equipped with a heating jacket for high temperature operation. Elevated temperature operation permitted higher sample vapour pressures to be used in the cell when studying low boiling liquids. The higher intrinsic sensitivity of photoacoustic spectroscopy permits the weak high overtone spectra to be taken with gas cells of approximately 10 cm pathlength. A detailed description of the photoacoustic cells will be given in Chapter 6. All photoacoustic spectra were taken at room temperature.

The Wilks gas cell was placed in the absorption spectrometer, connected to a vacuum rack, and pumped down for a minimum of 1 hour. Once pumped down, the desired pathlength was set and the cell was aligned within the spectrophotometer. Background spectra of the empty gas cell were then acquired and stored. For elevated temperature work, the temperature was raised and kept constant by a circulating, thermostatted hot water bath (Haake, Berlin). Inlet and outlet ports were wrapped with heating tape which was

connected to a Variac power supply. The heated cell was wrapped in insulation and allowed to equilibrate for 2 to 3 hours before the background spectra were collected. Photoacoustic cells were attached directly to the vacuum line through B10 greaseless fittings (J.Young, England) and pumped down.

The samples for room temperature photoacoustic and absorption spectra were connected directly to the vacuum rack. The connection line of the cylinders of gaseous samples was pumped down. Liquid samples were evacuated with several freeze-pump-thaw cycles. Both sample container and gas cell were isolated from the pump. Stopcocks of each were opened and sample vapour was allowed to diffuse into the gas cell. The sample vapour pressure was closely monitored by a mercury or piezo-electric manometer. Once the optimum pressure was reached, the gas cell stopcock was closed isolating it from the entire system. The remaining sample vapour in the vacuum line was recondensed into the sample container or a waste trap using a liquid nitrogen trap.

For the elevated temperature absorption spectra, the Wilks gas cell temperature was maintained at 89°C. The outlet port of the cell was connected to the vacuum rack and the sample was directly

attached to the inlet port. By opening the stopcock of the sample flask and both the inlet and outlet ports of the cell, the sample could be evacuated by a series of freeze-pump-thaw cycles. Closing the outlet port isolated the sample and cell from the pump and allowed sample vapour to diffuse into the cell. The temperature of the sample flask was gradually increased with a hot water bath to nearly that of the cell. This increased the sample vapour pressure in the gas cell. The higher temperature of the cell ensured that none of the sample condensed on the sensitive optics in the cell. Once the maximum cell pressure was attained, the inlet port was closed isolating the cell from the sample flask. Any residual sample vapour in the transfer line was recondensed into the sample flask with a cold trap.

Once the gas cells were loaded with sample, overtone spectra could be acquired (see Chapters 4 and 5). After the various overtone regions had been collected, the cells were again pumped down for a 1 to 2 hour period. Background spectra of the empty gas cells were again recorded to ensure against any cell contamination. For the absorption spectra taken with the Wilks cell, the comparison of the background spectra before and after data collection provided a check

on the integrity of the cell alignment throughout the complete procedure. In addition, these background spectra were also used to correct for any sloping or curved baselines in the spectra (see Chapter 4).

## CHAPTER 4 : Conventional Absorption Spectrometers

### i) FTIR

All fundamental spectra discussed in this thesis were measured with a Nicolet MX 3600 FTIR data system. The system incorporates an MX-1 Michelson interferometer, a Nicolet 1280 minicomputer, dual CDC 9427H hard disk drives, and a Nicolet Zeta 160 digital plotter. An Epson LQ 1000 dot matrix printer could optionally be connected to the system through RS-232 port A.

The MX-1 interferometer bench is capable of 0.5  $\text{cm}^{-1}$  resolution over a spectral range of 400 - 4900  $\text{cm}^{-1}$ . The bench is a single beam instrument. Background spectra of the empty sample cell were collected and later ratioed against the acquired sample spectra to give absorbance spectra. Infrared absorbance spectra were acquired, manipulated, displayed, plotted, and finally stored using Nicolet's FTIR36 software package.

ii) Beckman

The low energy overtone spectra,  $\Delta\nu_{\text{CH}}=2-4$ , and the high energy liquid phase spectra,  $\Delta\nu_{\text{CH}}=5-6$ , were measured with a Beckman UV5270 near infrared - visible - ultraviolet spectrophotometer. The near infrared source and detector were used for the low energy overtone regions while the visible source and detector were used for the  $\Delta\nu_{\text{CH}}=5-6$  regions.

The Beckman absorption spectrometer was operated under both manual and programmed slit control. In the programmed control mode, the slit width varied automatically to compensate for changes that were detected in the optical throughput of the spectrophotometer. An increase in the cell pathlength or the insertion of a neutral density filter in the reference beam naturally decreased the throughput. In the programmed control mode, this caused the slit to widen and hence decreased the resolution. This effect could be offset by increasing the detector voltages. When scanning the wavelength of the spectrometer in the programmed mode, the resolution varied as function of the spectral profile of

both the detector sensitivity and the lamp source. In some regions this would cause resolution to vary rapidly with wavelength. In the manual mode the resolution also changed as a function of wavelength but usually less dramatically. The resolutions quoted in this thesis correspond to the lowest of the particular spectral scan.

In a typical experiment, low resolution survey spectra were used to optimize cell alignment and pathlength. For these scans the analog absorbance signal was recorded directly onto chart paper as a function of wavelength. When the best signal-to-noise was obtained, the slit width was slowly decreased to improve resolution. This procedure was continued until a suitable compromise between resolution and signal-to-noise was obtained. The final research spectrum was then acquired using the data collection parameters determined from the survey spectra. With the exception of some  $\nu_{CH}=4$  and 5 spectra, slit widths could be kept small enough to not noticeably affect the relatively broad overtone absorption features. In the majority of cases the instrumental resolution exceeded the digital resolution of the data collection software.

The Beckman UV5270 is crudely interfaced to the Nicolet FTIR data system. The spectrophotometer provides a digitized absorbance

signal in a 16 bit BCD (binary coded decimal) format at the rear instrument panel. The digital output can be monitored by the Nicolet 1280 computer through one of its parallel I/O ports. BECKMA, a modified version of FTIR36, contains a macro program for reading in the digital BCD signal and converting it into true digital format. The spectral scan speeds for transferring absorbance spectra to the Nicolet 1280 from the Beckman are limited by the digitization rates of the Beckman, the data transfer rates, and the data processing speed of the macro routine. Digitization rates are controlled from a switch on the rear panel of the Beckman. Typical digitization rates used for spectral acquisition are 50 points/nm and 12.5 points/nm in the visible and near infrared modes respectively. At such rates, scan speeds are constrained to be around  $1/16 \text{ nm s}^{-1}$  and  $1/8 \text{ nm s}^{-1}$  for visible and near infrared spectra.

The UOM data collection macro of BECKMA linearizes the absorbance data on a wavenumber scale. The linearizing process produces spectral files in a FTIR36 format with a digital resolution of  $1.22 \text{ cm}^{-1}$ . In most cases this corresponds to the resolution of the reported spectral traces.

When pathlengths in excess of 15 m were used, the optical

throughput of the sample beam was so reduced that the absorbance reading would be off scale. In these situations a neutral density filter was placed in the reference beam of the spectrometer to bring the spectra on to scale.

In addition to long gas cell pathlengths, spectra were often run at elevated temperatures. This was done to enable higher sample vapour pressures to be used in the gas cell and hence improve the signal. Under the conditions of long pathlengths and elevated operating temperatures, the gas cell tended to produce a nonlinear, sloping baseline. Pathlengths were often chosen as a compromise between those which were long enough to give adequate signals yet short enough to minimize this effect. Despite these efforts, sloping baselines occurred in most of the raw spectral traces.

The sloping baselines produced by the cell could be eliminated by running background spectra of the empty cell, storing them, and later ratioing them against the raw sample spectra. In order for the ratioing procedure to exactly cancel the cell baseline profile, the sample and background spectra had to be recorded under the same conditions. These conditions include resolution, pathlength, and cell alignment.

The spectral adding routine was useful for improving the signal-to-noise of the weak gas phase overtone spectra. Several spectra of the same region can be collected and added. The addition of N scans should improve the signal-to-noise ratio by  $\sqrt{N}$ . The Beckman is a dispersive instrument and data collection times for a single scan range from 10 to 80 minutes. This places practical limits on the number of scans one can collect. Signal enhancements of a factor of 2 to 4 were commonly attained for the weaker, overtone spectra. When this procedure is used in conjunction with the baseline ratioing method, the number of acquired background spectra must be the same as the number of sample spectra to achieve the  $\sqrt{N}$  signal enhancement.

Liquid phase spectra can also have baseline distortions. The higher liquid phase overtones can occur on the shoulder of a low lying electronic transition. In these cases baseline correction routines help remove the sloping shoulder.

The BECKMA ratioing, baseline correction, and spectral adding routines are interactively controlled through the graphics display of the processed absorption spectrum. Once the absorption spectra were processed and plotted with the BECKMA routines, the files

could be stored on the hard disk for further analysis. The data analysis software will be described in Chapter 7.

## CHAPTER 5 : Intracavity Dye Laser Vibrational

### Overtone Photoacoustic Spectroscopy.

#### i.) Introduction to Photoacoustic Spectroscopy. (PAS).

Absorption spectroscopy has been used for over a century to study molecular vibration. The fundamental vibrational transitions which occur in the mid-infrared region ( $400 - 4000 \text{ cm}^{-1}$ ) have traditionally been of the most interest to vibrational spectroscopists. Today's commercial infrared absorption spectrometers are capable of recording the fundamental dipole allowed transitions of even very dilute gas phase samples with high signal-to-noise and resolution. The situation is quite different for recording the high energy (NIR - VIS) vibrational features of molecules. The overtones of the XH-stretching ( $X=C,O,N,S,\dots$ ) modes of the molecule carry most of the oscillator strength in the high energy vibrational regions. The overtones are very weak relative to the XH-stretching fundamental. The first overtone of an XH-stretch is well over an order of magnitude less intense than its fundamental. Each succeeding overtone is typically an order of magnitude less intense than the preceding one. Thus, as one proceeds to the higher

overtone, the absorption decreases very rapidly. In the weak absorption case, a conventional absorption spectrometer must detect very small differences between two large signals. Instrumentationally this is a very difficult detection problem. Ultimately this limits the sensitivity of conventional absorption spectroscopy to between  $10^{-2}$  and  $10^{-4}$   $\text{cm}^{-1}$  absorptivity. Long sample pathlengths and relatively high sample densities are required to record the lower gas phase overtone regions. Even with such efforts, the small absorptivities  $< 10^{-6}$   $\text{cm}^{-1}$  of the high overtone regions are well beyond the capabilities of conventional absorption spectroscopy.

The extreme weakness of the high energy vibrational features of molecules requires an ultrasensitive spectroscopic method to observe them. One such technique is photoacoustic spectroscopy (PAS). The PA effect was first discovered by Alexander Graham Bell in 1880<sup>40a</sup>. He observed that an audible sound is produced when modulated light is incident on an optically absorbing material. Except for the early investigations of this effect by Bell<sup>40b</sup>, Tyndall<sup>41</sup> and Roentgen<sup>42</sup> in the late 1800's, applications of the PA effect remained virtually unexplored until the advent of the

microphone. In the late 1930's, infrared spectrometers which utilized PA detection appeared<sup>43</sup>. By the mid 40's differential PA gas analyzers became commercially available. These designs were capable of detecting CO<sub>2</sub> in N<sub>2</sub> down to a few parts-per-million<sup>44</sup>. Also in the late 40's, PAS became an established technique to measure vibrational lifetimes of gaseous molecules<sup>45</sup>. Despite these early successes, PA techniques vanished by the late 50's, early 60's. PA spectrometers and gas analyzers were overtaken by infrared absorption spectrometers and more sensitive chromatographic methods. It was not until the early 70's that interest was rekindled in the PA effect. Using the various lines of a high power CO<sub>2</sub> laser as the excitation source, Kerr and Atwood<sup>46</sup> as well as Kruezer<sup>47</sup> were able to detect, photoacoustically, trace gas constituents at the sub-part-per-billion level. This work with fixed frequency lasers demonstrated the potential of laser PA methods. The maturing of PAS as an ultrasensitive spectroscopy hinged on the development of tunable laser sources. The progress in tunable dye laser technologies throughout the 70's opened the door to a number of ultrasensitive laser based spectroscopic techniques, including PAS. In the 70's, Stella et al<sup>48</sup> used intracavity, cw, dye laser

photoacoustic spectroscopy to observe gas phase molecular overtone transitions of methane and ammonia. The experimental arrangement was relatively simple yet was highly sensitive. With improvements in cell design and detection system<sup>49</sup>, Reddy, Heller, and Berry in 1982<sup>50</sup> were able to measure up to the 9<sup>th</sup> CH-stretching overtone of vapour phase benzene. This impressive work showed that PAS could be used for studying gas phase overtone spectra of low boiling liquids. The work of Reddy et al as well as that of numerous other groups has now established PAS as an important tool in the arsenal of vibrational overtone spectroscopists.

PAS is just one of a family of methods which can be generally categorized as photothermal or thermo-optical. The photothermal (PT) effect is the heating of a sample due to the absorption of radiation. More precisely, an incident radiation field excites the medium by resonant absorption. Subsequent de-excitation of the excited internal states occurs via a number of possible channels. Through the nonradiative decay processes some of the absorbed energy eventually appears as heat energy in the sample. PT heating gives rise to a number of different effects which in turn provide detection mechanisms for optical absorption. The most direct

method for measuring PT heating is to detect the rise in the temperature of the sample with a thermocouple or other temperature detector. Conventional optical or, as it is often called, laser calorimetry lacks the sensitivity required to measure the weak overtone transitions.

A consequence of PT heating is the production of a refractive index gradient in the sample. Since most materials have positive coefficients of thermal expansion, sample densities decrease with temperature. Thus indices of refraction usually have a negative temperature coefficient. The PT heating arising from a weakly absorbed TEM<sub>00</sub> (transverse electromagnetic) beam of a laser causes a gaussian radial temperature profile about the axis of the beam. The gaussian refractive index gradient in the sample acts like a negative or diverging lens. The propagation of the source beam is affected by this lens which causes it to diverge<sup>51</sup> (self-defocus, thermal bloom). The propagation of any other beam in the vicinity of the excitation beam is also affected by the refractive index gradient. Swofford et al<sup>52a</sup> using a probe beam directed down the axis of the modulated excitation beam monitored the modulated thermal lensing (defocusing) of the probe beam. Thermal lensing spectroscopy (as

this arrangement is called) was used extensively to measure the high overtone regions of transparent liquids<sup>52b,c</sup>. The standard thermal lensing experiment is not sensitive enough to measure the weak lensing arising from overtone absorption in gases. A closely related technique, photothermal deflection (PTD)<sup>53</sup>, however has been used to observe gas phase high overtone CH-stretching transitions<sup>54</sup>. In this arrangement the probe beam is not directed down the axis of the excitation beam. In fact the probe beam need not be colinear with the PT source. For the highest sensitivity however the probe is directed colinearly with the source approximately one beam radius from the axis of the source beam. This is the location of the maximum refractive index gradient. By modulating the excitation source, the path of the probe beam is deflected from its original position in a modulated fashion. The deflection is proportional to the PT heating, which in turn is directly related to the absorption of the sample.

Acoustical waves can also arise from PT heating. Direct photoacoustic (PA) generation can take place through pulsed excitation or continuous wave (cw) modulation. In pulsed excitation an optical pulse is absorbed by the sample, nonradiative processes

convert some of this energy to heat, the localized heating of the sample causes the sample to expand in the vicinity of the pulse. This produces a pressure disturbance in the sample. In a gas this pressure disturbance is detected as an acoustical shock wave in the sample. In the pulsed experiment the acoustical transient is acquired and analysed in the time domain. Acoustical disturbances are typically collected with transient recorders or boxcar integration schemes. Temporal gating techniques generally have to be used for noise suppression.

In cw modulation either the wavelength or amplitude of the excitation source can be modulated. Amplitude modulation is the most commonly used method. The simplest approach to amplitude cw modulation is to chop the output of a continuous excitation source before it is incident on the sample. Modulation frequencies are typically in the  $10^0$  to  $10^3$  Hz. range with a 50% duty cycle chopper (one half of the incident light is rejected by the chopper). The periodic pressure fluctuations caused by the modulated PT heating are detected as acoustical waves in a gas sample. The acoustical signal from a microphone is analysed in the frequency domain by lock-in (phase sensitive) detection electronics. The amplitude and phase

of one or more of the Fourier components of the periodic acoustical signal is measured by these techniques. Narrow bandpass filters eliminate signals occurring at frequencies other than that being analysed. This suppresses the noise in cw modulation PAS.

Both methods of PA generation have their advantages and disadvantages. The advantages of cw amplitude modulation include the high sensitivity of lock-in detection and high excitation duty cycle. The low peak powers of cw lasers result in low PA generation efficiency. Low chopping frequencies require acoustical transducers with superior low frequency response. Microphones typically have poor low frequency response characteristics<sup>55</sup>. In designing or analysing cw PAS systems, thermal diffusion effects and the acoustical boundary conditions may play an important role. The most serious problem in amplitude modulated cw PAS is the ability to discriminate against modulated background heating noise. The major source of this noise is generally from the weak optical absorptions of photoacoustic cell windows. Careful choice of phase in the lock-in detection electronics can reduce some of the window noise background. However, it is usually difficult to completely eliminate it from the sample's acoustical signal.

Pulsed PAS uses high peak power pulsed dye lasers as an excitation source. The efficiency of PA generation is still low but better than that in cw modulation. To detect the acoustical transient, a high frequency response of the acoustical transducer is desirable. The sensitivity of microphones and piezoelectric transducers in higher frequency regions is far superior to their response at low, sub-acoustical frequencies. Since excitation pulses are usually short, acoustical propagation during the pulse is much smaller than the dimension of the sample. The PA pulse shape in most cases is independent of boundary reflections and thermal diffusion effects are usually negligible. Most importantly, in pulsed PAS window noise can often be temporally resolved from the main component of the acoustical signal of the sample. In these cases window noise can be effectively suppressed by carefully gating the detection system. The biggest drawbacks of pulsed PAS are the low duty cycle and the related longer overall data collection times as compared to cw modulation PAS.

Whether pulsed excitation or cw modulation PAS has a higher detection sensitivity depends on the details of the experiment and the sources of noise. In situations where random noise dominates,

cw modulation PAS is usually superior. On the other hand when systematic noises such as window noise dominate, pulsed PAS with gated detection is preferred. Both methods however are capable of high sensitivity. In vibrational overtone PAS, the magnitude of random and systematic noise is high relative to the acoustical signal arising from weak overtone absorption. Both cw and pulsed PAS have been used to measure gas phase high energy vibrational overtone spectra. In this work, cw amplitude modulation PAS was used.

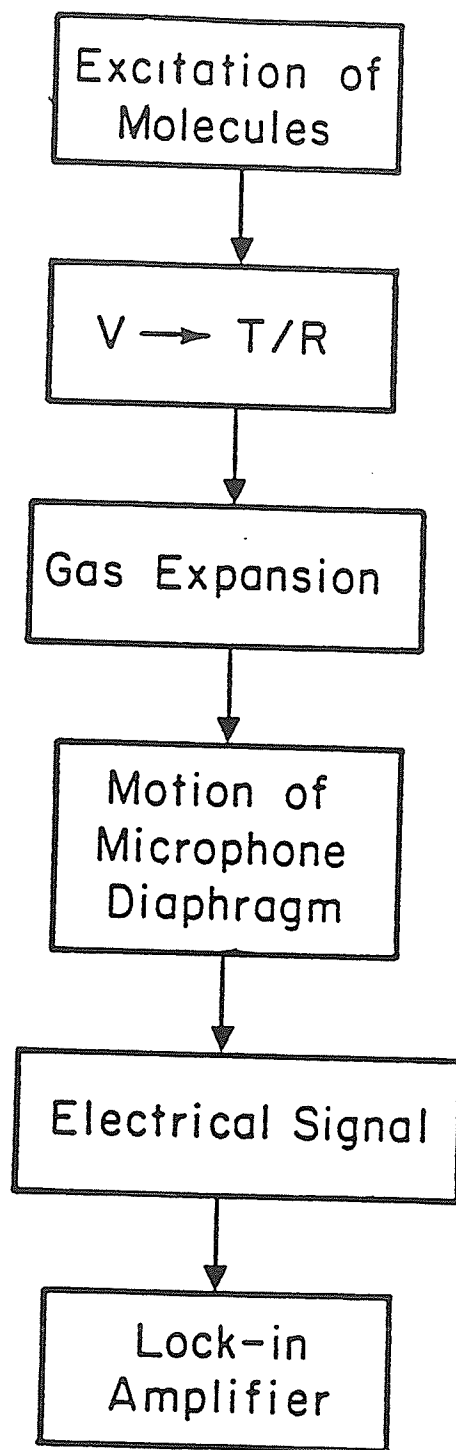
## ii.) Overview of the Analysis of Amplitude Modulated, Continuous Wave PAS

The theory of photoacoustic generation and detection in gases and condensed phases has been extensively reviewed<sup>56-61</sup>. To achieve the desired level of sensitivity requires the optimization of many design parameters of the PA spectrometer. This section simply collects the aspects of the theoretical studies that are relevant to the design of a photoacoustic spectrometer. The theoretical results guide in the construction of the spectrometer. In particular, those facts applying to amplitude modulated, continuous wave excitation PAS will be reviewed.

A detailed theory of photoacoustic detection of vibrational overtone excitation would indeed be quite complex. The considerations involved in such a theory are shown schematically in Figure 5.1. Resonant absorption of radiation which results in the production of highly excited vibrational states is the first step toward PA generation. The second step involves the decay of the excited states. In general, both radiative and nonradiative pathways compete in the the decay process. Excited vibrational overtone

**FIGURE 5.1**

Block diagram of the steps involved in the generation and detection of the photoacoustic effect.



states decay nonradiatively. Although the exact nature of the intra and intermolecular relaxation of highly excited vibrational states is still not completely understood, intramolecular vibrational energy redistribution in polyatomic systems is very rapid<sup>2</sup>. The vibrational energy is rapidly distributed throughout the molecule and eventually appears as excess translational energy through collisional deactivation. In the bulk phase, this is heat.

There are a few factors regarding the excitation and de-excitation of vibrationally highly excited states which have a bearing on the PA experiment. The absorption cross sections of vibrational overtone transitions are very low and their nonradiative decay extremely rapid. Thus even with high power laser excitation, saturation of the transition is unlikely. In addition, the photon flux even in the cavity of the c.w. dye laser is insufficient for multiphoton events to become likely. The rapid decay of the excited state also ensures that practical amplitude modulation frequencies will be much slower than the total decay rate. The almost exclusive nonradiative decay of the highly excited vibrational states means that what little energy is absorbed will ultimately end up as heat energy in the sample. On the other hand, states with high

fluorescence quantum yields are poorly suited to photothermal studies.

The third step in PA generation is the excitation of sound in the gas. Again this has been amply reviewed<sup>62,63</sup>. Morse and Ingard<sup>64</sup> have given the inhomogeneous wave equation relating acoustical pressure and the heat source. The acoustical pressure in a cell due to a modulated heat source is expressed in terms of the normal modes of the gas cell. In the weak absorption limit, for a cylindrical cell geometry and with the excitation beam directed along the axis of the cylindrical PA, only the radial modes of the cell can be excited by the heat source. Typically dye lasers operate in the TEM<sub>00</sub> mode. A TEM<sub>00</sub> beam has a Gaussian profile. The response of a cylindrical PA cell to a TEM<sub>00</sub> beam sinusoidally modulated at frequency  $\omega$  under the conditions described previously at zero-order and at the lowest order radial resonance  $\omega_1$  are given by<sup>58</sup>

$$A_0(\omega) = \frac{i \beta (\gamma - 1) W l}{\omega \left(1 - \frac{i}{\omega \tau_0}\right) V_c} \quad (5.1a)$$

and

$$A_1(\omega) = -\left(\frac{i\omega}{\omega_1^2}\right) \frac{\beta(\gamma-1)Wl}{\left[1 - \left(\frac{\omega}{\omega_1}\right)^2 - i\left(\frac{\omega}{\omega_1 Q_1}\right)\right]} V_c \quad (5.1b)$$

where  $g$  is the heat capacity ratio of the gas in the cell and  $b$  is its absorption coefficient ( $\text{cm}^{-1}$ ) at the excitation wavelength. Heat conduction

from the gas to the walls is accommodated by the damping term  $t_0$ .

The laser power is given by  $W$  while  $V_c$  and  $l$  refer to cell volume and length respectively. In equation (5.1b)  $Q_1$  is the acoustical quality factor for the lowest order radial mode.

The expressions for both resonant and nonresonant PA generation share a number of variables which strongly impact upon the performance of the system. The acoustical pressure is proportional to the laser power. By taking advantage of the much higher power within the laser cavity, an intracavity PA experiment is capable of much greater sensitivity than an extracavity

experiment. Section iii of this Chapter reviews the lasers used in the construction of the PA spectrometer and the steps taken to increase the intracavity dye laser power.

Equations (5.1) guide in the construction of the PA gas cell. In the nonresonant case, the PA signal can be increased by minimizing the cross sectional area,  $A_c = V/l$ , of the cell. The situation is more complex with resonant PA cells. Again  $l$  and  $V$  appear in the numerator and denominator respectively, of the expression for acoustical pressure. The acoustical pressure however, also depends inversely on the resonant acoustical frequency. Cells with low radial resonant frequencies would therefore seem desirable. With cells of cylindrical geometries, the resonant frequencies of the radial modes increase with decreasing cell radius. To decrease the resonant frequency of the lowest order radial mode requires increasing the cross sectional area of the cell. Effective resonant PA cells often employ novel geometries which carefully balance these two factors. Acoustically resonant PA detectors have been carefully reviewed<sup>65</sup>. Chapter 5, section iv describes the series of nonresonant photoacoustic cells used in the experiments.

The last steps in Figure 5.1 involve the detection of the

acoustical pressure. In the case of nonresonant PA generation, the PA signal can be increased by employing low amplitude modulation frequencies. Acoustical transducers with good low frequency response are crucial for high sensitivity applications. The majority of microphones have poor low frequency characteristics. Section v of this Chapter reviews the characteristics of the broad-band microphone used for the acoustical detector as well as the electronics used to process the microphone signal. The monitoring of weak electrical signals in the " $1/f$ " ( $< 100$  Hz.) region is fraught with a number of difficulties. Flicker noise from instrumental amplifiers, noise from the mains, and noise from other laboratory equipment saturate this region. Careful choice of lock-in amplifier detector parameters is necessary in order to optimize the sensitivity of the PA system. These parameters are discussed in some detail in section v.

### iii.) PAS Laser System

In the linear regime, the PA signal is directly proportional to the intensity of the incident radiation field. The incredible advantages in the spectral brightness of laser sources compared to conventional light sources and the tunability of dye lasers makes them an attractive excitation source for an ultrasensitive vibrational overtone photoacoustic spectrometer. In the near-UV, visible, and near-IR, dye lasers have revolutionized optical spectroscopy. By changing excitation sources and dyes, dye lasers offer continuously tunable radiation from 310 - 1200 nm.

Either pulsed or continuous wave (cw) dye lasers can be used as an excitation source for PAS. The merits of the two methods of PA generation were discussed in part i. of this chapter. The PA spectra in this thesis were obtained using amplitude modulated cw PAS. A Coherent Inc. INNOVA 20 argon ion laser capable of 20 W multiline visible output was used to pump a CR-599-01 standing wave dye laser. The argon ion pump laser was operated in both a multi or single visible line mode. Single line operation typically resulted in better dye laser beam quality and stability.

For the intracavity PAS arrangement the output of the INNOVA

20 argon ion laser is amplitude modulated by a mechanical chopper. The chopper unit consists of a Rofin 7505 chopper head and a 7020 control module. The control unit contains the electronics which drives the chopper head. The chopping frequency can be controlled internally by manually setting the control unit or it can be triggered remotely (see Chapter 6). The 7505 chopper head is a two aperture head which gives square wave modulation at a 50% duty factor between 5 and 200 Hz.

A dye laser consists of an amplifying dye medium placed in an optical resonator. Laser output radiation is obtained by having a small transmission leak in the output optic of the resonator. The power of the radiation within the resonator is much greater than that transmitted. A way of increasing the radiation intensity in the PA cell without increasing the source intensity is to place the sample in the optical resonator of the laser excitation source. PA enhancements<sup>65</sup> as high as  $10^4$  or  $10^5$  are possible by performing the experiment in an optical resonator. In low gain cw dye lasers, intracavity PA enhancements are on the order of  $10^2$ . The intracavity PA enhancement is critical for obtaining gas phase vibrational overtone PAS of low boiling liquids.

The CR-599-01 dye laser has an astigmatically compensated folded three-mirror cavity design<sup>66</sup> which is longitudinally pumped by the TEM<sub>00</sub> mode of the argon ion laser (see Figure 5.8). The standard commercially available output couplers in the 535 - 950 nm. region have transmission coefficients of 1 - 5%. Higher reflecting 99+% output couplers (courtesy of Coherent Inc.) reduce the output losses and hence lower the threshold for the cavity. In general this increases the intracavity power of the dye laser. The use of high reflecting output couplers generally improves the PA signal for the intracavity experiment.

The intracavity dye laser power can be increased by increasing the pumping power. For moderate increases of the pump level from threshold, the dye laser power shows a linear dependence on pump power. As the input power increases, the increase in dye laser performance becomes less dramatic. At the critical pump power, the dye laser performance reaches its maximum level. Above the critical pump power the resonator becomes unstable and lasing ceases. Thermo-optic (photothermal) distortions in the dye media represent the main limiting factor in attaining high power cw dye lasers<sup>67</sup>. There are several factors, such as argon ion pumping

configuration, dye laser beam radius, and dye laser cavity alignment which dictate the efficiency of the high power pumped dye laser.

In conventional low power pumping configurations ( $< 6W$ ), the pump beam is generally tightly focussed. Threshold pump intensity shows a quadratic increase with the focussed argon ion laser beam radius<sup>68</sup>. Low thresholds and hence tightly focussed pump beams are important when pumping with low powers. The critical pump power for a given resonator configuration increases linearly with focussed beam radius<sup>68</sup>. For a particular resonator configuration, dye flow system, and dye solution, there is a high pump power and a particular pump beam radius where the dye laser output is the highest. In practice, the best pump beam radius is found by increasing the pump power and focussed beam radius until the dye laser output is maximized.

Adjustment of the dye laser beam and the cavity alignment can improve the high power operation of the laser. Under high pump powers, the dye laser performance improves by increasing the dye laser beam to the argon ion beam ratio. A wider pump beam is generally used in a high power pumping configuration. Thus the dye beam radius should be increased. A beam ratio of one or greater is

preferred.

If the laser is aligned for the standard low power pumping configuration, increasing the pump power distorts the cavity alignment. This distortion is caused by the increased thermal lensing occurring in the dye jet stream. This distortion affects laser stability. Initially the lens influences the inner parts of the dye laser beam. This preferentially distorts the  $TEM_{00}$  mode of the dye laser<sup>69</sup>. The intensity modulation of the pump beam produces temporal distortions of the  $TEM_{00}$  mode. This initiates mode hopping in the dye laser. The onset of dye laser mode hopping generally indicates that the critical pump power has been exceeded. However, the cavity can often be reajusted to partially compensate for the lens distortion.

The laser dyes and the dye flow system require considerable attention under high power operation. The critical pump power increases with an increase in the dye stream flow velocity<sup>68</sup>. However the flow velocity of the stream is limited by the visco-elastic properties of the jet stream where the flow becomes turbulent. Turbulence in the jet stream degrades the stability of the dye laser which adversely affects the performance. Critical flow

velocities depend on the thickness of the jet, jet nozzle construction, and the viscosity of the dye solution. A reduction in the thickness of the jet and a nozzle channel height which decreases as it approaches the exit permit greater jet stream flow velocities. The conventional jet nozzle was replaced by a precision stainless steel, high power nozzle (courtesy of Coherent Inc.). This provides a wider but thinner jet stream of dye across the laser optical axis. The higher dye circulating pressures which could be achieved with this nozzle reduced the residency time of the dye molecules in the pump beam and increased the critical pump power. At circulating pressures that are too high, dye foaming and bubbling can significantly deteriorate dye laser stability. Typically operating pressures for the Coherent Model 591 dye circulating module ranged from 28 to 40 psi depending on the dye solution.

The major problems encountered in the dye solution under high power pumping are the thermal distortions in the stream and thermal degradation of the dye. Dye cooling can markedly reduce both effects. For example, cooling a water based dye solution from room temperature to 3°C reduces the  $dn/dT$  value by a factor of three<sup>70</sup>. The temperature dependence of the refractive index of ethylene

glycol based solutions is less affected by cooling. In all cases however, cooling increases the lifetime of the dye by reducing the rate of thermal degradation. In addition to these effects, dye cooling also tends to increase the viscosity of the dye solution. This permits greater jet stream flow velocities to be used. The dye circulating modules (Coherent Model 591) are equipped with a cooling coil. A temperature controlled circulating bath (Haake model G) was used to cool the dyes to  $6^{\circ}\text{C} \pm 2^{\circ}\text{C}$ . The dyes were prechilled before starting the jet to avoid excess foaming. After prechilling, the jet is turned on and the circulating pressure is increased until the onset of stream turbulence.

In vibrational overtone spectroscopy, the red and near IR (NIR) regions are of main interest. The recent introduction of three new argon pumped red - NIR dyes: DCM, Styryl 9M, and Pyridine 2, have greatly extended the wavelength range accessible to an argon ion pumped dye laser. With the visible and UV laser lines of the argon ion laser, dyes can now be pumped which cover a wavelength range of 400 - 960 nm. ( $25000 - 10420 \text{ cm}^{-1}$ ). The dyes used in this work were Rhodamine 110 (R110), Rhodamine 6G (R6G), DCM, Pyridine 2 (P2), and Styryl 9M (S9M).

with 8W trouble-free. Higher pumping powers can be used if the thermal properties of the dye solution can be suitably modified. Reducing the  $dn/dT$  of the dye solution will markedly increase the critical pumping power. Water based dye solutions cooled to 3°C should be able to be pumped by 100W cw before the thermal lens distortion destroys the lasing action<sup>70</sup>. Unfortunately most dyes are poorly soluble in water. Also the low viscosity of water makes it ill suited for use in a jet. Alternatively water based detergents or surfactants are used as additives to the ethylene glycol dye solution. Some viscosity is usually sacrificed for the decreased sensitivity to high power pumping. The reduced viscosity of the solution generally requires a decrease in the jet flow velocity. This reduces the critical pumping power. There is generally a compromise between the decreased thermal sensitivity of the dye solution and the decrease in the dye flow velocity which ultimately determines the critical pump power in these ethylene glycol and water based additive dye solutions. High pump power dye solution mixtures have been successfully pumped with 200W cw power<sup>71</sup>.

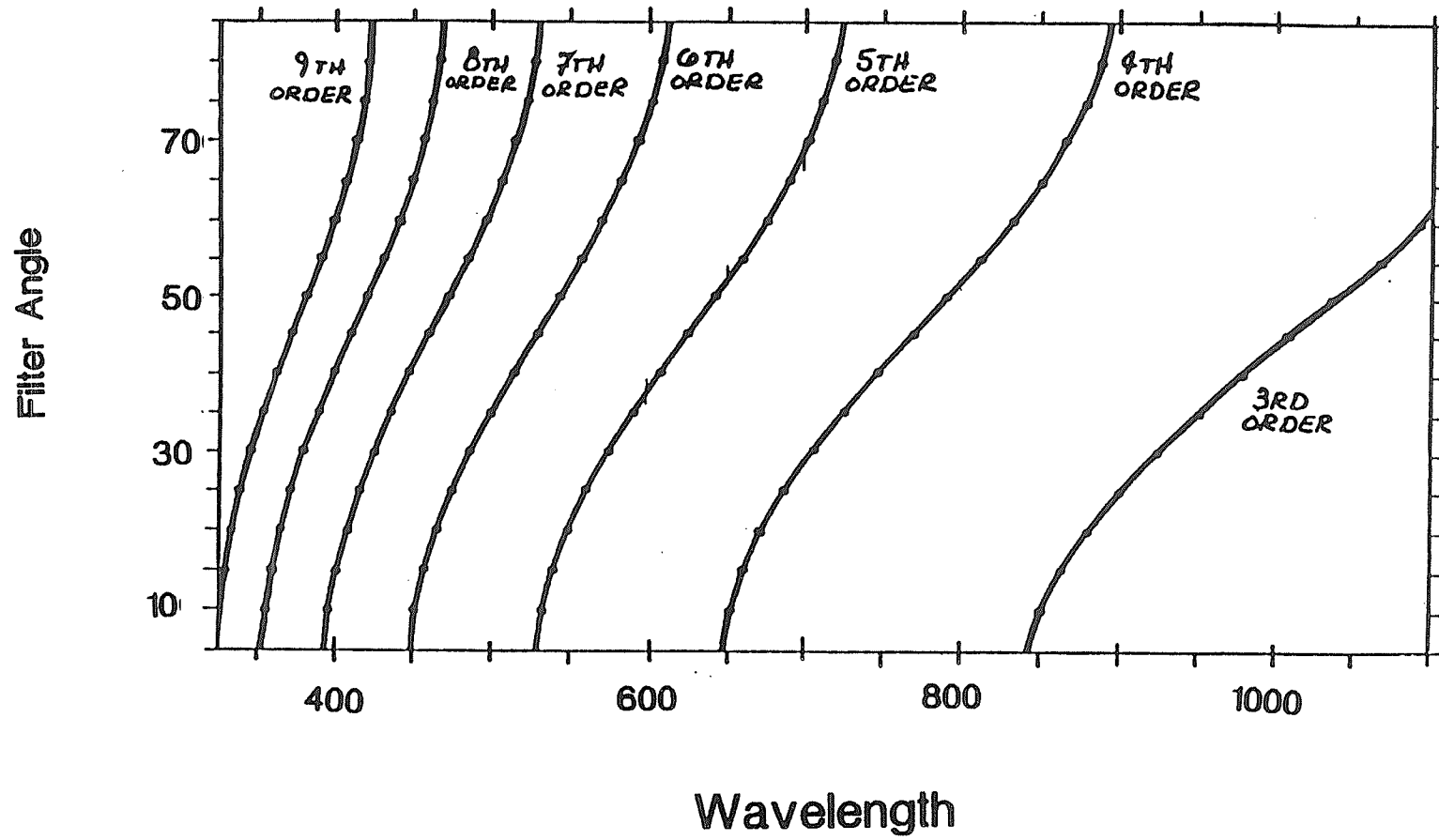
Broadband tuning of the CR-599-01 is accomplished with a three plate birefringent filter<sup>72</sup>. The commercial birefringent filter

has a 1:4:16 plate thickness ratio, with the thinnest plate having a 0.34056 mm thickness. The filter tunes smoothly across 310 to 1080 nm with an optical bandpass of 40 GHz (1.33 cm<sup>-1</sup>) or less. The birefringent filter is placed inside the dye laser cavity with the plates oriented at Brewster's angle. The filter exhibits insertion losses ranging from 3 to 10% depending on its alignment and the wavelength region. Once installed in the cavity, the filter has precise, repeatable, but nonlinear tuning over the various filter orders. The tuning curves of the third to ninth filter orders are reproduced in Figure 5.2.

Smooth tuning over the entire wavelength range of the gain medium is desirable. In the low gain regions when the PA cell is in the laser cavity, the wavelength often jumps back towards the peak of the tuning curve. The source of these tuning discontinuities is probably because the most prominent wavelength of the secondary passband of the filter at that particular filter angle coincides with a high gain region of the dye medium<sup>73,74</sup>. Despite the reduced transmission of this passband through the filter, oscillation at this frequency is preferred over that of the primary band. Most importantly for intracavity work, the presence of the intracavity PA

**FIGURE 5.2**

Transmission of the Three Plate Birefringent (1:4:16) Tuning Element. (Thickness of Plate 1 = 0.34056 mm.)



cell increases the cavity losses and lowers the effective gain of the dye medium. This reduces the tuning range of the dye. The tuning range of the filter can be increased by reducing cavity losses with the high reflecting optics and by carefully aligning the PA cell and dye laser optics.

Smooth tuning can be further disrupted by the presence of the intracavity PA cell. The primary transmission window of the filter is generally rather wide compared to the actual laser linewidth. Laser dyes behave essentially as homogeneously broadened gain media. They have a natural tendency to lase only at a single, most favorable frequency. Thus within a particular transmission window, the laser has a preferred narrower lasing window. Small deviations in the PA cell transmission can give rise to tuning glitches on the order of  $10 \text{ cm}^{-1}$ . Maintaining smooth laser tuning to within the laser linewidth requires either highly uniform transmission over an area of the PA cell windows and/or the PA cell windows to remain stationary with respect to the intracavity laser beam. The detailed information about PA cell window materials and their effects on the PAS system will be discussed in the following section.

#### iv) PA CELL DESIGN

Optimal photoacoustic cell design depends on the purpose of the PA system. In this case the main purpose of the system is to measure the absorption of various vapor phase samples with the greatest possible sensitivity. The design of a general purpose cell with high sensitivity depends on a number of competing factors.

PA cells can be divided into two categories, resonant and nonresonant. Resonant photoacoustic cells are designed such that the acoustical modes of the cell, in particular the lowest order radial mode, have frequency ranges which are compatible with the modulation frequencies of the excitation source. Acoustical disturbances at a resonant frequency of the cell will be enhanced by the acoustical quality factor  $Q_i$  of the  $i$ 'th mode of the cell. The resonant enhancement of the PA effect however is also inversely proportional to the magnitude of the resonant frequency  $\omega_i$ . Radial frequencies are inversely proportional to the cell radius. Increasing the cell radius in order to attempt to increase the resonant enhancement of the photoacoustic signal, increases the volume of the cell. The PA signal is inversely proportional to the volume of the

cell. A successful resonant PA cell design must carefully balance these two criteria. In general, the resonant photoacoustic approach requires high Q's in order to offset the higher frequencies and larger volumes associated with these cells.

In practice, the resonant approach presents difficulties in designing general purpose cells. Resonant frequencies of the cell not only depend on its geometry but also on the speed of sound in the cell. This latter factor depends on both the pressure of the gas in the cell as well as the thermodynamic properties of the gas. The optimal resonant cell geometry will therefore change for different samples and different pressures. This practical difficulty outweighed the possibility of obtaining moderate resonant enhancements of the PA signal. Nonresonant cells were therefore used in all experiments.

Nonresonant PA cell geometries are typically cylindrical. As in the resonant case, the pressure response of a nonresonant cell has an inverse volume dependence. This would suggest that cells should be made as small as possible. There are however some practical considerations which must be taken into account in the design. One such consideration is that the laser excitation beam has a finite radius. In order for the intensity profile of the Gaussian TEM<sub>00</sub> beam

not to be significantly disturbed, the ratio of the cell radius to beam radius must be about a factor of five. In the intracavity design, small cell cross sections can make the optical alignment of the cavity extremely difficult and in fact degrade laser performance due to the attenuation of the TEM<sub>00</sub> profile. Cross sectional areas of intracavity PA cells should be small yet not small enough to make alignment inordinately difficult or significantly degrade the performance of the laser. An inner diameter of between 0.5 to 1 cm proved to be suitable for the intracavity PA cells.

The optimal cell length is again determined by a number of competing factors. The PA signal strength is proportional to the power absorbed. Increasing the pathlength of the chamber increases the amount of radiation absorbed. A persistent difficulty in achieving ultra high sensitivity in AM cw PAS is the presence of a background signal arising from the absorption of the excitation beam on the sample cell windows. This background signal is proportional to the excitation intensity and typically determines the sensitivity limit when high intensity laser excitation sources are used. The effects of window heating are minimized by increasing the pathlength of the PA cell. An increase in length obviously increases

the cell volume which in turn deteriorates the pressure response of a nonresonant cell. The optimum cell length is a careful balance of these parameters which again depends on the particular application. In these investigations lengths of between 10 to 15 cm were used for the intracavity cells.

In addition to the geometry of the cell, the cell components are important in determining the ultimate sensitivity of the system. Window noise has already been cited as a major source of noise in the experiment. Scattering of the incident radiation by dust and aerosols also gives rise to a background PA signal. Some component of the scattered radiation is absorbed by the cell walls. Surface absorption on the cylindrical walls contributes an additional pressure signal in the cell. Certain cell and window materials have definite advantages in PAS. The thermodynamic properties of sapphire for instance make it six times more effective at reducing the effects of window noise over the conventional quartz windows. The expense of sapphire windows however discourages their use. In order to minimize reflective losses at the window boundary, the chosen window material should be mounted at Brewster's angle. Scratched window surfaces tend to increase the scattering noise,

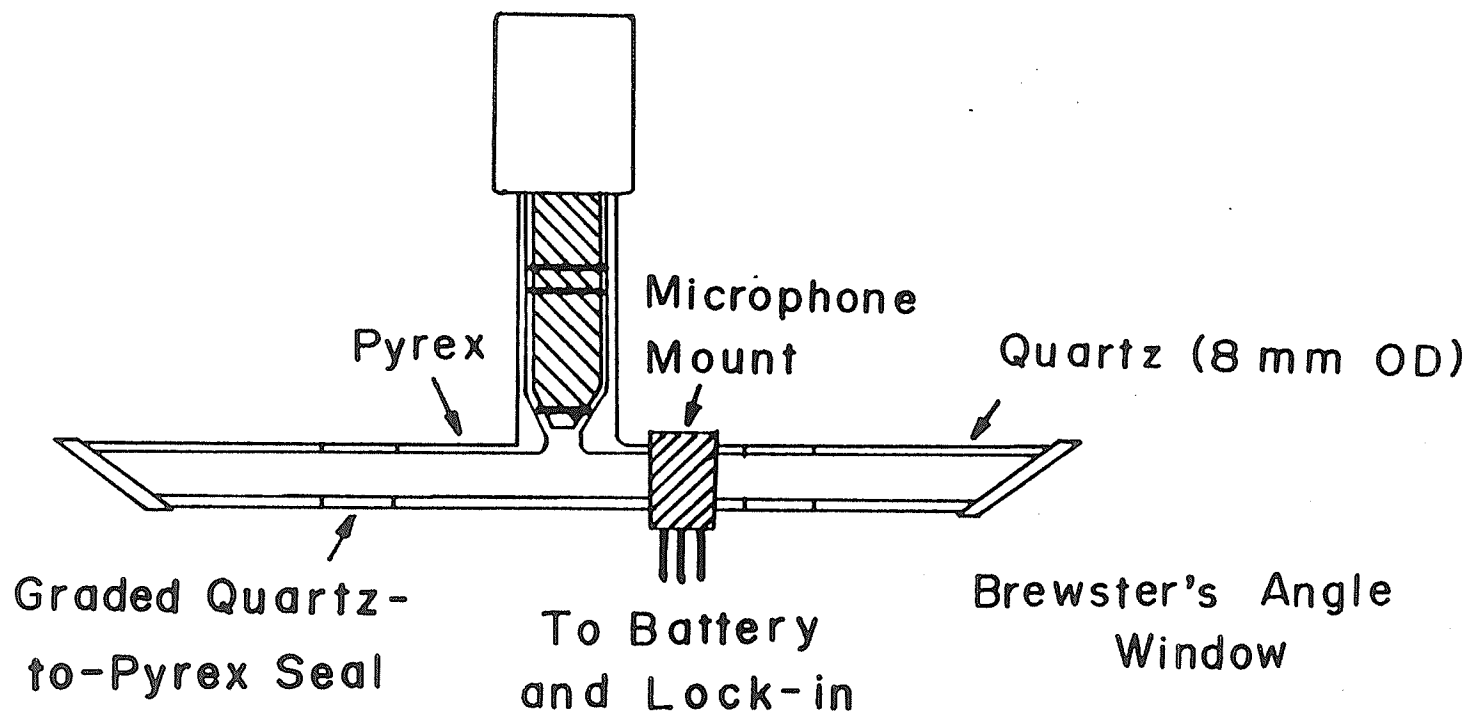
while grease or other window contamination usually results in increased window noise. Clean windows are therefore essential in a high sensitivity design.

Surface absorption at the cylindrical walls of the PA cell can be minimized by choosing the appropriate building material. Cell chambers constructed of copper or silver are preferred over aluminium designs. The difficulties associated with the construction of a metal-glass cell often leads to all-glass designs. In these investigations, metal PA cells were not built; instead, several all-glass designs were used.

The first all-glass cell which we built was based on a design described in Wong's thesis<sup>75</sup> (see figure 5.3). The main section of the cell chamber consists of a 6 mm i.d. pyrex tube to which a greaseless 4 mm stopcock (J. Young Glass) is attached. A rectangular hole for the microphone detector is cut in the center of the tubing. Quartz windows (Lambda/Airtron BW-10) are mounted at Brewster's angle on small sections of quartz tubing with glass transfer tape (Vitta Corp G1015). The quartz tubing is attached to the central part of the chamber through graded quartz-to-pyrex seals. A total cell length of around 12 cm is typical.

**FIGURE 5.3**

Illustration of the "Single-piece", non-resonant photoacoustic cell.



This "single-piece" cell design has several disadvantages. The windows are difficult to remove and clean in this design. Window cleaning was restricted to flaming of the windows in an oxygen rich flame. Although flaming reduced the window noise in newer windows, the magnitude of this background signal tended to become greater as the windows aged. The flaming of old windows only marginally improved their performance.

The single most serious problem with this design in an intracavity experiment is the cell alignment mismatch with the resonator. This results in large insertion losses. The misalignment arises from distortions introduced during the cell construction and the positioning of the cell in the cavity. The quartz tubing to which the windows are attached has small deviations in the cutting angles. Mounting the windows flushly against the tubing with the transfer tape is difficult. These errors tend to spoil the Brewster's angle and parallel window orientation. Attaching the tubing to the central pyrex body with the graded seals also spoils the alignment. All of these factors increase the reflective and scattering losses at the windows.

The alignment distortions produced during the construction of

the cell and the alignment problems encountered during the positioning of the cell in the cavity are amplified by the choice of PA cell windows. The set of Brewster windows used initially were crystalline quartz. Crystalline quartz is a uniaxial, birefringent crystal<sup>76</sup>. A low gain laser with Brewster angle elements in the cavity lases in a TM linearly polarized mode. TM polarized light incident on a birefringent plate oriented at Brewster's angle suffers no decrease in transmitted intensity when the optic axis of the crystal is perpendicular to the ray axis of the light beam. If however the optic axis of the crystal is distorted from this orientation some of the incident TM beam is transformed into a TE component. The power lost to the TE component is no longer available to stimulate lasing of the TM mode<sup>72</sup>. The birefringent losses introduced by the distortions of the optic axis of the windows further reduce the performance of the laser. In addition to the birefringent losses, distortions in the alignment of the optic axis of the windows also interfered with the smooth tuning of the birefringent filter. These tuning discontinuities proved to be even more troublesome than the birefringent losses.

To facilitate cell window cleaning and improve dye laser

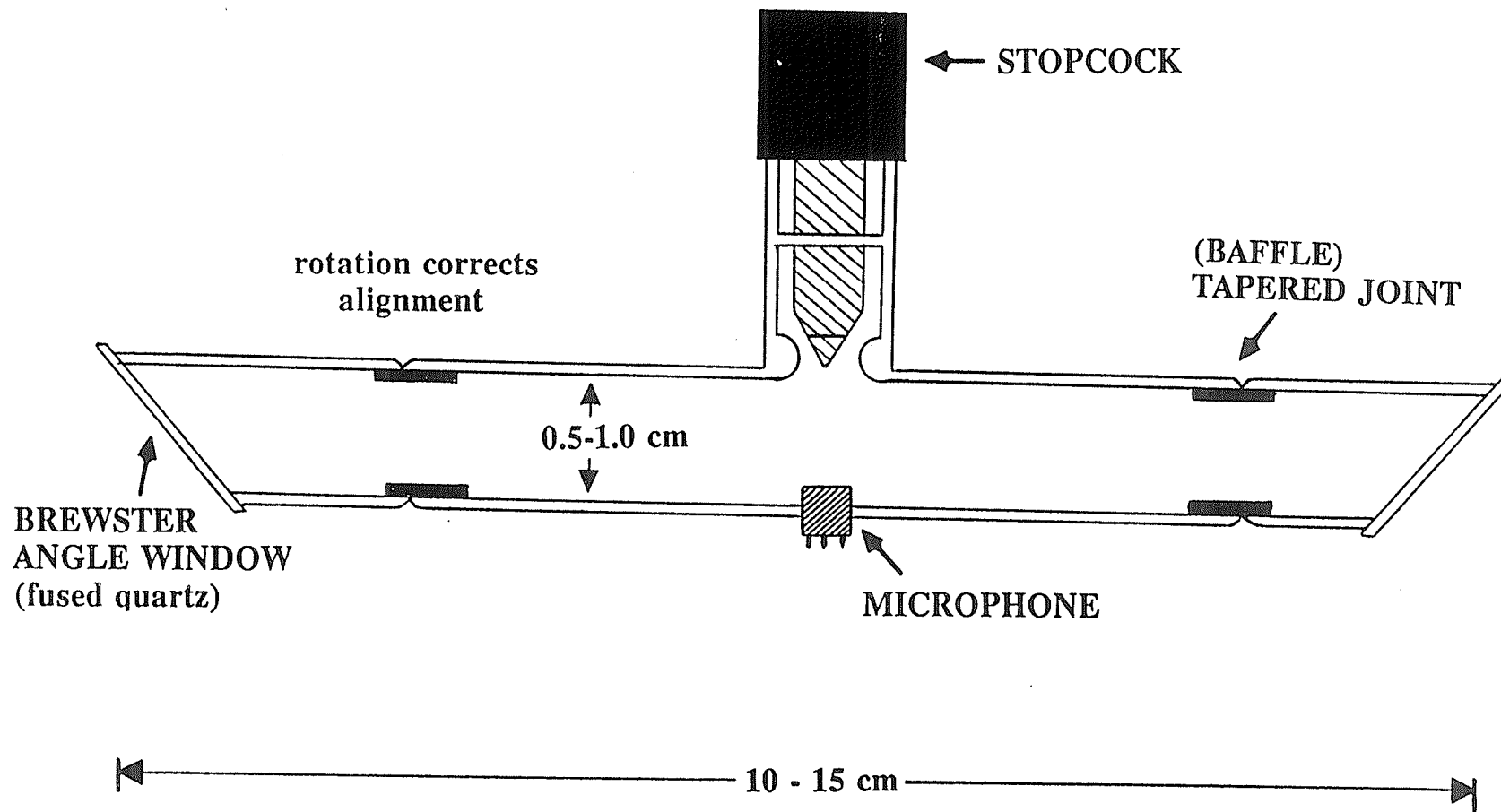
performance, a greaseless "multi-piece" PA cell with fused silica windows was designed (see figure 5.4). The central tube section is of the same design as given above with the one exception that at the ends of tube there are female B10 greaseless o-ring joints. The windows are epoxied with low vapor pressure glue (Torr Seal, Varian) at Brewster's angle to small sections of pyrex tubing fitted with male B10 o-ring joints. The sections are held together with a set of o-ring clamps.

In this multi-piece design, the window sections could be unclamped from the central section of the PA cell which housed the sensitive acoustical detector. A flameless heat gun could be used to remove the epoxied windows. Since the windows sections could be physically separated from the main cell section, this heating did not degrade microphone performance. Cleaned or fresh windows could be installed by again epoxying them to the window tube.

Insertion losses could be reduced using this design by adjusting the window alignment in the o-ring joints. The central cell section was placed in an intracavity cell holder. Vertical and horizontal adjustments were made to center the cell bore along the lasing axis of the dye laser. Cell window sections were then

**FIGURE 5.4**

Illustration of the "Multi-piece", photoacoustic cell.



clamped to the center section and adjusted to maximize the dye laser power. Minimizing the insertion losses due to the cell in this fashion markedly increased the sensitivity limits of the spectrometer over the previous "single-piece" design.

The last design that we tested was very similar to the previous multi-piece design. The main difference was that ground-glass B10 joints were substituted for the clamped o-ring joints. Unlike the previous designs, the joints required small amounts of grease. Small amounts of low vapour pressure Apiezon N grease (Apiezon Products Ltd.) were used to lubricate the joints. Since the presence of grease tended to decrease the useable lifetime of the optical windows, the use of inexpensive window material is recommended. Windows were again epoxied at Brewster's angle to removable window tubes to facilitate cleaning. Windows were frequently replaced. Upon replacement, the entire cell was cleaned to remove any grease that had migrated from the joint region. The ground-glass joint design permitted easy adjustment of the window alignment. By carefully epoxying the windows flushly to the window tubing, and by making the horizontal, vertical, and window adjustments, reductions as low as 10% to 15% in dye laser output

could be achieved. The majority of PA spectra reported in this work were taken with this final cell design.

#### v.) PA Detection Scheme

The intracavity PA spectrometer is specifically designed to measure the very weak overtone transitions of molecules in the vapour phase. A high sensitivity PA detection scheme is paramount for observing these transitions. The acoustical transducer is a critical component of such a detection scheme. Microphones are the most commonly used acoustical transducer for gas phase PAS. The ideal acoustical transducer for PAS must conform to a strict set of requirements. The inverse volume dependence of the PA signal along with the intracavity design place constraints on the size of the PA cell and hence the microphone. The  $1/f$  signal dependence encountered in nonresonant PA detection ideally requires microphones with a particularly sensitive low frequency response. High sensitivity microphone designs are often achieved at the expense of reduced microphone bandwidth and increased size<sup>77</sup>. The low frequency response of most microphones is poor, making them ill suited for use in PA detection systems<sup>78</sup>. The microphone used in these investigations, Knowles Electronics Model BT-1759, satisfies most of the requirements for a PA acoustical detector.

The Knowles BT-1759 microphone is small (5.6mm x 8.4mm x 2.2mm) making it suitable for compact photoacoustic cell designs. The integral high impedance FET preamplifier gives the microphone high sensitivity, low noise characteristics, and a widened bandwidth. The sensitivity of the BT-1759 peaks to 14 mV/PA at 10 kHz, levels off to 10 mV/PA in the 100 Hz - 3 kHz range, and falls off below 100 Hz. The optimum PA modulation frequency turns out to be a trade off between the  $1/f$  signal dependence of the PA effect and the fall off in the low frequency response of the microphone. The highest overall PA detection sensitivity with a BT-1759 microphone as the acoustical transducer occurred at modulation frequencies in the 10 - 40 Hz range.

The PA component of the electrical signal from the microphone is small ( $< 1$  mV) and deeply buried in noise. The noise arises from various acoustical and electrical sources. The low frequency region used in cw PAS is subject to large flicker or  $1/f$  noise. The harmonics and subharmonics of electrical interference from the mains can be significant. The modulation of the PA signal which is intrinsic in a AM cw PA experiment provides a means of distinguishing the signal from noise. When a signal has such a

distinctive time variation, lock-in or phase sensitive detection (PSD) provides a means of signal recovery even under extremely adverse signal-to-noise (S/N) conditions.

Very simply, a lock-in amplifier can be thought of as consisting of a mixer followed by a low pass filter. PSD is driven by a reference signal which is coherent (same frequency  $\omega_r$  and phase) with the input signal. The switching circuitry driven by the reference signal mixes the input and reference channel signals in such a way that the d.c. component of the output is proportional to the magnitude of the input signal occurring at the reference frequency. The a.c. components of the output signal correspond to input signals outside the reference frequency. These a.c. components are rejected by the low pass filtering stage of the lock-in amplifier. The magnitude of the d.c. output also depends on the relative phase difference between the input and reference signals. The output is a maximum positive and negative value at a  $0^\circ$  and  $180^\circ$  phase difference respectively. The output is zero at a phase difference of  $90^\circ$  or  $270^\circ$ . The lock-in amplifier discriminates against noise both in terms of the frequency and phase difference between the input and reference waveforms.

In the photoacoustic studies, the electrical signal from the BT-1759 microphone is amplified by an EG&G Princeton Applied Research (PAR) model 117 differential preamplifier and processed by a PAR model 124A lock-in amplifier. The square wave reference signal is supplied either internally from the VCO (voltage controlled oscillator) of the lock-in or externally with the VCO output of the Rofin 7020 mechanical chopper. In the former arrangement the reference channel of the lock-in is switched to the internal mode and the Rofin chopper is driven in the external mode. The chopper "sync" input is driven by the reference channel output with the chopping frequency directly controlled from the reference channel panel. In the external reference mode, the Rofin chopper is internally triggered. The chopping frequency is manually controlled with a 10 turn potentiometer on the chopper control unit. The sync out signal from the control unit is sent to the reference input of the lock-in. Both external or internal operation provides a suitable reference signal for PSD.

A lock-in amplifier acts as a very narrow bandpass filter in that only the component of the input signal occurring at the reference frequency is detected<sup>79</sup>. Despite this lock-in filtering,

preconditioning of the input signal in the form of broadband filtering is important under poor S/N conditions and in the recovery of low frequency signals<sup>80</sup>. The PAR model 124A lock-in amplifier provides low pass, high pass, notch, and bandpass broadband filtering capabilities. In phase sensitive detection, there are transmission windows for the input signal at the odd harmonics of the reference frequency. Although the higher order terms are attenuated, they can still be a substantial source of noise. Thus, in cases where no prefiltering is used, the modulation frequency must be judiciously chosen such that noise sources are minimal at the modulation frequency and the higher order odd harmonics. Low pass filters, which reject frequencies at  $3\omega_r$  and above, eliminate the high order noise acceptance windows. Since flicker or  $1/f$  noise has mainly low-frequency content, high pass prefiltering can greatly increase the dynamic reserve of the amplifier. For maximum dynamic reserve and elimination of high order transmission windows, bandpass preconditioning is usually carried out. The bandpass filter is centered on the modulation frequency with the filter quality factor (Q) depending on the stability of the modulation frequency. Both the central filter frequency and the Q can be set from the front panel of

the signal channel.

The stability of the output signal from the lock-in is controlled by selecting the time constant for the final low pass filtering stage of the lock-in amplifier. The time constant is switch selectable between 1 ms and 300 s with a choice of -6 or -12 dB/octave rolloff. Through these settings the output response can be tailored between convenient measurement times and the required output S/N. For PAS, data collection time constants ranged from 10 ms to 1 s with -12 dB/octave rolloff.

The general procedure for detecting the PA component of the microphone signal can be summarized as follows:

- Set the signal channel of the 124A lock-in to the lowest sensitivity (500 mV, full scale deflection) setting. Switch the lock-in to the bandpass mode and set the filter Q to 100. Turn the lock-in power on.
  
- If the internal VCO is to be used as a reference, switch the reference channel to internal and select the modulation frequency from the reference panel. Connect

the reference output to the sync input of the Rofin chopper control unit, and switch the chopper control unit to the external mode.

- If an external reference is to be used, switch the Rofin chopper control unit to internal and adjust the chopping frequency with the control unit potentiometer. Switch the reference channel to external and connect the sync out of the chopper unit to the reference input.
  
- Once the chopping frequency has stabilized, adjust the bandpass filter center to the modulation frequency. If the modulation frequency drifts, decrease the filter Q.
  
- Switch the lock-in into the Hi.Dyn. Range PSD mode and connect the output of the microphone to the single-ended "A" input of the model 117 preamplifier.
  
- Once the instrument has stabilized and the signal has locked, the time constant can be temporarily reduced to

1 - 10 ms to decrease response time.

- To find the PA signal the gain can be slowly increased while scanning the phase until a d.c. signal is detected. Once a signal is detected the phase shift is adjusted to maximize the lock-in response. Blocking the pump laser output should of course eliminate the lock-in signal. Scanning the dye laser wavelength should produce the desired absorption profile. By manually scanning through the desired wavelength range, the optimal gain and phase of the lock-in can be adjusted. Increase the the time constant to obtain the desired stability in the lock-in output. With these adjustments, one is now ready to collect a PA spectrum.

Photoacoustic spectra are generally normalized. This involves the measurement of the PA signal amplitude divided by the excitation energy as a function of wavelength. In cases such as overtone excitation where much of the excitation energy decays nonradiatively, the normalized PA spectrum is proportional to the

linear absorption spectrum. The background or normalizing signal in the intracavity experiment is a signal which is proportional to the intracavity dye laser power. One method to monitor intracavity power is to measure the intensity of the light reflected off the Brewster angle window of the PA cell. The scattered light is passed through a polarizer to filter out spurious fringes arising from the birefringent filter. The filtered light is passed through a neutral density filter before being detected with a photodiode. The neutral density filter prevents the photodiode response from being saturated. The photodiode signal is then processed by a PAR model 128A lock-in amplifier. Again the chopper or internal VCO of the PAR 124A lock-in provides the reference signal. The output of the model 128A lock-in is proportional to the component of the photodiode signal occurring at the reference frequency. The background signal is to be recorded and later ratioed with the PA signal to produce normalized PA data. Difficulties in using this signal in the normalization of PA signals stem from the wavelength dependence of the photodiode response, the poor NIR (near infrared) sensitivity of the diodes, and a lack of knowledge of the spectral characteristics of the Brewster windows used in the cell. A second

the dye laser. Over the dye gain curve, the variation in the transmission of a standard dye laser output coupler is typically 4% or less. The largest changes in transmittance occur in the low gain regions of the dye (the output coupler coatings are specifically designed for a particular dye). The higher cavity losses due to the presence of the intracavity PA cell will typically not permit lasing in these lower gain regions. The variations in transmittance of the output coupler during a PAS scan are therefore small and the dye laser output is very nearly directly proportional to the intracavity power. The dye laser output was measured with a Coherent Model 210 pyrometer. The pyrometer has a calibrated, wavelength independent response of 1 mv/mW. The pyrometer output is recorded and later ratioed with the processed PA signal to produce a normalized PA spectrum. The details of the PA spectral processing software will be discussed in Chapter 7.

## vi) PA Spectrometer Performance

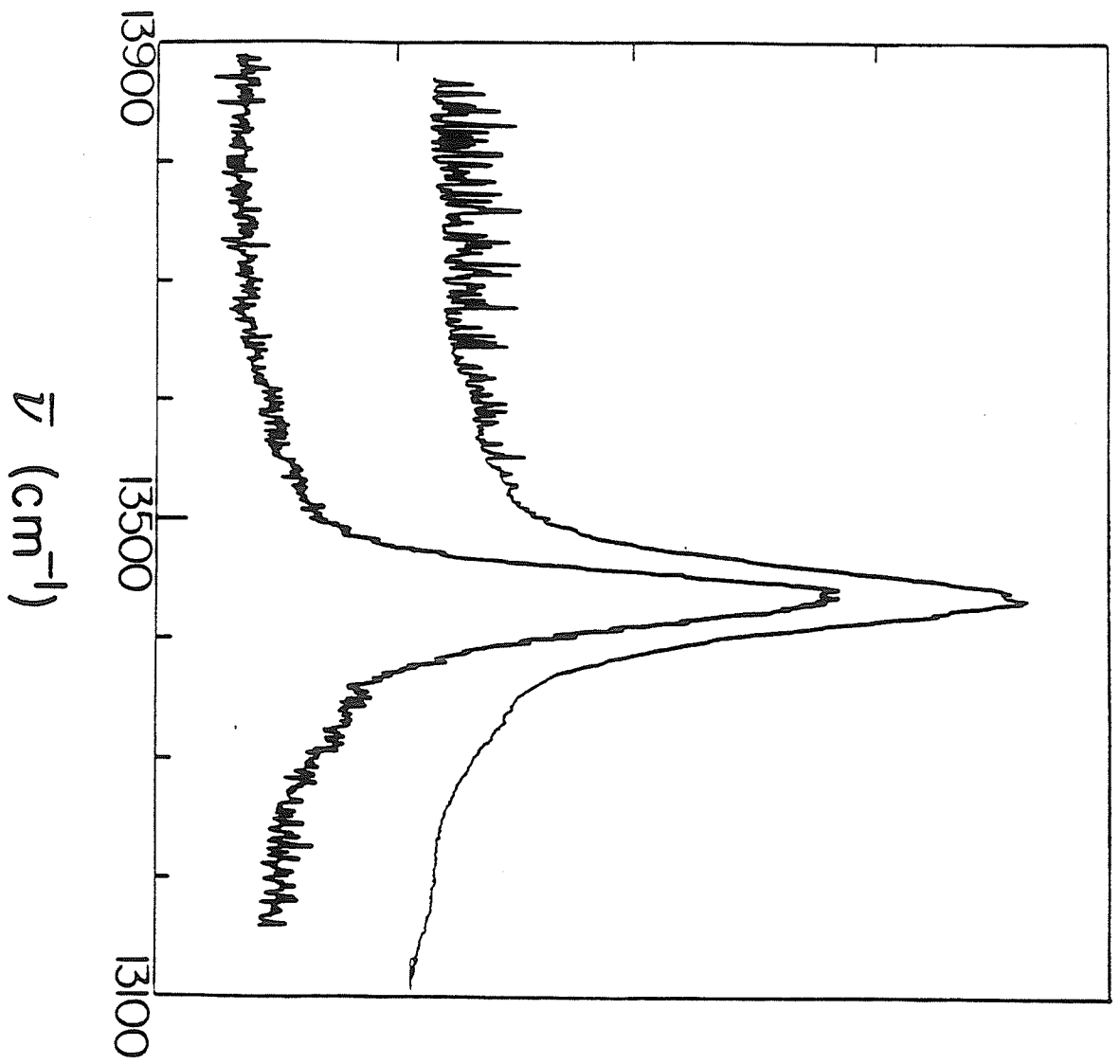
Perhaps the most dramatic way to demonstrate the sensitivity of the intracavity dye laser photoacoustic spectrometer is to compare spectra obtained by conventional absorption spectroscopy and those obtained with the photoacoustic spectrometer. Figure 5.5 compares the absorption and photoacoustic spectrum of the  $\Delta\nu_{CH} = 5$  region of neopentane. The PA spectrum has the same appearance as the spectrum taken by conventional absorption spectroscopy. The neopentane absorption spectrum was measured at 660 Torr pressure with a gas cell pathlength of 11.25 m. The photoacoustic spectrum of the same region of neopentane was measured at 68 Torr pressure and a 10 cm pathlength. The series of small spikes to the high energy side of the methyl CH stretching overtone transition are calibrating lines from the trace of water in the PA cell. A true indication of the high signal-to-noise ratio in the PA spectrum is apparent in the low energy wings of the methyl overtone transition. The noise level in the neopentane absorption spectrum is higher than the PA spectrum despite the  $10^3$  factor in effective sample

**FIGURE 5.5**

The  $\Delta\nu_{\text{CH}} = 5$  overtone region of neopentane.

- lower trace : Gas phase absorption spectrum measured at a pressure of 660 Torr and with a pathlength of 11.25 m.
- upper trace : Gas phase photoacoustic spectrum measured at a pressure of 68 Torr and with a 10 cm. pathlength.

ABSORBANCE



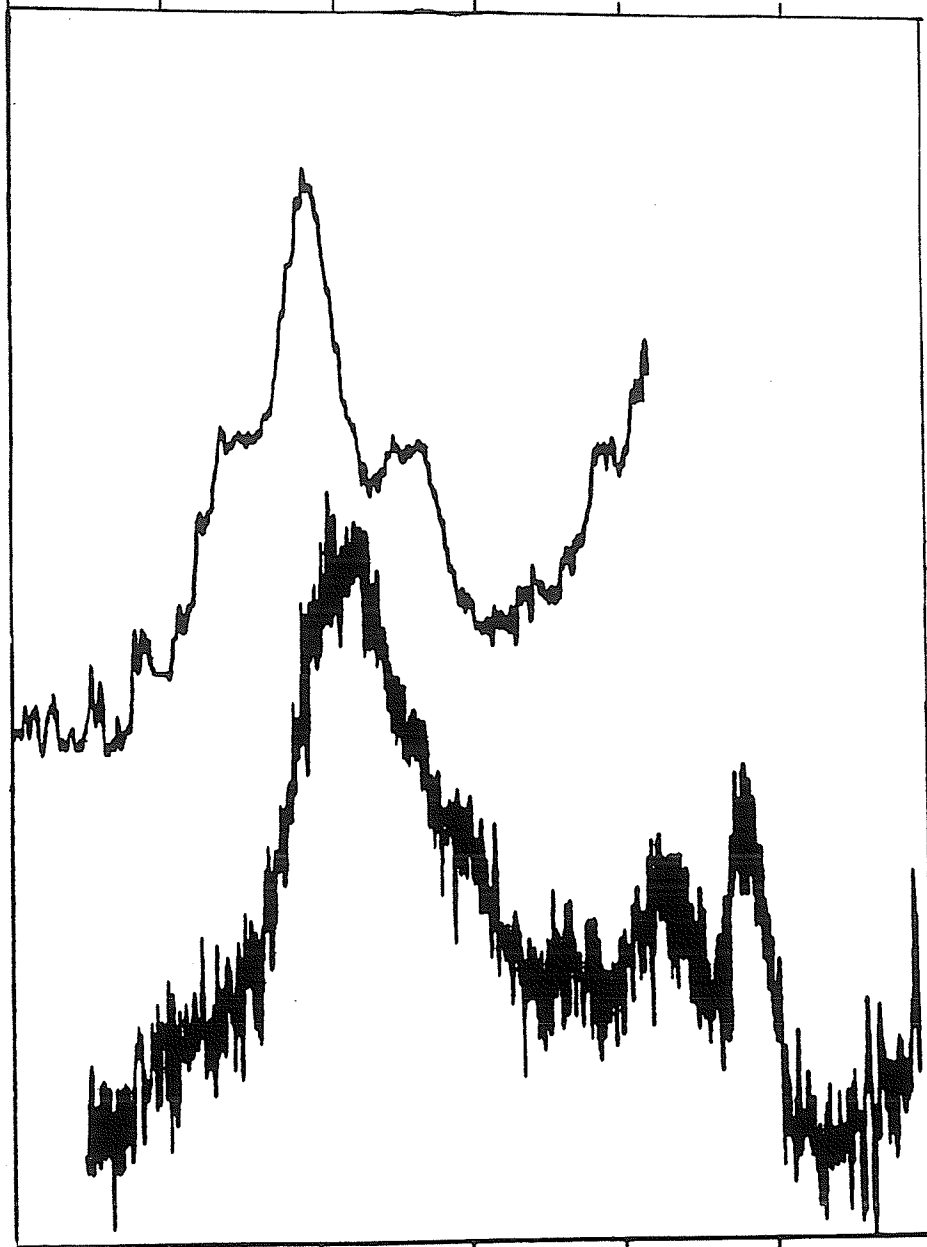
absorption density. Figure 5.6 more dramatically demonstrates the enhanced sensitivity of the PA spectrometer. The conventional gas phase overtone absorption spectrum of the  $\Delta\nu_{\text{CH}} = 4$  region of o-xylene<sup>134</sup> is presented in the lower trace of Figure 5.6. The spectrum was recorded using a 9.75 m pathlength with the gas cell heated to 86°C to give an increased vapour pressure. The o-xylene absorption spectrum is the sum of ten scans. The upper trace of the figure reports the room temperature, photoacoustic spectrum of the aryl  $\Delta\nu_{\text{CH}} = 6$  region of o-xylene. The PA cell pathlength was again 10 cm. The  $\Delta\nu_{\text{CH}} = 6$  aryl transitions are intrinsically two orders of magnitude less intense than the corresponding  $\Delta\nu_{\text{CH}} = 4$  transitions. The vapor pressures of o-xylene in the two experiments differ by slightly more than an order of magnitude and there are nearly two orders of magnitude difference in sample pathlength.

These examples are typical. With the intracavity dye laser photoacoustic spectrometer one can quite easily achieve a thousand-fold or greater increase in sensitivity over the Beckman spectrophotometer. Conventional absorption spectroscopy is limited to absorptivities of  $10^{-2}$  to  $10^{-4}$  cm<sup>-1</sup>. The intracavity design extends the capabilities of photoacoustic spectroscopy to enable the

**FIGURE 5.6**

- lower trace : Gas phase absorption spectrum of o-xylene in the  $\Delta\nu_{\text{CH}} = 4$  overtone region. The lower trace represents a sum of 10 spectral scans measured at  $T = 89 \text{ }^\circ\text{C}$ , a sample pressure of 370 Torr and a cell pathlength of 9.75 m.
- upper trace : Gas phase photoacoustic spectrum of o-xylene in the  $\Delta\nu_{\text{CH}} = 6$  overtone region. The PA spectrum was measured at  $T = 25 \text{ }^\circ\text{C}$ , a sample pressure of 29 Torr and with a 10 cm. cell pathlength.

17000 16800 16600 16400 16200 16000



12000 11800 11600 11400 11200 11000 10800

Wavenumbers

measurement of absorptivities that are less than  $10^{-6} \text{ cm}^{-1}$ . A schematic and pictorial representation of our version of a c.w. amplitude modulated photoacoustic spectrometer are shown in Figures 5.7 and 5.8.

**FIGURE 5.7**

Block diagram of the photoacoustic spectrometer.

# DYE LASER OUTPUT

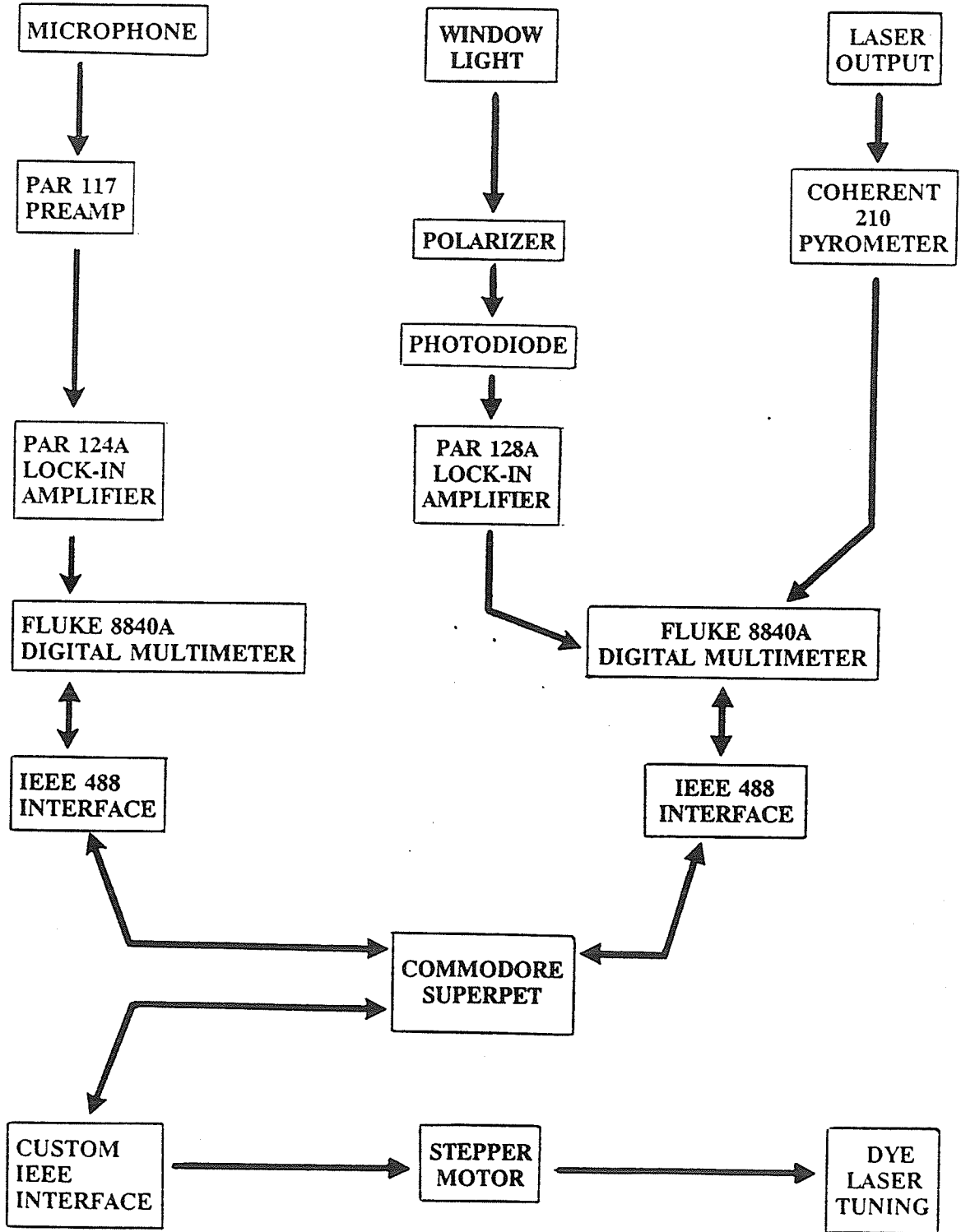
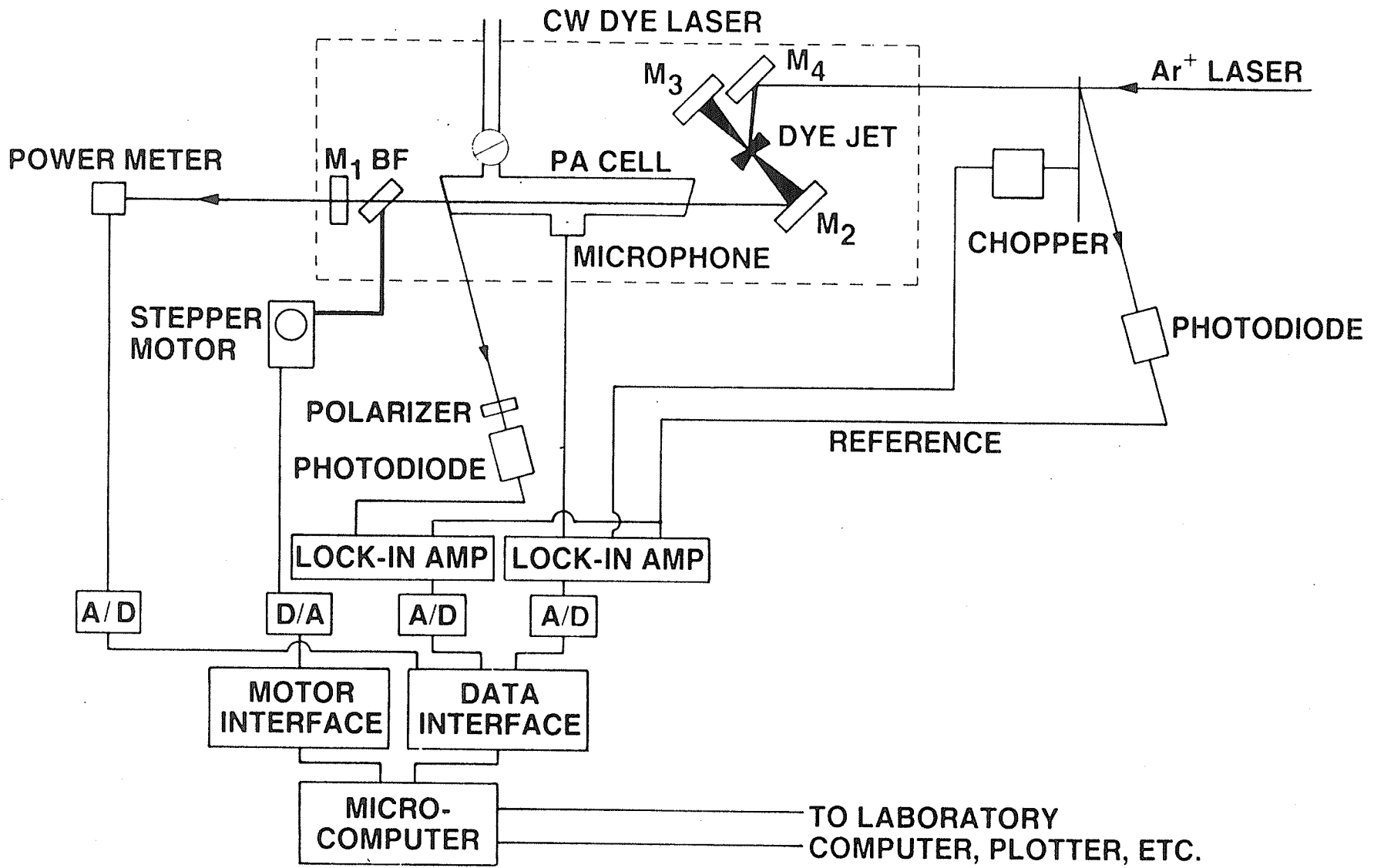


**FIGURE 5.8**

Schematic representation of the complete photoacoustic spectrometer.



## CHAPTER 6 : PA INSTRUMENT CONTROL AND DATA ACQUISITION

In the typical photoacoustic experiment modulation frequencies are low and lock-in integration times are long. A small, inexpensive microcomputer is completely adequate for instrument control and data collection. A Commodore SuperPET was used for these purposes. Despite the age of the PET, it is an attractive solution to the problem of low cost laboratory automation. The primary reason behind this is that it fully supports an IEEE-488 general purpose interface bus (GPIB)<sup>81,82</sup>. The PA experiment is interfaced to the PET through this interface. Some detailed knowledge of the IEEE-488 GPIB bus is required to understand the circuitry used in the interfacing.

### i.) Description of the GPIB-IEEE 488 Bus<sup>81,82</sup>

The hardware independent protocol and wide range of compatible laboratory instrumentation makes the IEEE-488 digital interface a flexible and standardized means of integrating computers and laboratory instrumentation. The interface bus offers excellent

noise impunity; an essential feature in most laboratory environments. Probably the most inviting feature of the interface is that a single bus can support a number of connected devices. Each device has an address on the bus. A GPIB device can operate in three modes; listener, talker, and controller. In the listening mode the device accepts data or secondary commands from the bus. Talkers send data or secondary commands over the bus. The controller assumes the primary supervisory role on the bus. It addresses and commands bus devices as well as manages bus traffic. In a typical GPIB transaction, the controller addresses as many listeners as required then grants the talker permission to use the bus. After the talker is finished, it relinquishes the bus back to the controller. At any one time, only one talker or controller can be active. In principle all connected devices can assume any combination of the three modes. The SuperPET however is permanently configured as the primary bus controller. All other devices are restricted to being talker-listeners.

The bus employs a byte-serial, bit-parallel, "low-true" logic scheme with TTL (transistor-transistor logic) level signals. The 16 bus lines can be grouped into three categories:

- 1 Eight bidirectional data lines (DIO 0-7) which carry a byte of address or command or data.
- 2 Five interface management lines:
  - a.) ATN (attention) line indicates whether information on the bus is data or a bus address-command.
  - b.) IFC (interface clear) line resets all devices to a defined state.
  - c.) REN (remote enable) disconnects instrument from the bus to permit stand-alone operation.
  - d.) SRQ (service request) permits a connected instrument to signal the controller that it needs attention.
  - e.) EOI (end or identify) when issued by the controller, requests the device which asserted a service request to identify itself by placing its address on the bus. When EOI is asserted by a talker it signifies the end of a message-transfer sequence by the talker. The controller then takes over the bus. This last type of EOI is optional and many instruments send the ASCII CR and LF characters to signify the end of a message.

The specifications of the IEEE-488 devices must be checked to see if they support an EOI end protocol.

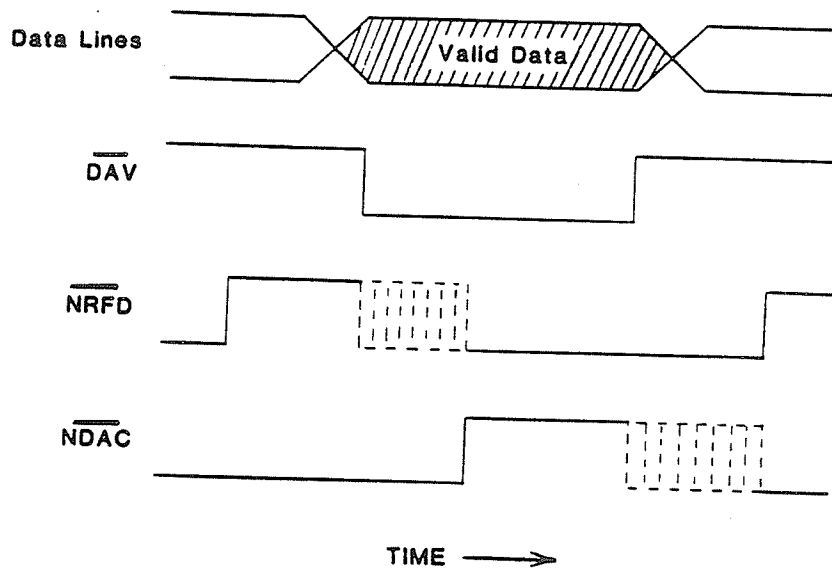
3 Three byte transfer handshake lines:

- a.) DAV (data valid) line indicates that the data on the bus is valid.
- b.) NRFD (not ready for data) line indicates that the connected devices are not ready to accept data.
- c.) NDAC (not data accept) line shows that the devices have not yet processed the data on the bus.

Every byte transfer whether it is a byte of address, or command, or data is accompanied by an asynchronous 3-wire handshake on the byte-transfer-control lines (see Figure 6.1). Any interface circuitry must conform to this handshake IEEE-488 protocol. An unaddressed handshake involves the talker or controller putting a byte of information on the bus and asserting the DAV line low (true). This announces that the byte on the DIO lines is valid. Acknowledging the DAV signal the fastest device pulls NRFD low, signifying it is busy processing the information. Once the processing is completed by the slowest device, NDAC (held low since the previous transfer) is

**FIGURE 6.1**

IEEE-488 Three wire handshake protocol.



released indicating that the byte has been accepted. Sensing the NDAC signal, the controller or talker removes the byte from the DIO lines and forces DAV high. Devices respond by pulling NDAC low and NRFD high, indicating they are ready for the next transfer.

A general bus transaction involves a transfer of one or more bytes of data between a specific talker and one or more addressed listeners. The general procedure is as follows:

A Address listeners : The controller asserts the ATN line low, places a valid listen address on the bus and initiates the byte-transfer-handshake by setting the DAV line low. Acknowledging the low ATN line, bus devices realize the DIO lines carry an address or a command. Connected devices complete the handshake. The device whose address matched that on the DIO lines is activated to the listening mode. If more listeners are required, the process is repeated with the appropriate device addresses.

B Address talker : The same process as in A is repeated

with the DIO lines carrying a valid talk address. Only a single talker can be activated.

C Transfer data : The addressed talker places a byte of data on the DIO lines and begins the handshake protocol by setting DAV low. Addressed listener(s) respond, accept the data, and complete the handshake. More data bytes can be transferred by simply repeating this procedure. Once all the data is transferred, the talker asserts the EOI line at which time the controller re-assumes bus control.

When designing circuitry for use with the bus, there are some features that one should be aware of. Devices generally terminate signal lines with  $3k\Omega$  pull-down resistors, which maintain uniform line impedance and high noise immunity. IEEE-488 drivers must sink 48 mA (receivers use Schmitt-type inputs). This imposes restrictions on cable lengths and the number of connected devices. The maximum recommended distance between two devices adjacent on the bus is 5 m. The maximum cable lengths between any two

communicating devices is 20 m. Longer lengths may cause timing violations in the IEEE-488 protocol. The number of connected devices is limited to 15 (including the controller). The major "hardware" factor in determining the data transfer rates is the setting time  $T_1$ . This is the time between when the data is put on the DIO lines and the DAV line is asserted true. When open-collector transceivers are used for connection, the standard  $T_1$  is 2  $\mu$ s. When tri-state transceivers are used, a higher transfer rate and hence a lower  $T_1$  are allowed. Some controller chips allow the setting time to be software controlled. One high speed software setting for the Intel 8291A controller allows a  $T_1 = 2 \mu$ s for the first byte after a change in the ATN state while for all subsequent bytes  $T_1 = 500$  ns. Thus when designing interface components one must determine which timing protocol is being used by the controller. Alternatively, with the right choice of components, the data transfer rates may be improved by a low level program command to the controller chip.

## ii.) GPIB-IEEE 488 Photoacoustic Configuration

The IEEE-488 interface bus can support up to 15 unique talker and listener addresses. The SuperPET controller requires two talker-listener addresses. These are designated as IEEE-488 channels 0 and 1. The Commodore model 8850 dual 512 K floppy disk drive is configured as channel 8 by default. The SuperPET can provide two-way control over 12 other talker-listener devices on its single IEEE-488 interface bus. In the simplest configuration, the photoacoustic experiment uses only 3 IEEE-488 devices aside from the controller and disk drive. Two devices are standard IEEE-488 instruments while the third has a custom designed IEEE-488 interface.

As discussed in the previous Chapter, two signals are recorded from the photoacoustic experiment; the acoustical signal itself and the dye laser output. In the experimental configuration, a EG&G Princeton Applied Research (P.A.R) Model 124A lock-in amplifier processes the acoustical waveform from the Knowles Electronics BT 1759 electret microphone. The dye laser output is monitored in one of two ways. In the first way, a photodiode monitors the scattered light from a brewster angle window. The photodiode signal is then

processed by a P.A.R. Model 128A lock-in. In the other method, the dye laser power is directly monitored by a pyrometer (Coherent Model 210). Both the processed acoustical and dye laser output signals are digitized by two Fluke 8840A digital multimeters. The meters are fully programmable,  $5\frac{1}{2}$  digit instruments equipped with standard IEEE-488 interfaces. They are configured as talker-listeners occupying channels 9 and 10. In this thesis, it will be assumed that channel 9 measures the photoacoustic signal while channel 10 monitors the dye laser output. The user can actually control which channel is to be used for monitoring which signal.

The Fluke multimeters can be programmed to operate in an autoranging or a fixed range mode. Since the signals from the experiment have limited ranges autoranging is avoided thus speeding up the signal digitization<sup>83</sup>. Typically the photoacoustic signal channel (channel 9) is set at the  $\pm 20$  VDC range while the dye laser output channel (channel 10) is set at the  $\pm 2$  VDC range. These ranges are compatible with the EG&G 124A and 128A lock-in amplifier output voltages. The Fluke meters have selectable digitization rates. With a 60 Hz line voltage, A/D conversion times for the slow, medium, and fast modes are 395, 45, and 7 ms respectively. In the

fast mode the meter only has  $4\frac{1}{2}$  digit precision. This corresponds to 1 mV resolution in the  $\pm 20$  VDC range. In the photoacoustic application this is usually sufficient resolution. If however the dye laser output is taken directly from the pyrometer, the fast conversion mode will yield a noisier dye gain curve. The fast mode doesn't support any signal processing. For cleaner background curves, the slower digitization rates which do filter the input signal can be used.

The meters have four programmable external triggering modes. The meters can be externally triggered by a remote TTL pulse or by a IEEE-488 bus trigger. In this experiment, the Flukes are bus triggered by the SuperPET data collection software. The two bus triggering modes, T2 and T4 respectively enabled and disabled the automatic settling time of the Fluke multimeters. In a controller initiated trigger the settling time delay (time between the trigger and the beginning of the A/D conversion) begins only after the trigger command has been processed. The automatic settling delays for a DC voltage reading in the 2 to 1000 volt ranges (not autoranging) are 342, 17 and 9 ms for the slow, medium and fast conversion rates. Disabling the settling time reduces the delay to 1

ms ( $\pm 150 \mu\text{s}$ ). Although not crucial in the PAS experiment, the through-put performance of the meters can be significantly improved by disabling the automatic settling times. Both T2 and T4 triggering modes were used in the experiments.

The above paragraphs deal with the data collection hardware. The instrument control aspect of the experiment consists of automating the wavelength tuning of the dye laser and coordinating it with the data collection sequence. The tuning element of the CR-599-01 dye laser is a micrometer driven three-plate birefringent filter. Turning the micrometer head tunes the laser. The simplest way to automate this process is to attach a stepper motor to the micrometer head and interface the motor to the experiment controller. In this experiment an Aerotech Inc. stepper motor and translator board were purchased from Optikon Corp. Ltd. for this purpose. The Fluke DMMs with IEEE-488 interface used for data collection required no special circuitry in order to be interfaced to the SuperPET. However the stepper motor required some custom interface circuitry.

The Aerotech 1401 translator board contains a fused 115/230 V power supply, circuitry to drive the stepper motor, as well as

digital logic circuitry which controls the motor. The board is designed to be part of a larger interface system and hence provides a remote input control connector (J2). Through this connector the SuperPET can control the operating mode of the stepper and the direction. The functions of the pins on the J2 connector are given in Table 6.1.

The Aerotech stepper motor has three operating modes. The slew mode continuously drives the rotor of the motor. Applying a "low-true" voltage on pin 5 of the J2 connector activates motor slewing. Stepping modes are controlled by pin 6. The full step mode is a standard 200 steps per revolution mode while the half step mode has twice the number of steps per revolution. A low signal on pin 6 selects the half step mode. The 1.8 and 0.9 degree per step resolution of the full and half step modes corresponds to approximately a 0.6 or a 0.3  $\text{cm}^{-1}$  wavenumber step of the birefringent filter. The filter's optical bandpass is 40 GHz ( $1.33 \text{ cm}^{-1}$ ) or better across 310 to 1080 nm. Since this is only slightly greater than wavenumber step of the motor, the motor is directly connected to the micrometer head without any gearing.

The stepping or slewing direction is under control of pin 11 on

**TABLE 6.1 :** Pin-Outs of the Remote I/O Connector (J2)  
for the Aerotech Stepper Motor Driver.

---

pin	designation
1	ONE / TWO PHASE ON
2	RESET
3,10,15	SPARE
4	STEP NC
5	SLEW
6	FULL / HALF STEP
7	RESET TO READOUT
8	CL TO READOUT
9	DIR TO READOUT
11	CW / CCW DIR
12	STEP NO
13	GND
14	+ V
16	LCL / REM

the J2 connector. Bringing pin 11 to a low voltage state selects a counter-clockwise scanning direction for the motor. Once the appropriate scan direction is chosen and the motor is in a stepping mode (pin 5 is false), the motor can be remotely stepped by applying opposite logic levels to pins 4 and 12 of the J2 connector and then toggling those levels. This sequence causes the motor to take a single step in the chosen direction and with the chosen resolution.

All that is required to automate the control of the stepper motor functions from the SuperPET is to route CMOS level logic signals to the appropriate pins of the J2 remote connector of the stepper motor systems. These signals could easily be derived from the parallel port of the computer. However, a peripheral device unrelated to the PAS experiment specifically required the PET's parallel port. Since the Fluke DMMs were controlled through the IEEE-488 interface, for consistency the same interface was chosen to attach the motor to the PET. This choice of a standard interface has the advantage of making the instrument control and data acquisition relatively machine independent. In addition, in principle any IEEE-488 based system can be directly attached to any GPIB controller with absolutely no change in hardware.

There are several commercially available single chip circuits designed for GPIB interface applications. Most of these chips support a wide range of IEEE-488 features and protocols. Unlike the Fluke DMMs, the stepper motor is strictly a "listen-only" device on the bus. Being able to configure the motor as a listen-only device simplifies the required interface circuitry. The circuitry needs only to perform three functions: 1) respond to the IEEE-488 bus handshaking protocol; 2) determine when address information is on the bus and recognize its address; 3) once addressed, read the data on the bus and pass it to the appropriate pins of the J2 connector of the remote stepper motor controller board. The necessary interfacing can be accomplished with a few common integrated circuits<sup>84</sup>.

The IEEE-488 handshaking protocol was described in section i of this Chapter. The responder section of the motor interface simply performs the bus handshaking for an ATN command sequence. When the controller issues a bus command, the ATN line is brought low (true). A low DAV line signifies that the command or address information on the DIO lines is valid. At this point of the ATN command sequence, all attached devices respond by driving NRFD and

NDAC lines to their proper states to complete the handshake (see Figure 6.1). With a simple set of Hex inverters (74LS368), the required device response logic can be achieved. The responder circuit and logic are diagrammed in the insert of Figure 6.2.

Each bus device must have a unique address. Most commercial IEEE-488 compatible instruments have a DIP switch selectable bus address. This feature adds considerable overhead to the circuitry for the interface. Rather than support a selectable addressing feature, the motor address was hardwired into the address decoding logic. The motor address can be changed by changing the input sequence of the DIO lines in the address decoding circuitry.

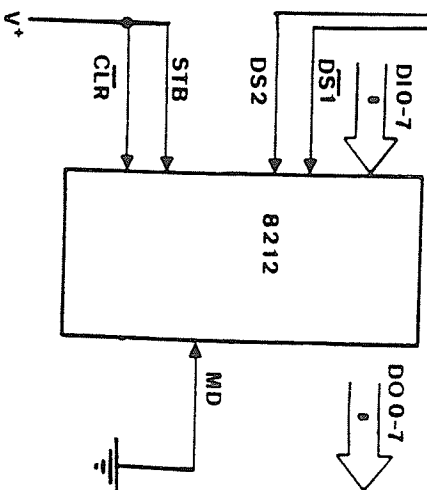
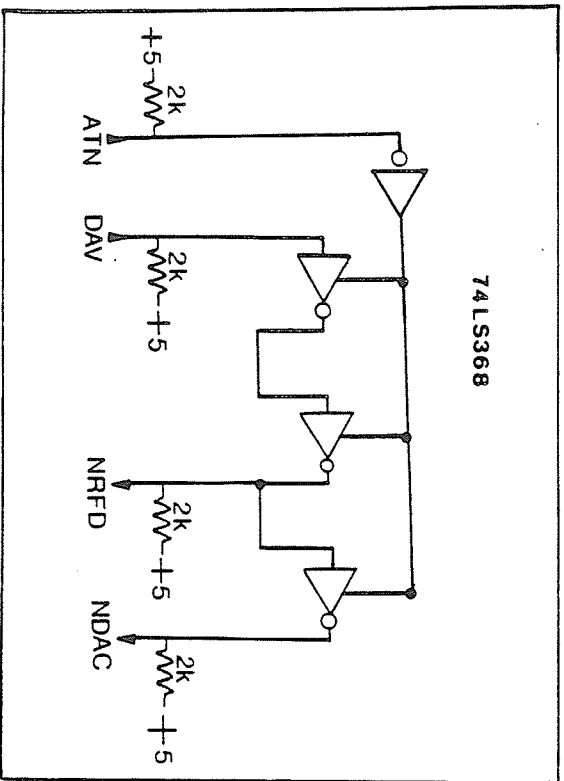
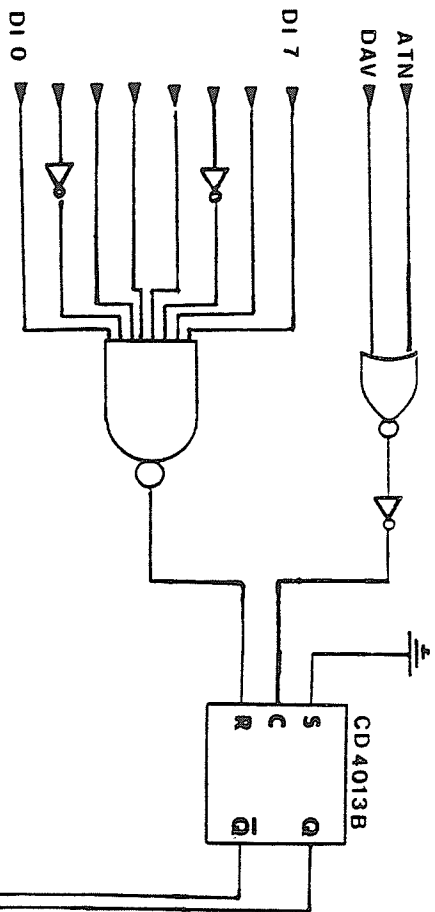
Address decoding is carried out by an 8-input NAND gate and a few inverters connected to the gate inputs (see Figure 6.2). When the controller sets the ATN and DAV lines low, devices on the GPIB bus should interpret the data on the DIO lines as a command or address. The ASCII decimal codes 32 through 62 and 64 through 94 are reserved for GPIB addresses. When these codes are put on the DIO lines by the controller during an ATN command sequence, the device with the particular listen/talk address code is being activated. In this application, the stepper motor interface is given

**FIGURE 6.2**

Block diagram of the stepper motor IEEE-488 interface circuitry.

Main diagram : address decoding and data latching components.

Insert diagram : three-wire handshake responder logic.



the listen address 27. This corresponds to an ASCII decimal code of 59 or the "/" character. In 7-bit binary, decimal 59 corresponds to 0111011. Only bits 3 and 7 are low. Placing inverters on these DIO lines will cause the NAND gate (CD 4068B) output to go high each time decimal 59 appears on the DIO lines. To determine if this is indeed an address code, the output of the NAND gate is connected to the input of a D-type flip-flop. The output of the flip-flop is clocked by the inverted NOR of the ATN and DAV signals. Recall, during a command sequence, the ATN and DAV lines are simultaneously low while the command is being processed by the bus devices. The NOR gate output goes high at this stage of the handshake. Once the devices complete the handshake, the DAV is brought high causing the NOR output to go low. The positive going clock pulse of the inverted NOR output triggers the flip-flop and the input (D) is transferred to the output (Q). The flip-flop output remains in this state until reset by the next ATN command sequence. The address decoding Q and  $\bar{Q}$  outputs of the flip-flop are used in the triggering of the bus data reading circuitry.

The final interface function is to latch the data on the DIO lines once the motor has been addressed. An Intel 8212 8-bit

input/output port is used for the data latching. The DIO lines are connected to the inputs of the 8212 while the 8212 outputs are directed to the pins of the J2 remote connector (see Figure 6.3). The 8212 acts as eight flip-flops whose outputs are controlled by four logic levels. When clocked by the appropriate logic sequence, the levels present at the inputs are passed on to the outputs. In this application, the 8212 is used as a simple gated buffer. In the gated buffer mode, the mode (MD) and strobe (STB) control logic inputs are tied low and high respectively. The gate is only controlled by the device selection logic inputs (DS1 and DS2). When DS1 is low and DS2 is high, the gate is enabled. The levels on the DIO lines are then passed on to the J2 connector. The Q and  $\bar{Q}$  outputs of the address decoding flip-flop act as the device selection logic levels. Address decoding and data latching logic is presented in Figure 6.2 while the complete interface wiring diagram for the stepper motor interface is given in Figures 6.3 and 6.4.

The Aerotech translator board along with most of the circuitry used in the interface use CMOS logic. The IEEE-488 bus uses TTL logic. The IEEE-488 outputs are terminated with 2 to 3 K $\Omega$  pull-up resistors. CMOS interface outputs are passed through a HEX

buffer/driver (open collector 7417) whose outputs drive the IEEE-488 TTL loads.

**FIGURE 6.3**

Upper wiring diagram of the IEEE-488 Stepper Motor Interface Board.

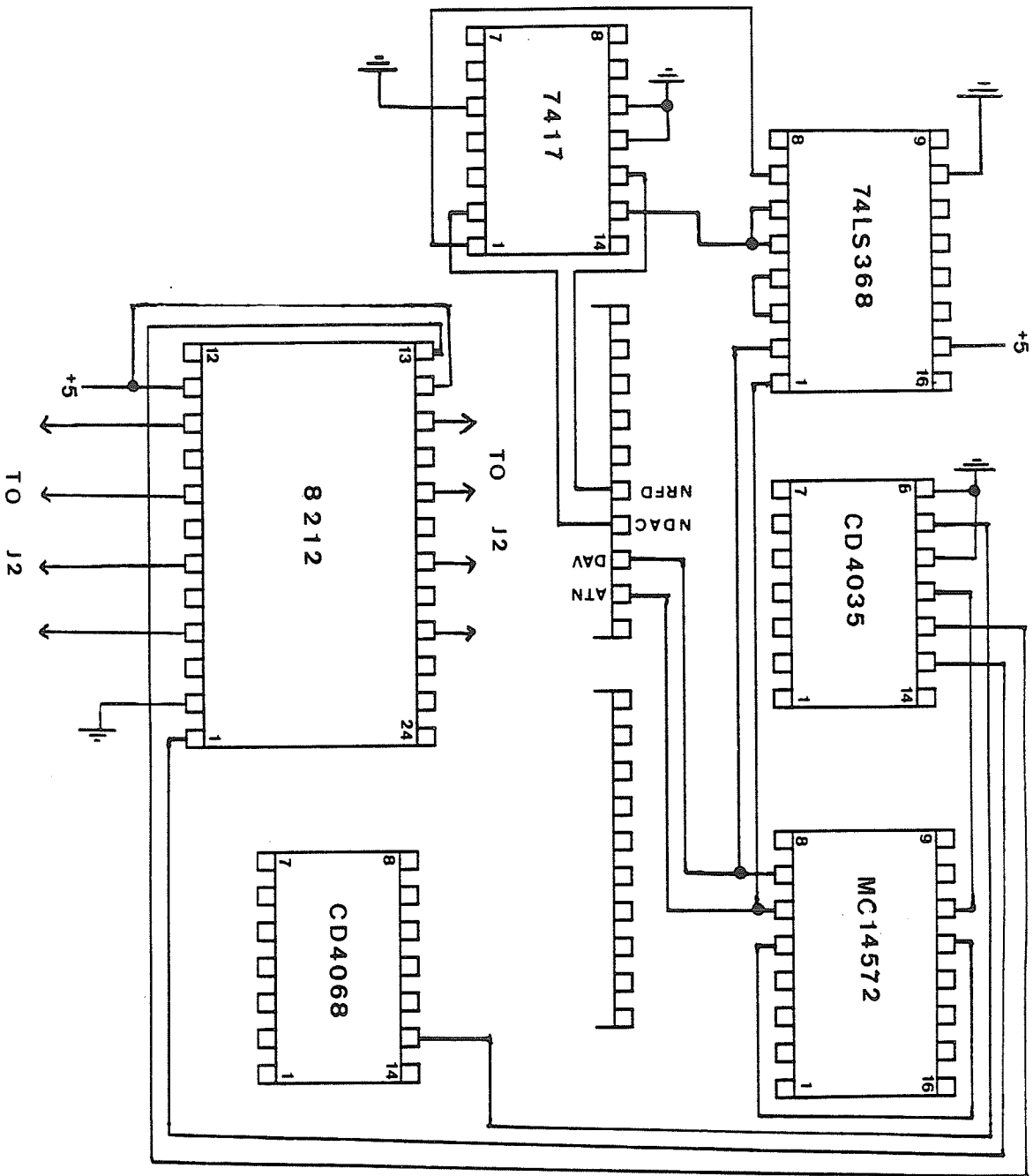
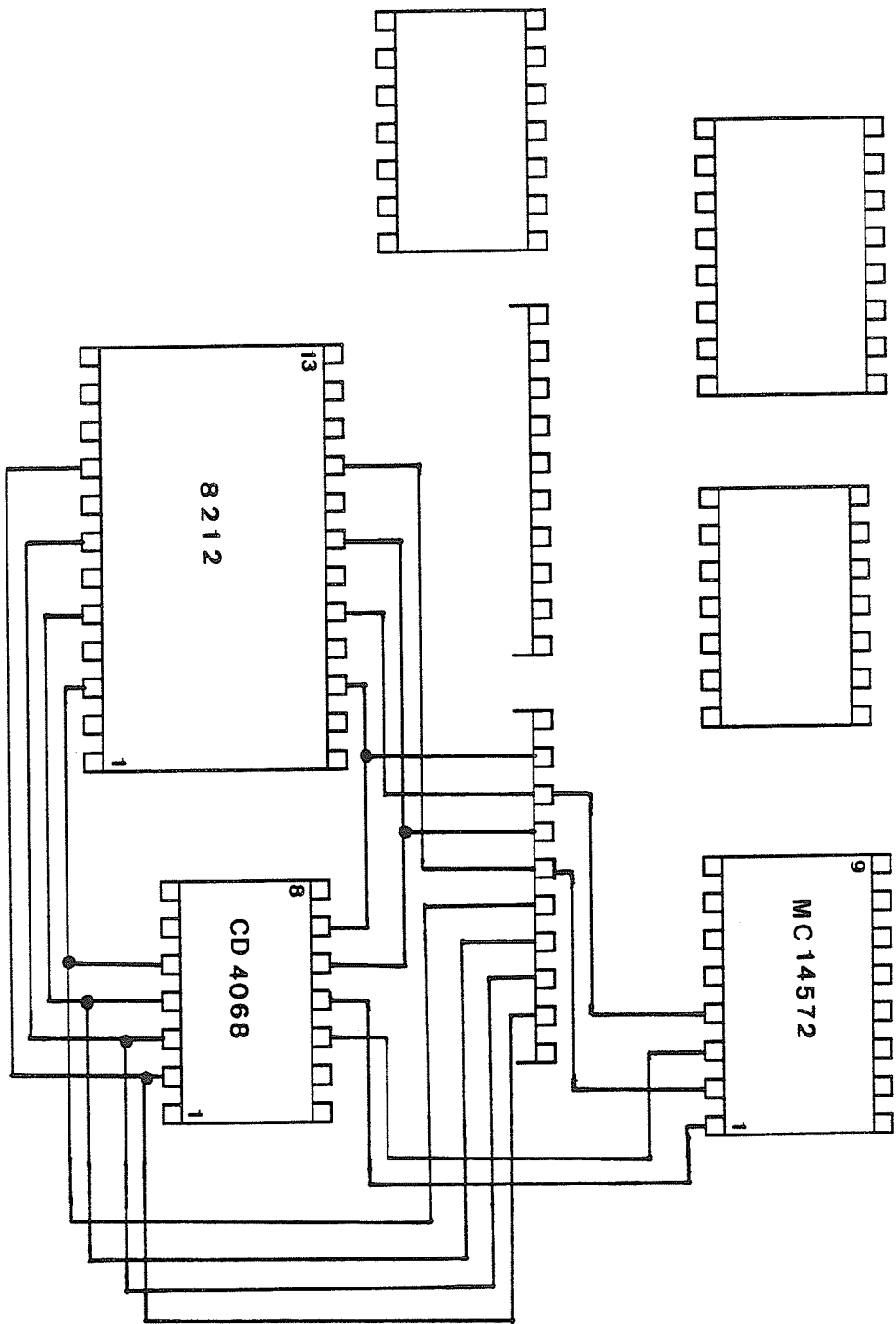


**FIGURE 6.4**

Lower wiring diagram of the IEEE-488 Stepper Motor Interface Board.



### iii.) PAS Control-Acquisition Software

The Fluke DMMs and the Aerotech stepper motor are under the program control of the SuperPET through its IEEE-488 bus. The aim behind the control-acquisition software is to completely automate the process of collecting photoacoustic spectra. The requirements of the automated spectrometer are modest. In the cw PAS experiment, the acoustical signal is monitored over rather long lock-in time constants (10 ms - 1 s). These long integration times are usually the limiting time factor in the data collection sequence. The speed advantages gained by writing the automation software in assembler would be largely eroded by the long settling time delays required by the lock-ins. This somewhat justifies writing the control-acquisition software in a high level, more convenient language. The fastest executing language and the language with the greatest graphics support was the ROM based Commodore Version 4.0 BASIC. The PA control-acquisition program, PAS, was written in this language (see Appendix 1).

The PA control and data acquisition program is written in three distinct sections: motor control, PA scan setup, PA scan

acquisition. The first section gives the user direct control over the stepper motor. Like all sections, this section is menu driven. It is hoped that the menus are self explanatory. They will however be briefly explained in the following text.

Lines 5000-5800 of the program PAS contains the motor setup routine. The routine allows the user to step or slew the stepper motor in a clock-wise or counter clock-wise direction. Although the appropriately addressed, Commodore SuperPET BASIC, READ and WRITE commands can access the GPIB bus, the stepper motor interface is controlled by a series of BASIC POKE commands. The various interface lines as well as the timing of the GPIB bus can be directly controlled by POKE commands. The command sequence for the GPIB stepper motor interface is simply,

```
POKE 59456,0      : set ATN low
POKE 59426,219   : put motor address on DIO lines
POKE 59427,52    : set DAV low
POKE 59427,60    : set DAV high
POKE 59456,4     : set ATN high
POKE 59426,255   : clear DIO lines
POKE 59427,52    : set DAV low again.
```

Issuing this series of commands addresses the stepper motor as a listen-only device. The addressing sequence has the familiar structure discussed in the previous sections. The ATN line is set low which indicates a bus address/command will be placed on the DIO lines. Writing decimal 219 to the bus data lines (DIO0-DIO7) sets DIO2 and DIO5 lines low. This corresponds to the motor interface address. Setting DAV low, triggers the interface responder-decoder circuitry. Resetting the ATN and DAV lines completes the bus addressing procedure. The eight DIO lines are cleared and the DAV line is set low indicating the presence of valid data on the DIO lines. The DAV line triggers the latching circuitry and the levels on the DIO lines are passed to the J2 connector of the stepper motor control board. With the appropriate values on the DIO lines, the motor can be controlled. The connection between the GPIB DIO lines and the J2 connector were discussed in the previous section. The various motor functions controlled by the PAS program include, clock-wise slew (POKE 59426,16), counter clock-wise slew (POKE 59426,1), clock-wise step (POKE 59426,57 POKE 59426,58), and counter clock-wise step (POKE 59426,41 POKE 59426,42).

Recall, in order to step the motor the DIO0 line must be toggled high-low. A sequence is completed by clearing the DIO lines and resetting the DAV line high.

Controlling the stepper motor interface through the series of POKE commands slows the GPIB command/control sequence sufficiently for the interface and motor circuitry to respond. Timing problems can be encountered if the BASIC WRITE command is used to access the motor interface. Maintaining the strict IEEE-488 command protocol ensures that the other instrumentation on the bus is unaffected. The slower timing of the stepper motor interface may slightly increase the bus addressing time sequence thus slightly decreasing the effective bus through-put . For the modest data transfer rates and the minimal general bus traffic encountered in a PA data collection sequence, a small decrease in bus performance is not critical.

The next section of the instrument control and data acquisition program, the PA scan setup section (lines 500-2800), prepares the GPIB devices and controller for a PA scan. If a scan has not been previously setup during the session, the user is required to supply a number of data collection parameters. The first setup screen asks

the user to input the laser dye being used for the experiment. Given a dye, the program determines the birefringent filter angle limits of the dye and the rough wavelength calibration of the filter in those limits. The wavelength calibration is obtained from a low order polynomial fit of a calibration list of filter angle - wavelength pairs. The reported wavelengths are meant to serve as a guide to the user. They were not intended to be an absolute calibration of the PA spectra. Wavelength calibration is discussed in detail in sections ii and iii of Chapter 7.

The second menu screen involves the setup of the stepper motor for the scan. The user is prompted for the scan direction, stepsize, and number of steps per data point. The default motor parameters are: clock-wise scan direction, half-step mode, and a data point collected at each motor step.

The next setup menu requires the initial and final birefringent filter settings for the scan to be entered. If the input filter angles are consistent with the range of the particular dye and the chosen scan direction, the approximate wavelength range of the scan is displayed. From the input stepsize and filter angle range, the number of motor steps and the number data points to be collected are

These newly calculated variables control the data collection loop.

The fourth menu sets up the Fluke DMMs. The user is asked to input the voltage range, A/D conversion time, and to assign the channels for the PA signal and the normalizing signal. The model 124A lock-in amplifier generally processes the PA signal while the model 128A lock-in or pyrometer processes the normalizing signal. By default channel ten is assigned as the PA signal channel with a voltage range of  $\pm 20$  VDC in the fast conversion mode. Channel nine is assigned as the normalizing signal and is set at  $\pm 2$  VDC in the medium conversion mode. To remotely program these parameters the proper device dependent command strings must be passed to the instruments. The Fluke programming language is documented in the Fluke 8840A Instruction Manual. The default command strings are "R3 S2 T4" and "R2 S1 T4" where Rx,Sx,Tx, respectively, control the voltage range, A/D conversion speed, and the triggering of the meters. A set of signal multipliers for the meters are also generated at this stage. The signal multipliers are determined based on the voltage range of the meters. These multipliers are chosen such that when multiplied by the meter readings, they give real numbers which can conveniently be truncated to integer values. All

the information pertaining to the PA experiment is stored in integer form to be consistent with the FTIR and Beckman data sets.

The next experimental variable which is asked for is the longest lock-in time constant being used in the experiment. The time constant determines the timing of the data collection loop and the maximum settling time required by the lock-in amplifiers.

The final setup menu asks if the PA and normalizing signals should be stored as disk files. If the files are to be stored on disk the user is prompted for a filename without an extension. The program automatically uses the extensions "SPE" and "BKG" for the PA and normalizing signals respectively.

Once the data collection parameters are specified, a PA scan can be initiated. The program assumes that the user has attached the stepper motor to the birefringent filter and that the filter angle was preset to the initial angle specified in the setup menu.

The heart of data collection subroutine (lines 3000-4000) is a simple FOR loop over the number of data points to be collected during the scan. Prior to initiating this data collection loop, the required GPIB devices must be activated and set to the proper state. The first devices activated are the Fluke DMMs. The GPIB channels 9 and 10

which correspond to the multimeters are opened as files 2 and 3 respectively. The appropriate command strings are passed to the DMMs by writing to these files using the BASIC PRINT# command. This activates the DMMs to the states defined in the setup routine. If the scan is to be stored, the disk files are opened in a similar manner. Files 4 and 5 are opened as the PA and normalizing data files respectively. A control block is written to the disk files prior to the data collection loop. The control block simply consists of the initial birefringent filter angle, the scan direction flag, motor step-size indicator, the number of steps per data point collected, and the number of data points for the scan. The control block as well as the DMM readings are converted and stored as integers. This is done in order for the PA experimental files to have the same data TYPE as FTIR/Beckman data files. To convert the initial filter angle to an integer value, it is multiplied by 1000 and truncated. The DMM readings are treated similarly. The constant multiplier however is determined by the DMM range specified in the setup procedure. After the control block is written to the disk files, the data collection loop is entered. The first part of the loop triggers and reads the outputs of the DMMs. The readings are stored and the stepper motor

is stepped the appropriate number of steps for the next data point. The time is read and a delay loop is entered. In the delay loop, the keyboard is polled for the scan abort command and the time is read again. If the elapsed time between the two time readings exceeds the settling time for the lock-in time constant the delay loop is terminated and the data collection loop is rejoined. Otherwise, the delay loop is executed until the settling time is exceeded. Once the collection loop is finished or has been aborted, the opened files are closed and the subroutine exited. The user is returned to the main command menu where another scan can be initiated, the scan parameters re-set, the stepper motor repositioned, or the program exited. The complete program listing is given in Appendix 1.

## CHAPTER 7 : PHOTOACOUSTIC DATA ANALYSIS SOFTWARE

The previous Chapter concerned itself with both the hardware and software aspects of PA data collection. This Chapter outlines the programs that were written to process the raw PA data. The data analysis and processing software need to fulfill a number of functions. The most important single function is probably the wavelength (wavenumber) calibration of the data. In the PA experiments, the microphone voltage is collected as a function of dye laser, birefringent filter angle. For the data to be useful as absorption spectra, the acoustical signal must be known as a function of wavelength. The automation of the wavelength calibration procedure is reported in section ii of this Chapter.

In Chapter 4 the procedure for collecting the CH stretching spectra in the fundamental and lower overtone regions was reviewed. The spectra are collected with conventional, commercial instrumentation which is interfaced to the Nicolet 1280 data station. The powerful, commercial FTIR software package supplied by Nicolet can be used to process these spectra. One goal of the PA experimental design was to integrate the PA data with the data from

the Nicolet FTIR and Beckman absorption spectrometers. The main impetus behind this goal was to give the PA data files access to the extensive set of Nicolet spectral processing routines. The first step towards this goal requires the transfer of PA data files to the Nicolet 1280 data station. The data transfer software and some simple data manipulation routines form part of the photoacoustic analysis software package for the Nicolet.

The Nicolet program PAS contains the data transfer routines as well as various miscellaneous data processing routines. Graphical presentation of the data helped in the wavelength calibration and provided a means to check on the integrity of the data transfer procedure. Routines to add, subtract, and ratio PA data files proved to be useful as well. Spectral ratioing was particularly important for the normalization of the PA spectra. Although the Nicolet FTIR software has a number of ratioing procedures, normalizing the spectra at an earlier stage reduces the number of PA files having to be converted to the FTIR36/Beckman file structure. The next section provides some detail on the Nicolet PAS program and the transfer procedure in general.

i.) Data Transfer & Rudimentary Processing in the Filter Angle Domain.

Although the SuperPET is completely adequate for controlling the PA spectrometer and acquiring the PA data, it lacks the computational power to do any substantial data processing. This reason, along with the desire to integrate the PA data with the FTIR - Beckman data, requires transferring PA spectral data to the Nicolet 1280 data station. Two methods are currently in place to accomplish this task.

The Nicolet 1280 has some highly specialized, resident data i/o packages. They are essentially designed to connect the 1280 computer to other Nicolet instrumentation. Their highly specialized nature and the lack of information on their i/o protocol required the programming of a data transfer procedure from the SuperPET to the Nicolet. The most logical way to accomplish this is through the serial transmission of the data via the RS-232 serial interface. Both the SuperPET and Nicolet 1280 provide some support for this standard interface. The only tolerable, high level programming

environment for the Nicolet was the Nicolet FORTRAN compiler. FORTRAN callable graphics and plotting libraries are available to assist programming development. Unfortunately, the available FORTRAN i/o libraries do not allow control over the RS-232 channel parameters nor do they support input through the RS-232 ports. The first method of data transfer emerged from a set of programs written to understand and debug the Nicolet end of the data transfer procedure. A simple Waterloo BASIC program for the SuperPET and a crude FORTRAN-assembly language program for the Nicolet both named PASFER (PhotoAcouStic transFER) make-up this first method. Although this method is functional, its routine use is not recommended. SuperPET Waterloo BASIC provides the programmer with direct and very simple control over the RS-232 port and serial traffic but it is exceptionally slow. Data transfer rates are limited to 300 bits per second (b.p.s.). At 300 b.p.s. and with the additional software handshaking overhead, a typical PA data file can take 30 minutes to transfer. On the basis of the information gained from the PASFER programs, a second method which supports faster transfer rates was developed.

The SuperPET side of the second method utilizes some of the

fundamental data communication capabilities built into the Waterloo 6809 editor. The SETUP editor command displays the RS-232 port parameters. Only two parameters need to be considered, baud rate and parity. The default even parity setting should be changed to none/mark. The baud rate for the RS-232 port depends on the distance between the Nicolet and SuperPET. For short cable lengths and low noise conditions, transfers at 9600 baud are possible. In general, transfers at 4800 baud are usually successful. Having setup the SuperPET's RS-232 port, the data file is loaded into the editor with the "g" or "get" command followed by the appropriate filename. Once loaded into the editor, the "p serial" command initiates the transmission of data through the RS-232 port. Before initiating the RS-232 transfer, the data reception part of the Nicolet program must be setup. The Nicolet data reception routine is part of a larger photoacoustic data analysis program called PAS. In addition to being able to capture PA data on the Nicolet RS-232 port B, the program can retrieve and store spectral files from the Nicolet hard disk, display and plot spectral data, ratio, add, and subtract spectral data. The complete program listing is given in Appendix 2.

Upon running the PAS program, the user enters the command

menu. Program functions which have similar counterparts in the Nicolet FTIR36/beckma programs were given the corresponding three-letter FTIR36 command name. The data reception process is invoked by the non-FTIR command GRx (x=S,B). The GRx command calls three PAS subroutines, RECEIV, SETRATE, and RS232B which retrieves a data file from RS-232 port B. The assembly language SETRATE routine controls the baud rate for the RS-232 ports. The default values are displayed and the user is prompted if a change in baud rate is desired. The baud rates of the RS-232 interfaces of both computers must be the same. Having set the appropriate baud rate for the Nicolet RS-232 ports, the transfer sequence can be initiated from the SuperPET with the "p serial" editor command. The RECEIV routine reads in the integer data control blocks and the integer spectral data. The assembly language routine RS232B actually polls the RS-232 port for a valid integer and passes it to RECEIV. Note RECEIV was written to distinguish between SuperPET PA data files and FTIR/Beckman files. Both types of spectral files can be read into the PAS program through the RS-232 port B. The same flexibility was built into the other general photoacoustic data analysis i/o routines. Upon completion of the transfer, the user is

returned to the command mode. A typical transfer takes between one and two minutes.

General i/o routines can be invoked from the command mode by the FTIR command names GDx, PSx, and PDx (x=S,B). These routines allow for the storage and retrieval of spectral data files from the D0 plater of the Nicolet hard disk drive. Again either raw PA data files or FTIR/Beckman files can be used with these routines. In the FTIR36 and Beckma programs, the PSx and PDx commands store the spectral data in a compressed or full storage mode respectively. In PAS and the other photoacoustic analysis programs however, only the compressed storage mode is supported. The disk space savings gained from the compressed storage mode are quite dramatic. This option is therefore also recommended when using FTIR36/Beckma programs. The data file i/o routines GETSPE and PUTSPE are listed in the section on general photoacoustic data analysis routines of Appendix 2.

Graphics display of the spectral data provided a convenient means of checking the integrity of the data transfer process. The data transfer routines do not support any sophisticated error checking procedures. Data corruption can often occur without

noticeably affecting the transfer routine. The FTIR36/Beckma command name DSx (x=S,B) displays the sample or background spectrum, respectively. The command, PLx (x=S,B), plots the corresponding spectra on the Nicolet Zeta plotter. A number of library graphics routines along with the buffering and driving routines INBUF, DSPEC, PLAXS, and PLSPEC display and plot the spectra. The graphical presentation of the data is controlled in a manner similar to the method used in the FTIR36 software. The PAG, AXS, and TIT commands control the paging, axis drawing, and title for the plotting. The x and y plotter scale lengths are controlled by the XSL and YSL commands. The display and plotting windows are controlled by the FXF, LXF, FYA, and LYA commands. Scales are restored by the ASx (x=S,B) command. A user familiar with the FTIR/Beckma software should have no difficulty with these PAS program commands. If further information on the function of the commands is required, the user is advised to consult the Nicolet FTIR36 program documentation or the program listings of Appendix 2.

The PA data collection program collects both the acoustical signal and a signal proportional to the dye laser power. Since the PA

effect is proportional to the intracavity power, the final normalized PA spectrum requires that the microphone signal be ratioed against the laser power. The PAS program can carry out the PA data normalization. Typically a SuperPET PA data file is transferred to the Nicolet as a sample file using the PAS program command GRS. A SuperPET laser power file is transferred as a background file with the GRB command. The RAS command can then be used to ratio the sample versus background files. Alternatively the ADD command can add or subtract sample and background. Both the addition or ratioing of the files are controlled through the FCx (x=S,B) scale factors (these scale factors function equivalently as the FTIR scale factors of the same name). Prior to the adding or ratioing of the files, the data is multiplied by a scaling factor. Often an appropriate set of scale factors must be chosen to yield nicely normalized PA spectra. The ratioed spectrum is displayed and the user is prompted if the procedure is to be aborted. If not, the ratioed result replaces the resident sample file. Typically the normalized PA spectrum is stored with the PSS (or PDS) command. The stored spectrum is now ready to undergo wavenumber calibration and conversion to the FTIR/Beckma data file format. Again further information on the

ratioing commands can be obtained from the Nicolet FTIR36 manual or the source listings of Appendix 2.

## ii.) Wavelength Calibration Procedures

During the PA data collection sequence, the filter angle of the dye laser is incremented in small steps. At each increment of the filter angle, both the PA signal and laser power are recorded. To be useful as an absorption spectrum, the PA signal must be known as a function of wavelength. In principle this can be accomplished if the wavelength calibration of the filter angle at the various orders of the birefringent filter are known. The wavelength calibration curves for the birefringent filter used in the dye laser were reported in Figure 5.2. The simplest way to calibrate the birefringent filter is to monitor the dye laser output with a monochromator as a function of filter angle. Typically a set of filter angles are chosen which have a convenient interval and which span the gain region of the dye. It remains to determine the wavelengths of the filter angles within the intervals. This can be done using a fitting procedure or the values can be interpolated from the calibration list.

Fitting procedures essentially assume a functional form for the calibration curve. The most dramatic example would be finding the best straight line fit through a set of calibration points. There is however no reason to assume that the calibration will be linear. A

very high correlation between the predicted and the calibration points is needed for the linear model to be useful for calibration. The predicted and determined wavenumber values for each point used in the calibration should not differ by more than one part in ten thousand. Linear models were incapable of giving such high precision wavelength calibration.

Low order polynomial fitting also suffers from the same flaws as linear fitting although less severely. An overall functional form of the calibration is assumed, and not all the calibrating points are exactly fit by the model. Despite these shortcomings, a low order polynomial fit can be useful as a preliminary wavelength calibration. The method is computationally simple to implement and undemanding. Polynomial fitting routines are available in most commercial statistical software packages<sup>85a</sup>. Quadratic polynomial fits to lists of birefringent filter calibration points for a number of dyes were carried out using the SAS polynomial fitting package<sup>85b</sup>. The polynomial coefficients were then used in the SuperPET data acquisition program to provide a rough estimate of the wavelength range of the scan in the photoacoustic data acquisition program. They are intended as a guide to the user. These polynomial fits

however are not recommended for the final calibration of the PA spectra.

With a higher order polynomial, the problem one encounters with the other fitting procedures can be overcome. A set of  $n$  calibration points can be exactly fit by a polynomial of degree  $n-1$ . The problem with higher order polynomial fits however is their highly oscillatory nature. The polynomial may fit the  $n$  calibration points but between the points the predicted calibration curve can oscillate wildly. In most applications, between the calibration points the calibration is expected to be described by a smooth function not an oscillatory one. Thus high order polynomial fits may not be suited to wavelength calibration procedures.

Interpolation procedures overcome many of the problems associated with the global fitting routines. Interpolation methods are much better suited to the wavelength calibration problem. The simplest form of the procedure is linear interpolation. Given  $n$  calibration points (knots), they are connected by  $n-1$  straight lines. Linear interpolation does not suffer from the oscillatory problems encountered in polynomial fitting procedures. Given a sufficiently fine calibration grid, linear interpolation can follow the calibration

curve. The disadvantage of linear interpolation is the discontinuous nature of the interpolating function. At each knot (point where two lines meet) there is a discontinuity (an abrupt change in slope). Over the majority of the dye gain region, the dye laser tunes smoothly. A continuous global interpolating function might be considered more realistic. In most applications this is indeed the case. To obtain a smooth function with a continuously turning tangent the pieces of the function which meet at the knot must have the same first and second derivative at the knot. The lowest order piecewise interpolating function which can satisfy these criteria are cubic polynomials. Experience has shown that for most smooth functions, cubics provide adequately accurate interpolation. The method is known as piecewise cubic spline interpolation<sup>86</sup>.

From a computational standpoint, interpolation procedures are more complex to program and require greater resources than linear and polynomial fitting routines. For the size of the data structures involved in the PA experiment, the additional demands of an interpolating procedure are easily accommodated within what today would be called modest micro/minicomputer technology.

Wavenumber calibration routines using cubic spline interpolation are

implemented on the Nicolet 1280 minicomputer. Algorithms for piecewise cubic spline interpolation procedures are widely available<sup>87</sup>. If a spline function  $s(x)$  is piecewise cubic over an interval  $[x_0, x_n]$ , then  $q_k''(x)$  is linear and interpolates  $(x_k, s''(x_k))$  and  $(x_{k+1}, s''(x_{k+1}))$  on the interval  $[x_k, x_{k+1}]$ . Integrating the analytical expressions for  $q_k''(x)$  twice with respect to  $x$  yields expressions for  $q_k(x)$  in terms of second derivatives of the spline function over the various pieces of the interval. This yields a set of  $n-1$  linear equations in  $n+1$  unknown  $s''(x_k)$  variables. Essentially, spline algorithms involve solving the set of linear equations using specific values for the second derivatives of the spline function at the endpoints  $(x_0, x_n)$ . One common endpoint strategy sets the endpoint second derivatives to zero. These piecewise cubic splines are known as natural cubic splines. The SPLFIT subroutine, discussed in the next section, calculates the natural cubic spline coefficients for a list of calibrating points. The subroutine is listed in Appendix 2. The computational demands of a cubic spline interpolating routine on the SuperPET are too excessive. As mentioned in a preceding paragraph, a quartic polynomial fit is used as a rough wavelength calibration on the SuperPET. The next section includes a detailed

discussion of a Nicolet wavenumber calibration routine.

This section has so far concentrated on the requirements of the wavelength calibration software and the algorithms actually implemented in that software. In the remainder of this section, problems encountered in physically calibrating the dye laser birefringent filter and the photoacoustic spectra will be discussed. The initial calibration procedure involved determining the wavelength of the dye laser output at various birefringent filter angles with a monochromator. If the initial birefringent filter angle is carefully set at the outset of a scan and the filter angle is consistently stepped, then the original calibration list will provide an adequate calibration of the PA spectrum. If the filter angle is not properly set or the micrometer head of the filter slips in the motor housing during a scan, the calibration list may not provide an accurate calibration. To ensure against such calibration errors, a calibrating signal can be recorded during a PA scan. Often interferometer fringes or calibrating lines from a rare gas hollow cathode lamp are used in dye laser wavelength calibration. Neither of these options are currently available in our laboratory. There is however a simple way to internally calibrate the PA spectra. The

high energy rotational-vibrational transitions of water are extremely rich throughout most XH-stretching regions. Unlike the overtone transitions in larger molecules, the water transitions are extremely sharp and well resolved. They have also been extensively cataloged<sup>88,89,90</sup>. All these qualities makes them ideally suited as an internal calibrant for the XH stretch regions of the photoacoustic spectra. The traces of water present in the sample or the PA cell are often sufficient to provide the necessary calibration lines for the spectra.

### iii.) PA Data Calibration and BECKMA Conversion Routines

The wavenumber calibration process and the data conversion to the FTIR format are combined in the program PASCON, written in Nicolet Version 4.1 FORTRAN 77. The PASCON program commands, like those of PAS, were kept as close as possible to existing FTIR and Beckman spectral processing programs. The calibration and conversion routines however have no counterpart in the other spectral processing programs. The function of these PASCON routines are the subject of this section.

The wavelength calibration routines are an attempt at automating the procedure described in the preceding section. The process is not completely automatic. This is especially true if care was not taken during the setting of the initial birefringent filter angle or micrometer slippage occurred. As discussed in section ii, an accurate wavenumber scale may require using water transitions as an internal standard. As a first step in the calibration of the PA data, the spectral data can be plotted as a function of filter angle with the PAS program. Filter angles of assigned water transitions can be used in a calibration list or to update an existing list. A wavenumber calibration list consists of a set of filter angle -

wavenumber pairs. Routines were added to PASCON to create a calibration list, edit the calibration list, store the list to a named disk file, and retrieve an existing calibration disk file from the D0 platter of the Nicolet hard disk.

In the PASCON program, the calibration process is initiated by the CAL command. The user is prompted if a new calibration file is to be entered or an existing file retrieved. If a new file is to be entered, the GETXY routine is called. This routine simply prompts the user for the number of calibration points, followed by the filter angle - wavenumber pairs. The program can support up to fifty calibration points. The filter angles are assumed to be entered in an order of increasing or decreasing value. If entered in a decreasing order, they are reordering in ascending value. If the calibration list is not ordered, an error will be flagged. If no input error occurred, the calibration list is printed by routine PRTPAR and the user is prompted if the calibration list is to be edited. If so, the routine EDPAR is called. After editing, the cubic spline parameters are determined by the routine SPLFIT. In the latest version of PASCON, SPLFIT fits the calibration points with a natural cubic spline. Natural cubic spline algorithms are available in most general

numerical analysis texts as well as specialized manuscripts on splines<sup>87</sup>. The SPLFIT routine requires the list of filter angle calibration points (knots) to be in an ascending order. Three cubic spline parameters are generated for each calibration point. The STOPAR command can be used to store the calibration file and the accompanying cubic spline parameters.

If a calibration file already exists on the Nicolet hard-disk, it can be retrieved either through the CAL command or the GETPAR command. Although a calibration file contains the spline parameters along with the filter angle - wavenumber calibration pairs, the spline parameters are regenerated. This allows the calibration files to be edited externally to the PASCON program. A newly created calibration file or one retrieved from disk can be edited with the EDPAR command, stored with STOPAR and printed with PRTPAR. Once the calibration list is prepared, wavenumber calibration of the PA data can be carried out. If the CAL command was originally issued, the PA data wavenumber calibration process is automatically carried out. If the calibration file was loaded with the GETPAR command, the wavenumber calibration must be initiated with the PACAL command. The PACAL subroutine generates the birefringent

filter angle for each data point and passes it to the SPLINT routine. SPLINT searches the calibration list, determines the correct interval for the filter angle and using the spline parameters for that interval, it computes the corresponding wavenumber value. For the first data point a binary search is implemented after which the index from the previous search is used as the starting point of a linear search. At the end of the process, PACAL has a list of wavenumber values corresponding to the list of data points.

Although PACAL calibrates the PA in the wavenumber scale, it is not in a format compatible with the Nicolet FTIR36 and Beckman programs. The FTIR36 and Beckman programs record data on a linear wavenumber scale. In the Beckma program the data is collected with a 1.2207  $\text{cm}^{-1}$  resolution. The resolution of spectra collected with the FTIR36 program can be varied. The default setting of the program however was changed to 1.2207  $\text{cm}^{-1}$  resolution to facilitate the compatibility of the various data files. In addition to having this digital resolution, FTIR36/Beckma data has a fixed wavenumber index. Essentially a FTIR36 data file can be thought of as a vector of dimension 16834. At 1.2207  $\text{cm}^{-1}$  digital resolution, the first vector element corresponds to 0  $\text{cm}^{-1}$  the final vector

corresponds to 20000  $\text{cm}^{-1}$ . In order to convert the PA data into a compatible format, the wavenumber scale of the data must be linearized with the equivalent wavenumber index and digital resolution. The routine PACON accomplishes this.

The conversion routine, PACON, searches the wavenumber list for points which straddle a valid FTIR36/Beckman wavenumber value. The PA intensity of two points which bracket a FTIR36/Beckman value are averaged and this averaged intensity is given the corresponding FTIR36/Beckman index. A new PA intensity list is generated in this fashion with the FTIR36/Beckman digital resolution and indexing. Once the new list is generated, it can be stored as an FTIR36/Beckman file with the PDS or PSS command. The STOSPE subroutine generates the correct FTIR36/Beckman control block and writes the control block and data list to a named disk file. This file can now be loaded into Beckman and processed, displayed, and plotted with the FTIR routines.

All the photoacoustic data processing programs implement the compressed spectral storage format. This reduces the disk space requirements for the files, speeds up the file i/o, and reduces the memory requirements of the programs. There are resident Nicolet

programs which do not support this file structure. One such program which is frequently used is NIRCAP (Near InfraRed Curve Analysis Program). NIRCAP can not read converted files directly. The file must first be expanded to the full storage mode. This can be accomplished by loading the file into FTIR36 or Beckma with the GDx (x=S,B,D) and storing it with the appropriate PDx command. The file is then stored in the expanded format.

The PASCON program listing forms part of Appendix 2.

## CHAPTER 8 : MOLECULAR ORBITAL CALCULATIONS

Molecular orbital calculations provide insight or support for the interpretation of experimental observations. Predictions of molecular structure, minimum energy molecular conformations, conformational barriers, and vibrational force fields often aid in the understanding of vibrational overtone spectra. *Ab initio* molecular orbital calculations were used extensively throughout these studies.

Computations were performed in the MVS SP 1.3.3 operating system environment of an Amdahl 5870 equipped with floating point accelerator boards. Three molecular orbital programs were used: MONSTERGAUSS<sup>91</sup>, GAUSSIAN82<sup>92</sup>, and GAUSSIAN86<sup>93</sup>.

### i.) Geometry Optimizations

Geometry optimizations were carried out with the forced gradient methods available in the above programs. In the majority of cases, Davidson<sup>94</sup> and Murtagh-Sargent<sup>95</sup> optimizations were used in the MONSTERGAUSS and the Gaussian programs respectively. These methods have superior convergence properties for molecules which contain a ring system(s). When the geometry is to be used as input for a force constant calculation and small force constants are needed accurately, the TIGHT optimization option was used in GAUSSIAN86.

The majority of the geometry optimizations were carried out with near double zeta, split valence basis sets. Some larger molecules were optimized only at the minimal basis STO-3G level. For aromatic molecules, the ring was constrained to be planar. Polarization functions were added to the split valence basis set functions of molecules containing heavy atoms, when possible.

The discrepancies between predicted *ab initio* geometries and accurately determined experimental geometries are well

known<sup>96,97,98</sup>. In general STO-3G structures are less reliable than those predicted using higher level basis sets. Near double-zeta split valence basis sets give bond angles which agree closely with experiment. Predicted bondlengths however show considerable deviation from the absolute experimental values. These deviations however are considered to be highly systematic. In these studies, CH bondlengths, and in particular the relative differences between them, are the important structural parameters. The split valence basis sets consistently underestimate CH bondlengths<sup>96,99</sup>. Again these deviations are systematic and can be largely corrected by employing scaling factors. Correction factors for several different split valence basis sets have been proposed. Since for this work only the relative differences are important uncorrected bond lengths are reported.

## ii.) Torsional Potentials

Many of the molecules studied have groups which can undergo large amplitude torsional motions or inversions. The minimal STO-3G basis set level is often in reasonable agreement with experiment in terms of both the torsional barrier height and the minimum energy conformation<sup>100</sup>. Torsional potentials of a number of molecules were calculated at the STO-3G level. Each calculation was carried out by optimizing the molecular geometry at a series of fixed torsional angles. This method is sometimes called the torsional angle driving method. In the calculations, torsional angle increments ranged from 5° to 15° depending on the foldedness of the barrier and the size of the molecule. In some cases, torsional potentials were calculated with higher level basis sets. In general however only the minimum and maximum energy torsional conformers were calculated with the larger basis.

### iii.) Vibrational Force Fields<sup>101,102</sup>

The complete and partial valence coordinate force fields of a number of molecules were calculated. Force fields were calculated using three different methods: (1) The complete harmonic force fields of small molecules were calculated analytically using GAUSSIAN86; (2) The complete harmonic force fields of intermediate size molecules were calculated in an analytic-numeric fashion using the corresponding options of GAUSSIAN82 or GAUSSIAN86; (3) The partial force fields of the larger systems were determined by a manual analytic-numeric method. Methods (2) and (3) numerically differentiate the analytical gradient. Stepsizes for the finite difference grid ranged from 0.005 to 0.01 Å. In method (3) a subsection of the complete force field grid was constructed and the derivatives were calculated employing central difference formulas<sup>86</sup>.

The experimental and optimized geometries were used as the reference geometry in the molecular force field calculations. The main disadvantage with choosing the theoretical geometry as a reference is that the force constants calculated with different basis

sets cannot be directly compared. This is due to the different linear error term in the force constant which results from the different reference geometries for each basis<sup>103</sup>. In this work, only the force constants calculated at the same basis set levels are directly compared where theoretical reference geometries are employed.

Force constants were calculated at a number of basis set levels. Minimal basis set, STO-3G, calculations are known to drastically overestimate the diagonal force constants and show random variations in the off-diagonal terms<sup>102</sup>. The former errors can be largely corrected by empirically scaling the diagonal terms. The latter error is however a disturbing problem. Despite the difficulties, STO-3G force constants can aid in the analysis of overtone spectra.

Hartree-Fock calculations with split valence basis sets yield force constants which are superior to those obtained from STO-3G calculations. Diagonal stretching and bending force constants are systematically overestimated by 10-30%<sup>102</sup>. The off-diagonal terms are generally well behaved. In particular the larger coupling terms are reproduced within 10 to 30% of the experimental values. In order to accurately calculate the smaller off-diagonal force constants at

the theoretical reference geometry, the structure must be carefully optimized ensuring that the first derivatives are zero. Tightly optimized reference geometries were used when small off-diagonal force constants and higher order diagonal force constants were needed. In some cases, polarized split valence basis sets were used in the force constant calculations of molecules containing heavy atoms.

The higher order potential terms, in particular the diagonal cubic terms of the CH-stretching modes were calculated in some cases. These terms were calculated by evaluating the second or higher derivatives of the analytical gradient. The diagonal cubics and some of the cubic interaction terms can be numerically evaluated from a simple three point grid:  $r_0$ ,  $r_0 + h$ ,  $r_0 - h$ , where  $h$  is the stepsize. Stepsizes employed for numerical differentiation of the analytical gradient varied between 0.005 - 0.01 Å.

Vibrational frequencies determined from theoretically calculated force constants cannot be expected to compete with the accuracy of experimentally determined frequencies. This is especially the case for such low level calculations which completely neglect electron correlation. This does not mean that theoretical

force constants are useless. Since the errors in the diagonal terms are largely systematic, the relative values of the diagonal force constants can be reasonably accurate. It is precisely those diagonal valence force constants which largely determine the frequencies of the modes. A set of reliable theoretical relative XH stretching mode frequencies and anharmonicities provides a check of the zero order local mode assignment of the XH stretching overtone regions. Thus theoretically calculated diagonal force constants provide an independent way for assigning local mode spectra. This method will be used to corroborate many of the zero order LM spectral assignments made in this thesis.

Vibrational frequencies are largely determined by the diagonal internal coordinate force constants. Since vibrational frequencies can be accurately measured, in essence the absolute values of the diagonal force constants are known very accurately from experiment. Off-diagonal force constants however are usually poorly defined experimentally. In fact for polyatomic systems the construction of harmonic force fields from spectroscopic data is hampered by the fact that the available experimental data is insufficient to determine all the interaction terms. In the language of numerical

analysis, the construction of a complete harmonic force field for polyatomic systems from the available experimental data is usually a highly underdetermined problem. Thus theoretically calculated off-diagonal terms often are the sole source of very valuable information on the vibrational potential energy surface of the molecule.

Based on these factors, one of the more successful approaches for constructing accurate molecular force fields is to combine both experimental and theoretical data. Botschwina et al in a series of papers<sup>104</sup> have constructed anharmonic vibrational force fields in which the diagonal harmonic force constants are obtained from the fit to the experimental fundamental frequencies and the harmonic interaction terms are taken as the theoretical SCF values. A similar approach is pursued in this thesis. The diagonal harmonic and high order XH-stretching terms are obtained from a zero order local mode parameterization of the XH- stretching overtone progressions. The harmonic interoscillator coupling terms and the other harmonic mode interaction terms are obtained from the force field calculations. In this approach the role of various coupling pathways can be explored using the theoretically predicted coupling parameters. The dominant

couplings resulting in observable spectroscopic splittings can be further identified and assigned with the help of the theoretical interaction terms. Details of this approach along with the results are presented in the following Chapters of the thesis.

#### iv.) Dipole Moment Derivatives<sup>101,105</sup> and Overtone Intensity Calculations

Like the theoretical harmonic and anharmonic force constants, theoretical dipole moment derivatives and their use in transition intensity calculations aid in the assignment and understanding of vibrational overtone spectra. As discussed in Chapter 1, the intensities of vibrational transitions are often calculated within the linear dipole approximation. In this approximation only the first term in the multicoordinate Taylor expansion of the dipole moment operator (eqn 1.8) is retained.

$$\hat{\mu} = \hat{\mu}_0 + \sum_i \left( \frac{\partial \mu}{\partial q_i} \right)_0 q_i \quad (8.1)$$

The transition intensity between an initial state ( $\Psi_i$ ) and final state ( $\Psi_f$ ) is proportional to

$$I^{fi} \propto \left| \langle \Psi^f | \hat{\mu} | \Psi^i \rangle \right|^2 \quad (8.2)$$

The expression for LM intensities involve only XH stretching states where  $q_i$  are the local XH stretching coordinates<sup>106-108</sup>. The LM states,  $\Psi^i$  and  $\Psi^f$ , are Morse oscillator product functions. The matrix elements appearing in equation 8.2 involving Morse oscillator eigenfunctions have known analytical solutions<sup>4,26,27,109</sup> while the dipole moment derivatives are available from *ab initio* molecular orbital calculations.

Dipole moment derivatives are obtained by calculating the dipole moment at geometries systematically distorted from the reference geometry. Dipole moment derivatives are available by numerically differentiating this set of dipole moments by finite difference equations. The appropriate subroutines are resident in the GAUSSIAN86 program and are invoked by the option command, IOP(2/38=10), on the job card. These routines provide the cartesian coordinate dipole moment derivatives. A small set of routines were written to transform these dipole moment derivatives to local

valence coordinates. The method has been described previously<sup>110,111</sup>. Finite-difference, cartesian dipole moment derivatives and force constants contain spurious "non-zero" translational and rotational contributions<sup>111</sup>. An additional advantage of the transformation procedure, is that the dipole moment derivatives satisfy the Eckart-Sayvetz conditions<sup>7,112,113</sup> thus eliminating any translational and rotational contributions. The local coordinate dipole moment derivatives are used in the calculation of LM XH stretching intensities.

The theoretical dipole moment derivatives like the force constants were calculated at the SCF level of theory with modest split-valence basis sets. Electron correlation is needed for absolute accuracy when calculating vibrational frequencies<sup>114</sup> and intensities<sup>105</sup>. In addition, it has been shown that diffuse basis functions are important in order to obtain good dipole moment functions<sup>115</sup>. Despite these deficiencies, low-level dipole moment derivatives are very useful. For small molecules experimental techniques are capable of providing precise dipole moments. Uncertainty in the accuracy of the model Hamiltonians describing the vibrational motion of polyatomic systems makes experimental

interpretation of intensities highly model dependent. This problem is particularly acute in the description of the intensities of high energy vibrational transitions. The use of a theoretical dipole moment function in an intensity calculation provides an independent means of assessing the quality of model Hamiltonians.

**PART C : VIBRATIONAL OVERTONE STUDY OF  
FIVE-MEMBERED AROMATIC HETEROCYCLES**

## CHAPTER 9 : Zero Order Interpretations of the Aryl CH Stretching Spectral Regions of Aromatic Heterocycles

### i.) The Zero Order Local Mode Assignment

The iso- $\pi$ -electronic series; furan, thiophene, and pyrrole are of considerable fundamental interest as prototypical five-membered aromatic heterocycles. A comparison of the properties of these molecules helps clarify our understanding of the concept of aromaticity. In particular, a comparison amongst the molecules of this series allows one to investigate the role of the heteroatom and the structure of the five-membered ring on the properties of aromatic heterocycles.

Owing to the importance of these molecules, it is not surprising that their infrared and Raman spectra have been extensively studied<sup>116-121</sup>. The  $\Delta v=5$  and 6 CH-stretching overtone regions of the neat liquids have also been reported<sup>122</sup>. Despite the amount of work which has been done on these systems, a number of intriguing questions remain. The questions regarding the XH-stretching vibrations of these molecules are of particular interest

to this work.

The study of the 5-member aromatic heterocycles was initiated to compare substituent effects on the aryl overtone features with the effects observed on the spectral features of the substituted benzenes. The aryl stretching transitions of the aromatic heterocycles must be assigned. Considerable discrepancies exist in the reported assignments of the fundamental CH-stretching region (3200 - 3000  $\text{cm}^{-1}$ ) of furan, thiophene, and pyrrole<sup>121,123</sup>. The source of these discrepancies appears to be the congestion of features in this region along with the ill defined rotational band profiles in the gas phase spectra of these systems. Much of the difficulties encountered in the fundamental region disappear at the higher overtone levels. The XH-stretching overtone transitions are generally of much greater intensity than any other spectral features. The anharmonicity defects of nonequivalent oscillators tend to differ in a way that XH-stretching transitions become increasingly resolved at high energy overtones. The assignment of the XH-stretching vibrations is often greatly facilitated at the higher overtone regions as compared to the fundamental.

The normal mode predictions for the  $\Delta\nu_{\text{CH}} = 1$  CH stretching

regions of furan, pyrrole, and thiophene deviate considerably from the observations. The inadequacy of the NM description of XH stretching motion due to the omission of the effects of anharmonicity was discussed at some length in Chapter 1. The local mode model which includes mechanical anharmonicity at zero order tends to be a better starting point for the description of such motion. Most of the dominant XH stretching features in the fundamental and the overtone XH stretching regions are predicted by the LM approach.

At zero order, the LM approach models each XH group as an independent anharmonic oscillator. The frequency and anharmonicity parameters of each XH oscillator are in some way dictated by the chemical environment of the oscillator. Chemically equivalent oscillators have identical parameters while the parameters of nonequivalent oscillators differ. Through the differences in LM parameters, nonequivalent oscillators give rise to distinct overtone progressions. Associating each overtone progression with a type of XH oscillator of the molecule leads to a structural interpretation of vibrational overtone spectra. Structural interpretations have been successfully used to understand the vibrational overtone spectra of a wide range of molecules. Conversely, the overtone progressions can

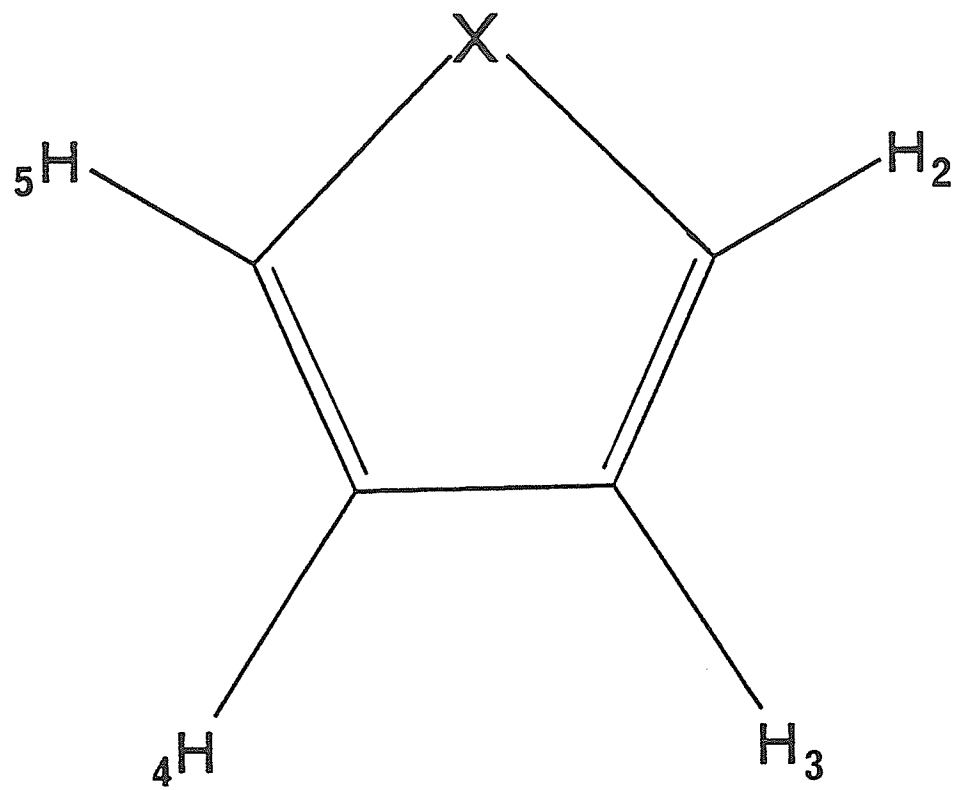
provide detailed structural information on the XH oscillators of the molecule. The chemical significance of the structural interpretation as well as the viability of this interpretation are discussed throughout this thesis. In this section however this property will be used to assign the overtone progressions.

The four aryl CH oscillators of furan, thiophene, and pyrrole partition into two sets of two equivalent oscillators (see Figure 9.1). Consistent with zero order predictions, two anharmonic aryl CH stretching progressions, one for each set of chemically equivalent oscillators, are observed. Typically, only the two CH stretching fundamentals or overtones are observed at the various levels of CH stretch excitation for these molecules. Figures 9.2 and 9.3 clearly show the two peak structure in the regions of 4 and 6 quanta ( $\Delta\nu_{\text{CH}} = 4, 6$ ) aryl CH stretch excitation for thiophene.

To facilitate the assignment of overtone spectra of thiophene, the aryl CH stretching progressions of a number of symmetrically disubstituted thiophenes were recorded. These molecules have only one type of aryl CH oscillator and hence only one aryl stretching progression is observed. Figures 9.4 and 9.5 show the single aryl CH stretching overtone in the  $\Delta\nu_{\text{CH}} = 4$  region of 2,5 dichloro, 3,4

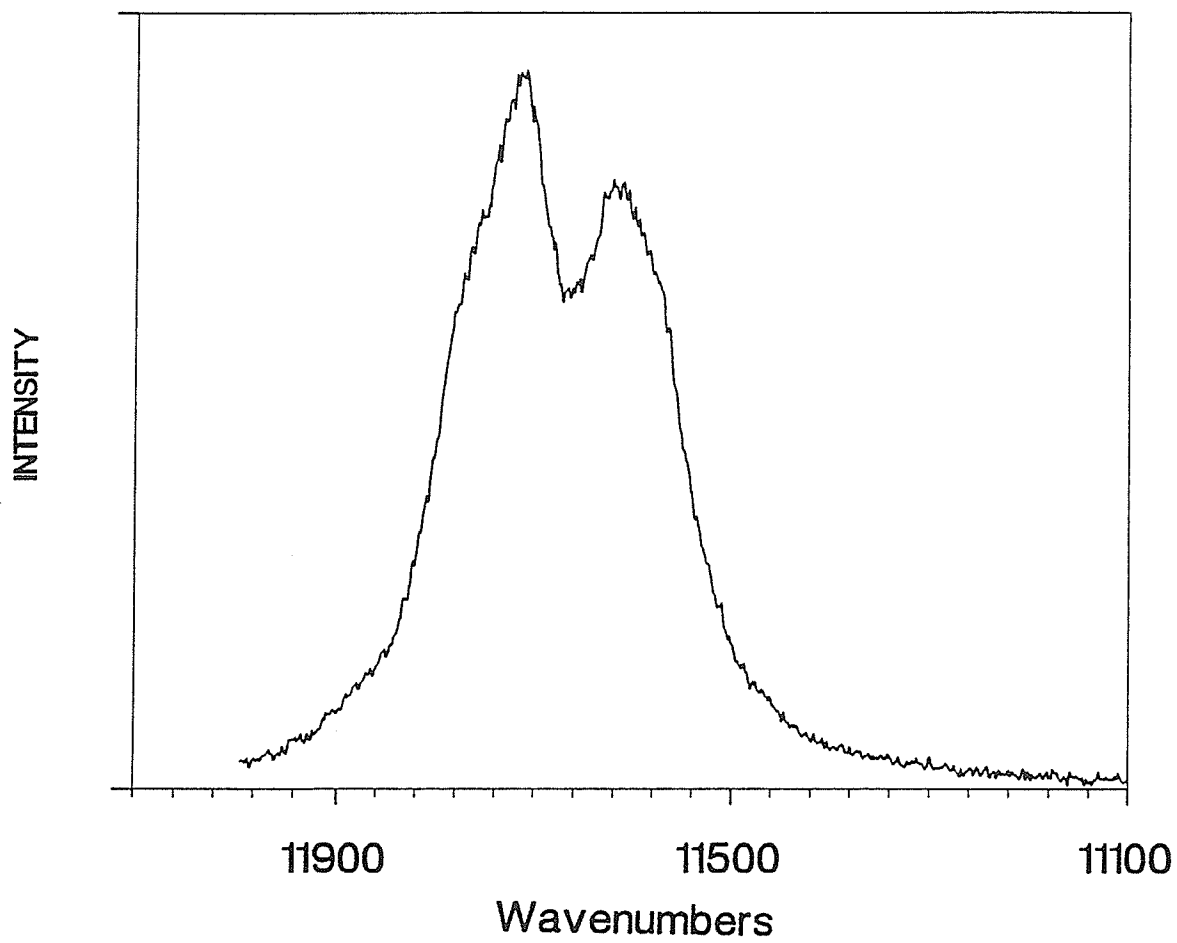
**FIGURE 9.1**

Diagram of the scheme used to label the aryl CH oscillators of the aromatic heterocycles where X=O,S,NH.



**FIGURE 9.2**

Liquid phase overtone absorption spectrum of thiophene in the  $\Delta\nu_{\text{CH}} = 4$  region. A sample cell of pathlength 5 cm was used.



**FIGURE 9.3**

Gas phase photoacoustic overtone spectrum of thiophene in the  $\Delta\nu_{\text{CH}} = 6$  region. The thiophene spectrum was measured at a pressure of 60 Torr with a 10 cm pathlength cell.

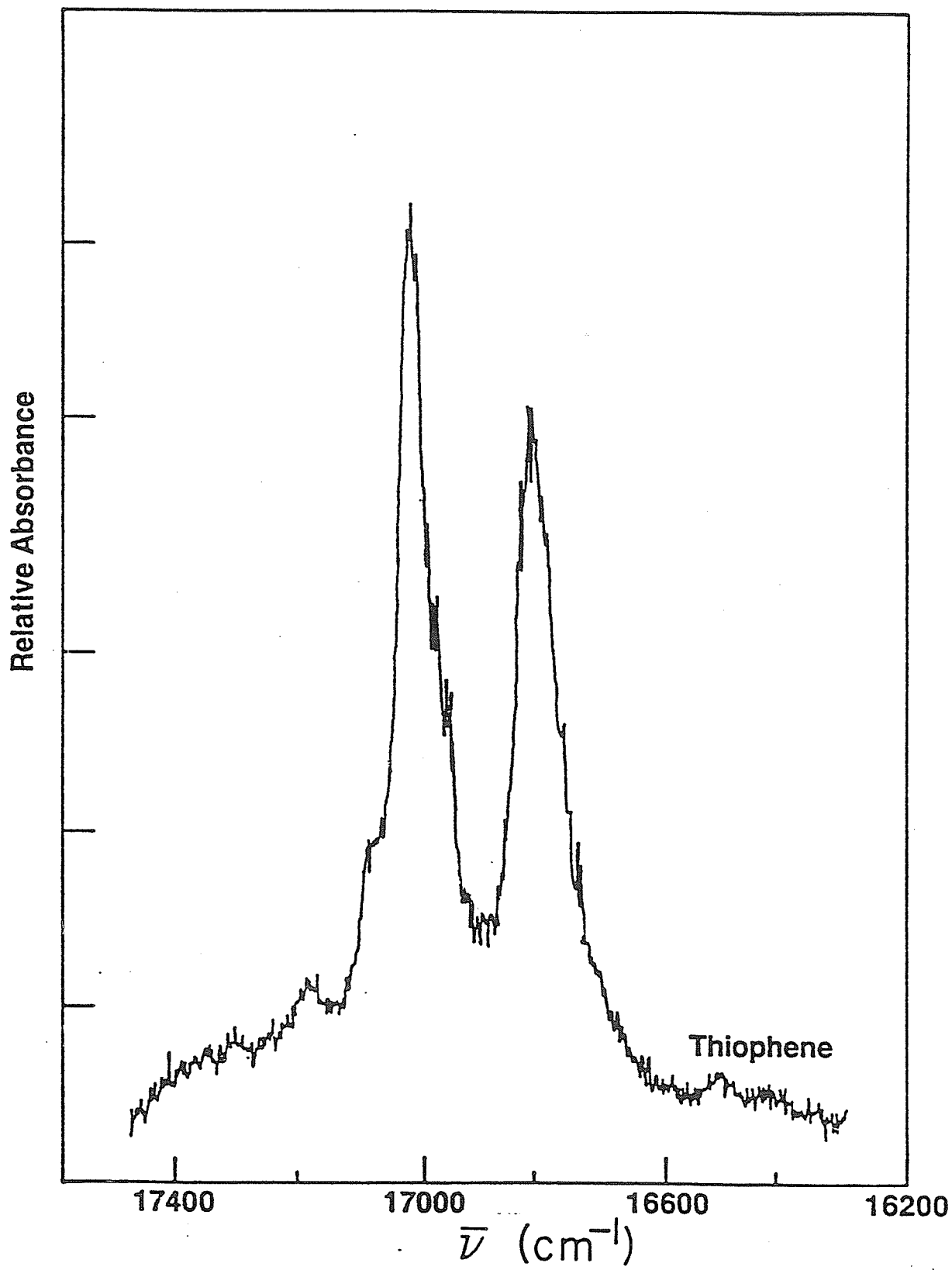


**FIGURE 9.4**

Liquid phase overtone absorption spectrum of 2,5 dichlorothiophene overlaid on the thiophene spectrum in the  $\Delta\nu_{\text{CH}} = 4$  region. A sample cell pathlength of 5 cm was used.

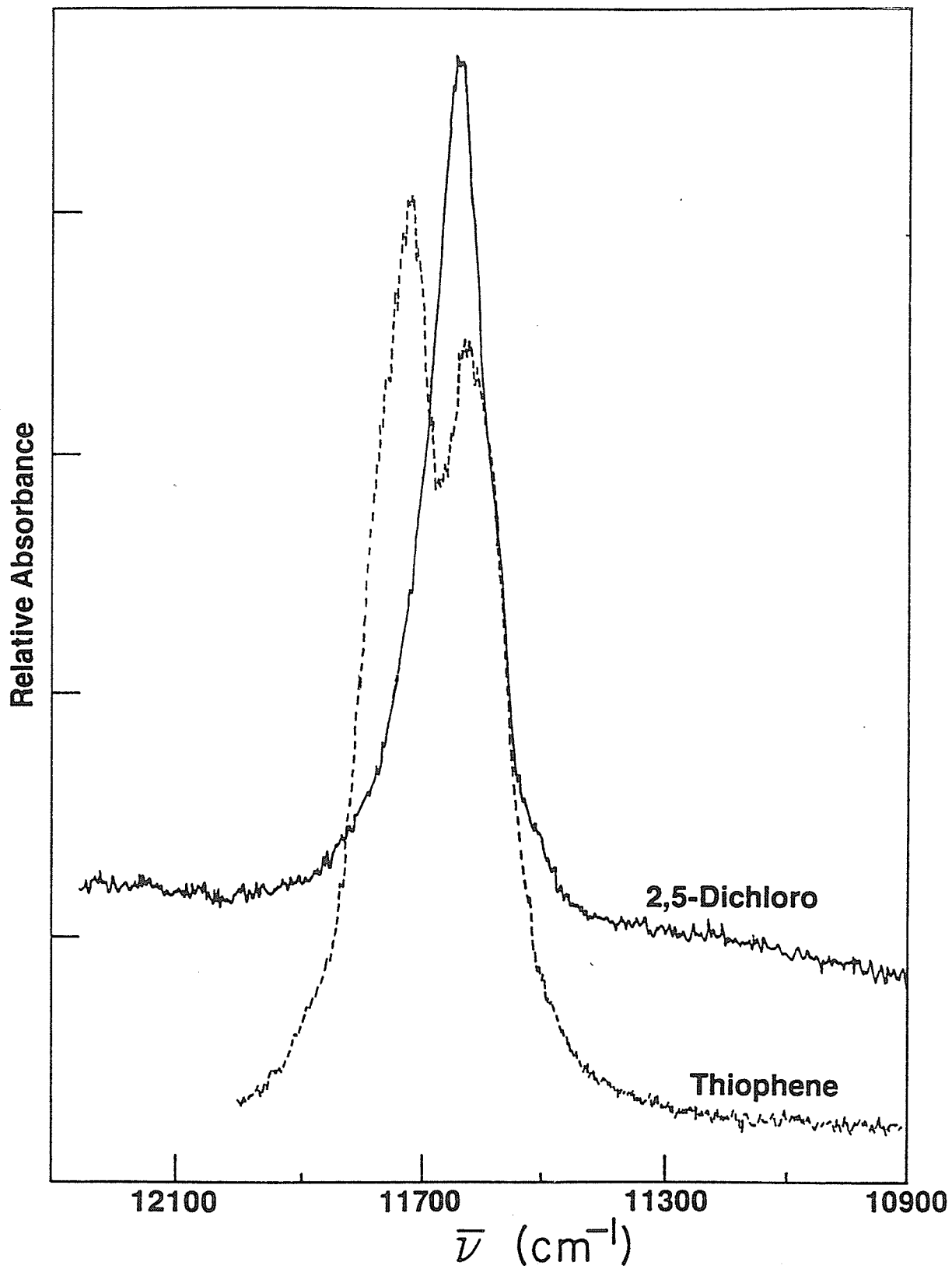
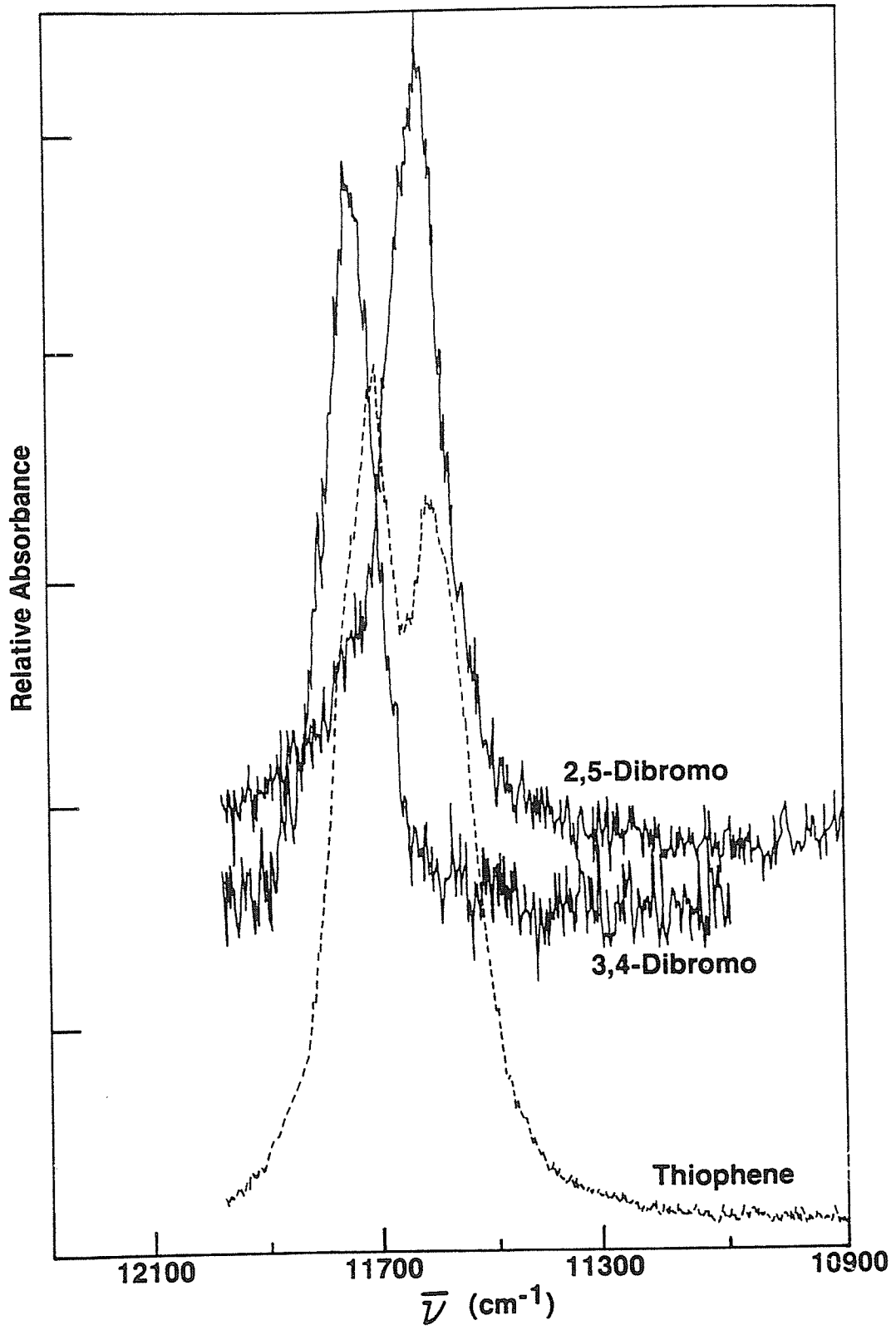


**FIGURE 9.5**

Liquid phase overtone absorption spectrum of 2,5 dibromothiophene and 3,4 dibromothiophene overlaid on the thiophene spectrum in the  $\Delta\nu_{\text{CH}} = 4$  region. A sample cell pathlength of 5 cm was used for the 2,5 dibromothiophene and thiophene spectra. A 2 cm cell was used for the 3,4 dibromothiophene sample.



dibromo, and 2,5 dibromothiophene. At a given level of CH stretch excitation, the aryl band of the 2,5 disubstituted species closely corresponds to the lower energy peak of the two peaks in the parent thiophene spectrum. The band of the 3,4 disubstituted molecules closely corresponds to the higher energy band of the parent molecule. Based on this correspondence, the progression with the overtone peaks at lower energy is assigned as transitions to the aryl CH-stretching states which we label as  $(|n_3 0_4\rangle \pm |0_3 n_4\rangle)$ . These are states in which the vibrational energy is localized within the C(3)H(3) and C(4)H(4) bonds. The higher energy progression is assigned as corresponding to transitions to the states  $(|n_2 0_5\rangle \pm |0_2 n_5\rangle)$  in which the vibrational energy is localized in the C(2)H(2) and C(5)H(5) oscillators. The fit of the assigned overtone progressions of thiophene to the Morse oscillator energy equation in the Birge-Sponer format is given in Figure 9.6. The overtone positions and the harmonic frequencies and anharmonicities obtained from the fit are presented in table 9.1. The high correlation coefficients are consistent with a good zero order LM description. At a given level of CH stretch excitation, the higher energy overtone is associated with the oscillators adjacent to the ring heteroatom

**FIGURE 9.6**

Birge-Sponer plot of the liquid phase aryl CH stretching overtone progressions of thiophene.

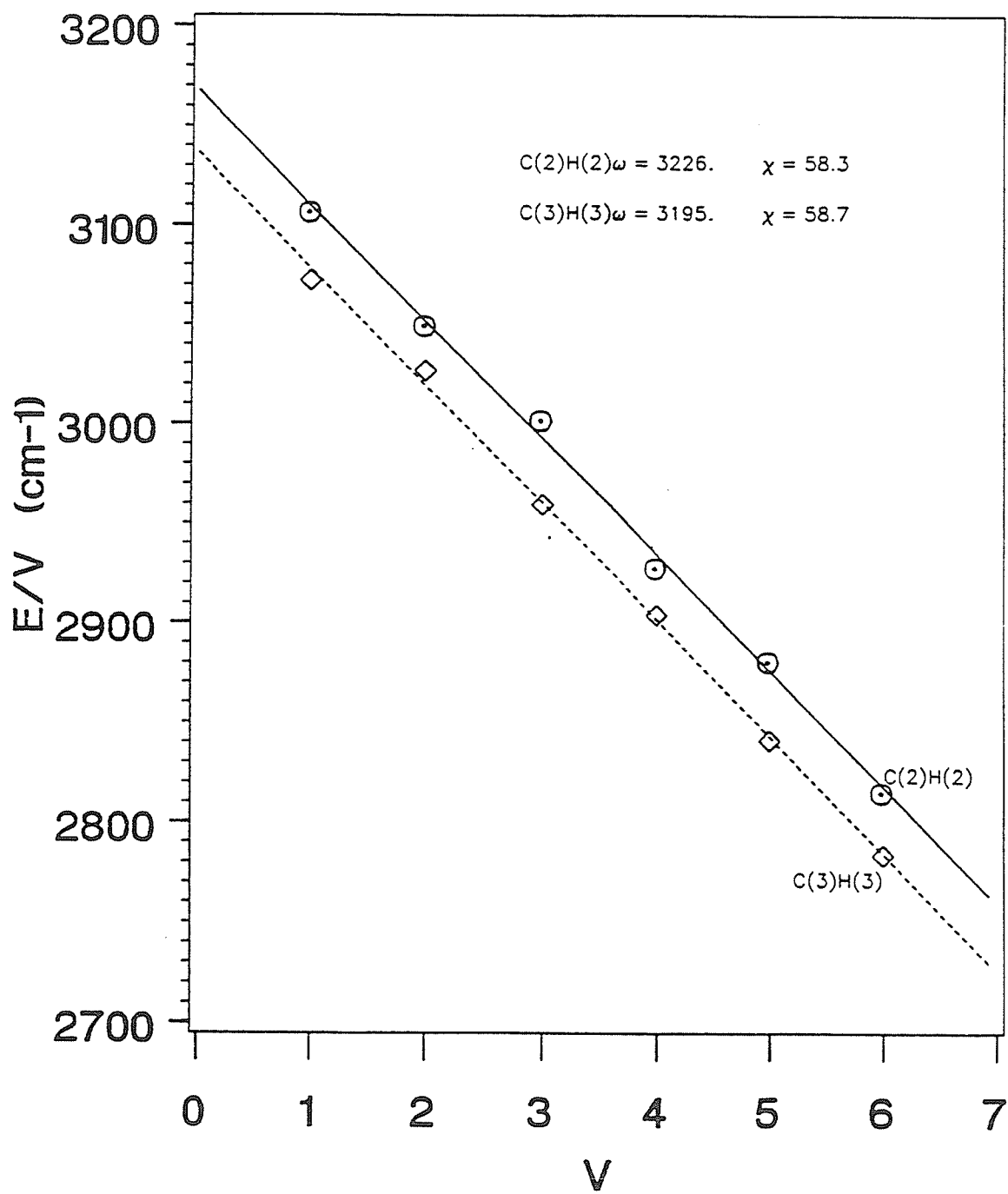


**TABLE 9.1**

Liquid Phase Aryl CH Stretching Overtone Peak Positions  
and Zero Order Local Mode Parameters of Thiophene.

v	Position of Overtone Maxima ( cm <sup>-1</sup> )	
	C(2)H(2)	C(3)H(3)
1	3107	3072
2	6099	6053
3	9006	8878
4	11711	11615
5	14404	14204
6	16890	16700
$\omega$	$3226 \pm 6$	$3195 \pm 5$
$\chi$	$58.3 \pm 1.5$	$58.7 \pm 1.2$
corr. coef.	-0.9986	-0.9992

while the lower energy overtone is associated with the oscillators at the 3 and 4 positions of the ring.

The overtone progressions of thiophene are rather well behaved and easy to identify. The progressions in the spectra of pyrrole and furan however are less easily distinguished. The  $\Delta\nu_{\text{CH}} = 3$  spectrum of furan (Figure 9.7) shows the expected two peak structure. The  $\Delta\nu_{\text{CH}} = 4$  spectrum no longer shows a clearly resolved two peak structure (Figure 9.8). The overtone region of the liquid phase spectrum is reasonably well fit by a broad single Lorentzian peak. The  $\Delta\nu_{\text{CH}} = 5$  liquid spectrum (Figure 9.9) shows a peak with a partially resolved shoulder. However, the gas phase photoacoustic spectra of furan in the  $\Delta\nu_{\text{CH}} = 5$  and 6 regions (Figures 9.10 and 9.11) clearly show a two peak structure. Comparing the aryl  $\Delta\nu_{\text{CH}} = 5$  photoacoustic gas spectra of 2 methyl and 2,5 dimethylfuran (Figure 9.12) with the same region of furan, the lower energy of the two peaks can be associated with the oscillators at the 3,4 positions on the heterocyclic ring. This is consistent with the observations at the lower overtones of furan as well as being consistent with the assignment of thiophene. The comparison with the overtone progressions of the methylfurans rules out the possibility of a

**FIGURE 9.7**

Liquid phase overtone absorption spectrum of furan in the  $\Delta\nu_{\text{CH}} = 3$  region. A sample cell pathlength of 2 cm was used.

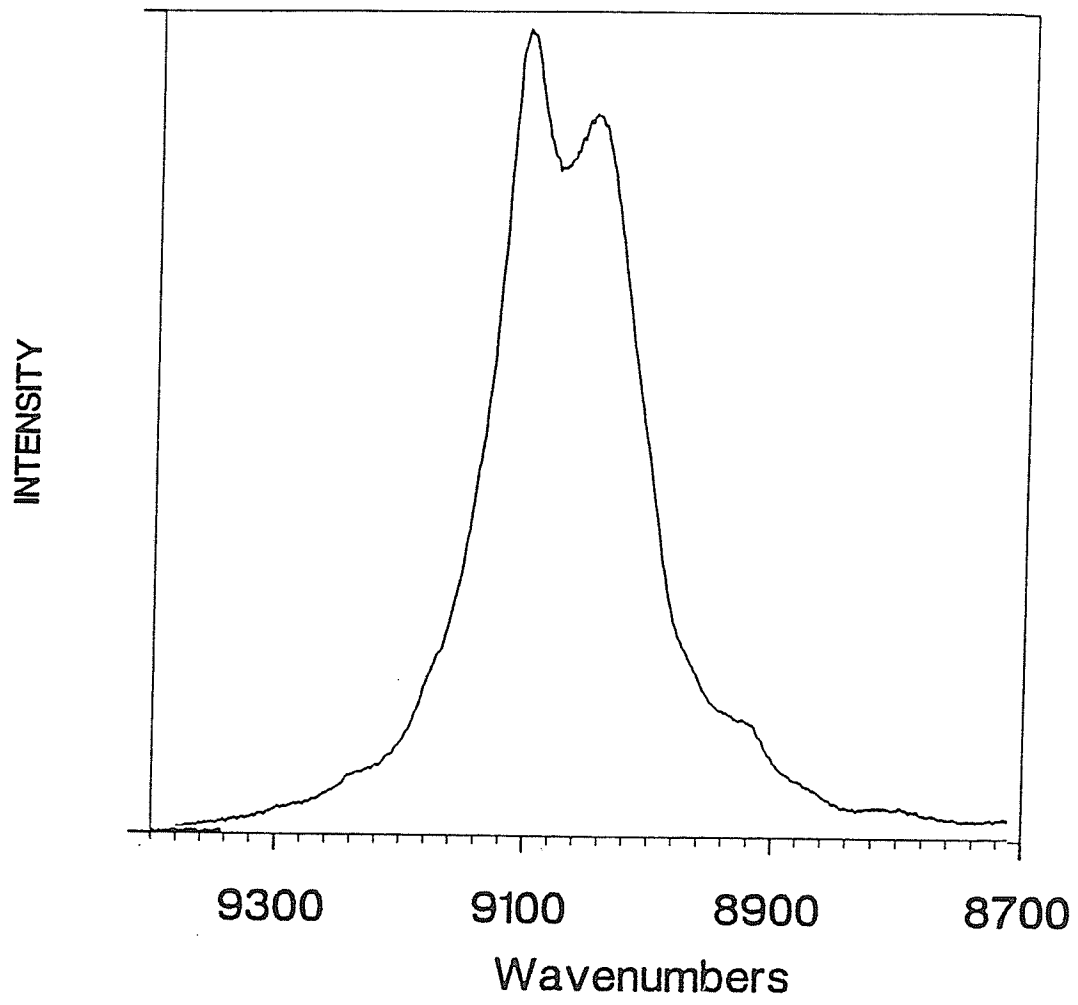


**FIGURE 9.8**

Gas phase overtone absorption spectrum of furan in the  $\Delta\nu_{\text{CH}} = 4$  region. The spectrum was measured at a pressure of 640 Torr with a 11.25 m pathlength.

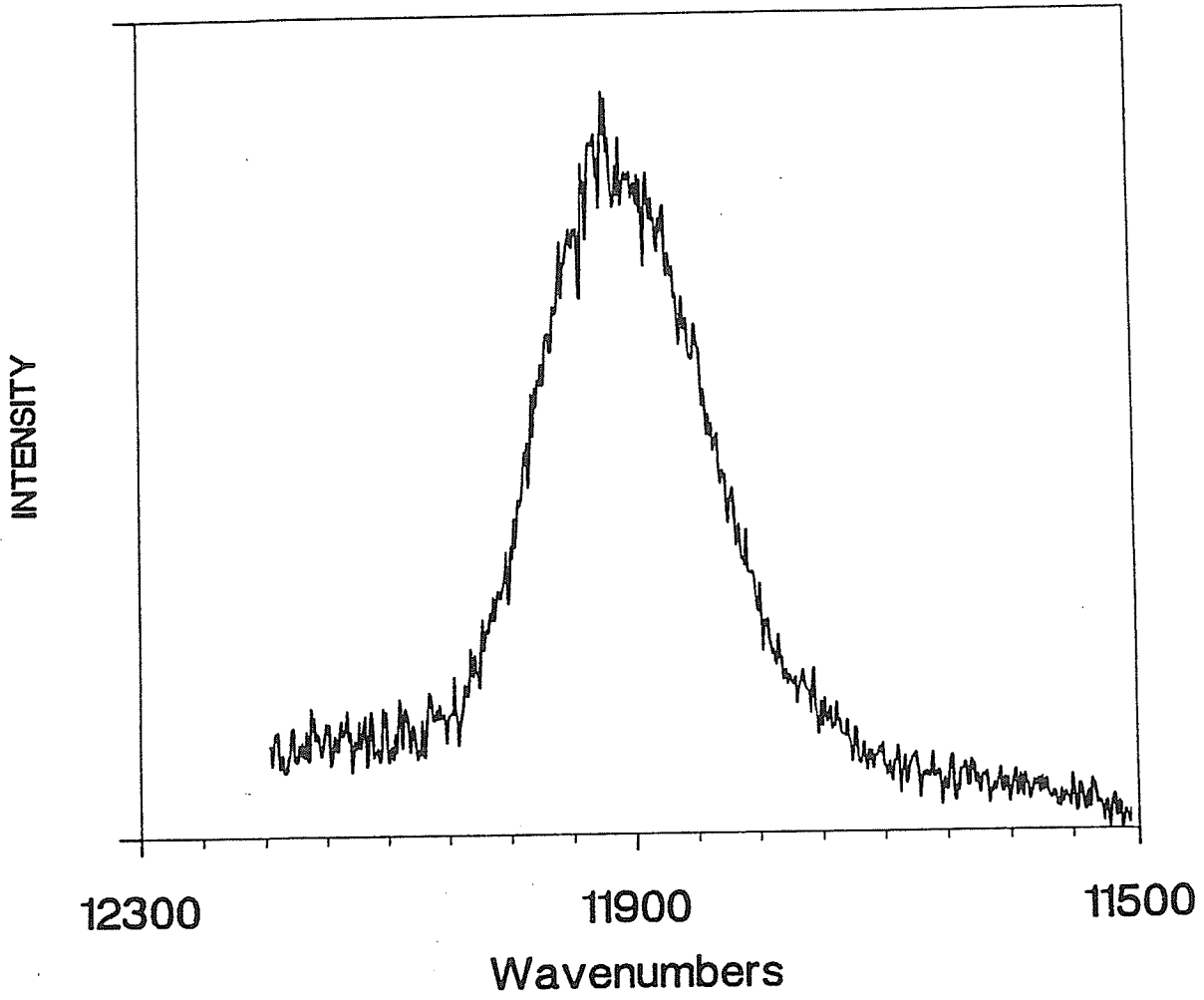


**FIGURE 9.9**

Liquid phase overtone absorption spectrum of furan in the  $\Delta\nu_{\text{CH}} = 5$  region. The spectrum was measured with a 5 cm pathlength cell.

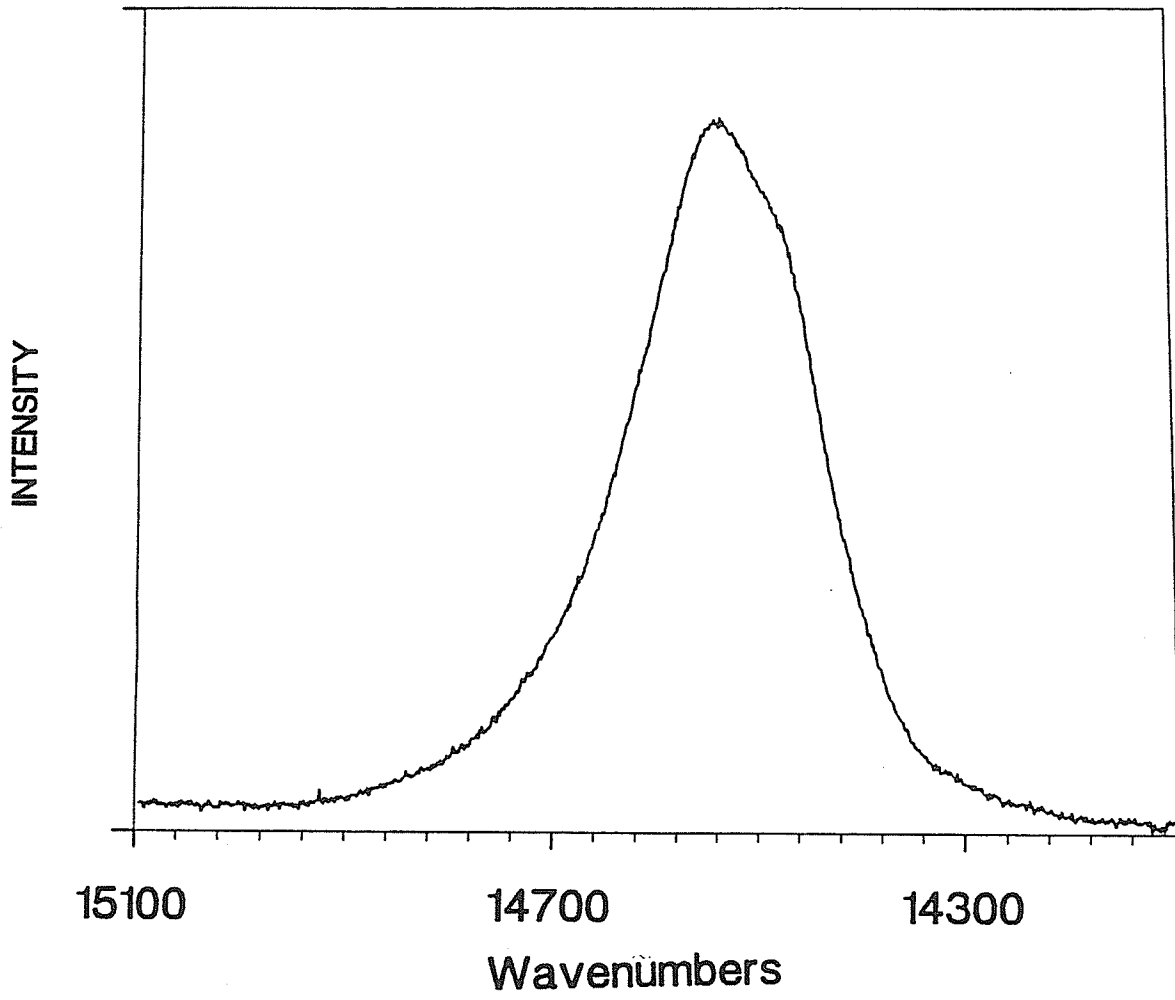


**FIGURE 9.10**

Gas phase photoacoustic overtone spectrum of furan in the  $\Delta\nu_{\text{CH}} = 5$  region. The spectrum was measured at 440 Torr of pressure with a 10 cm pathlength cell.

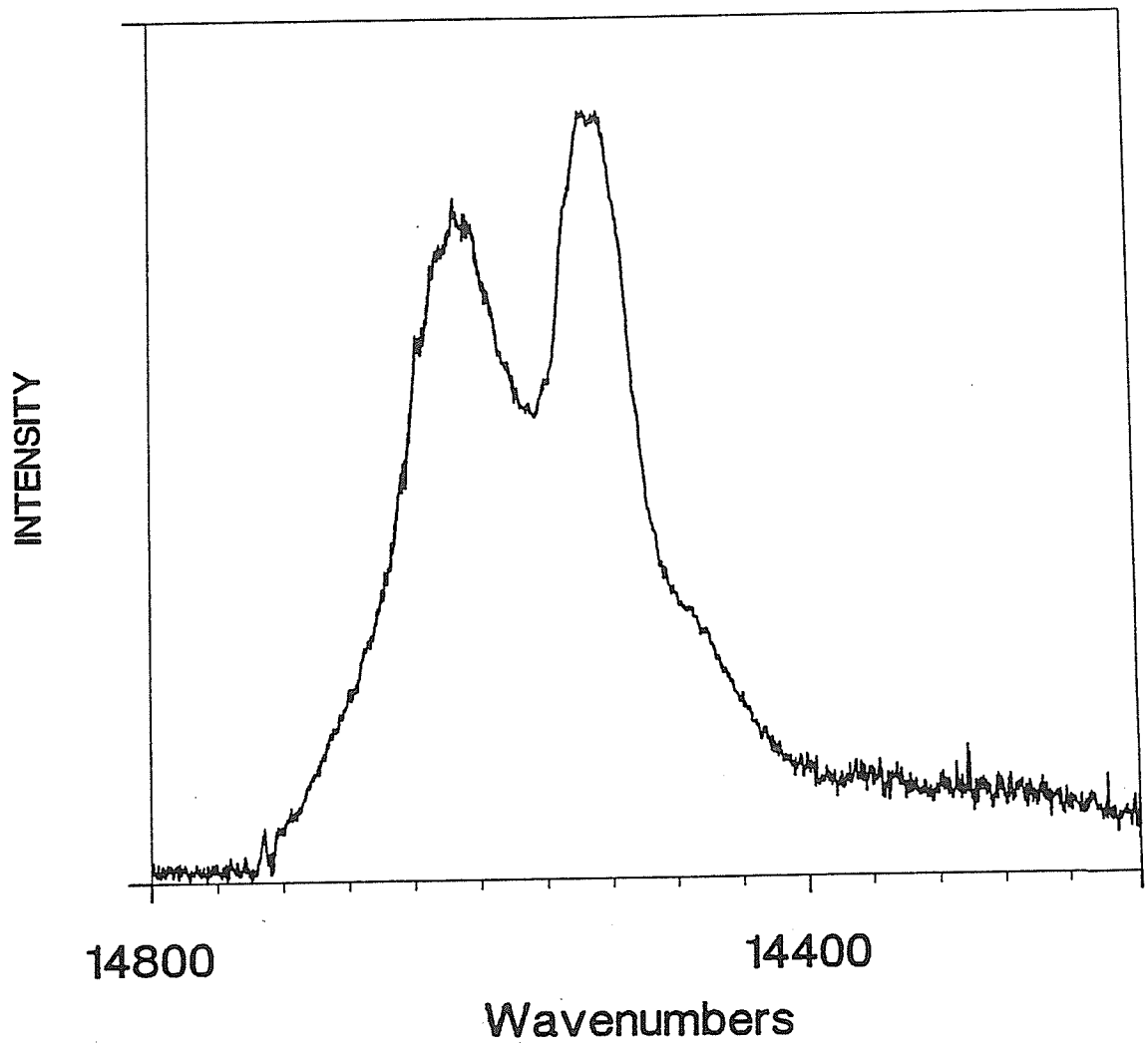


**FIGURE 9.11**

Gas phase photoacoustic overtone spectrum of furan in the  $\Delta\nu_{\text{CH}} = 6$  region. The spectrum was measured at 440 Torr of pressure with a 10 cm pathlength cell.

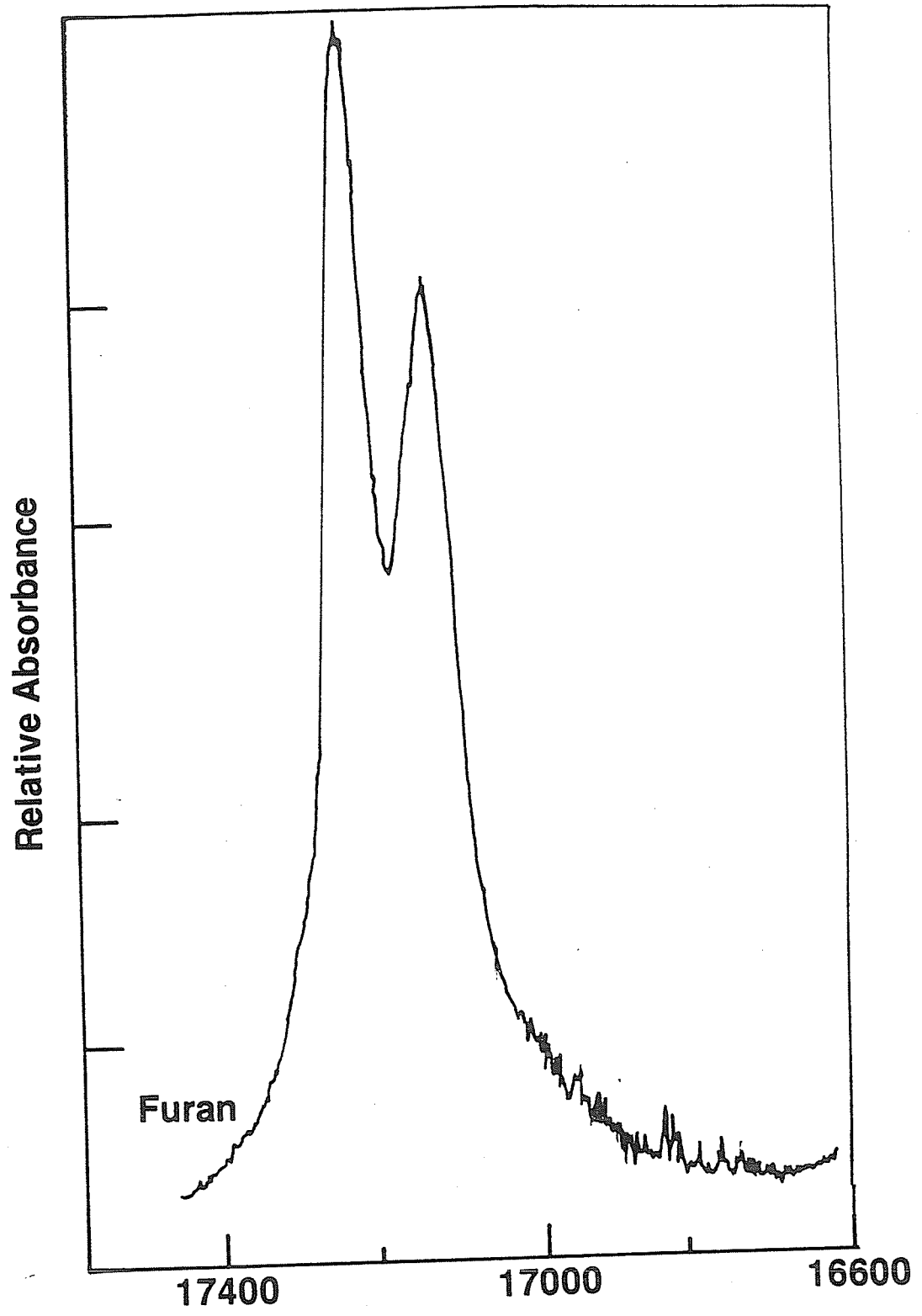
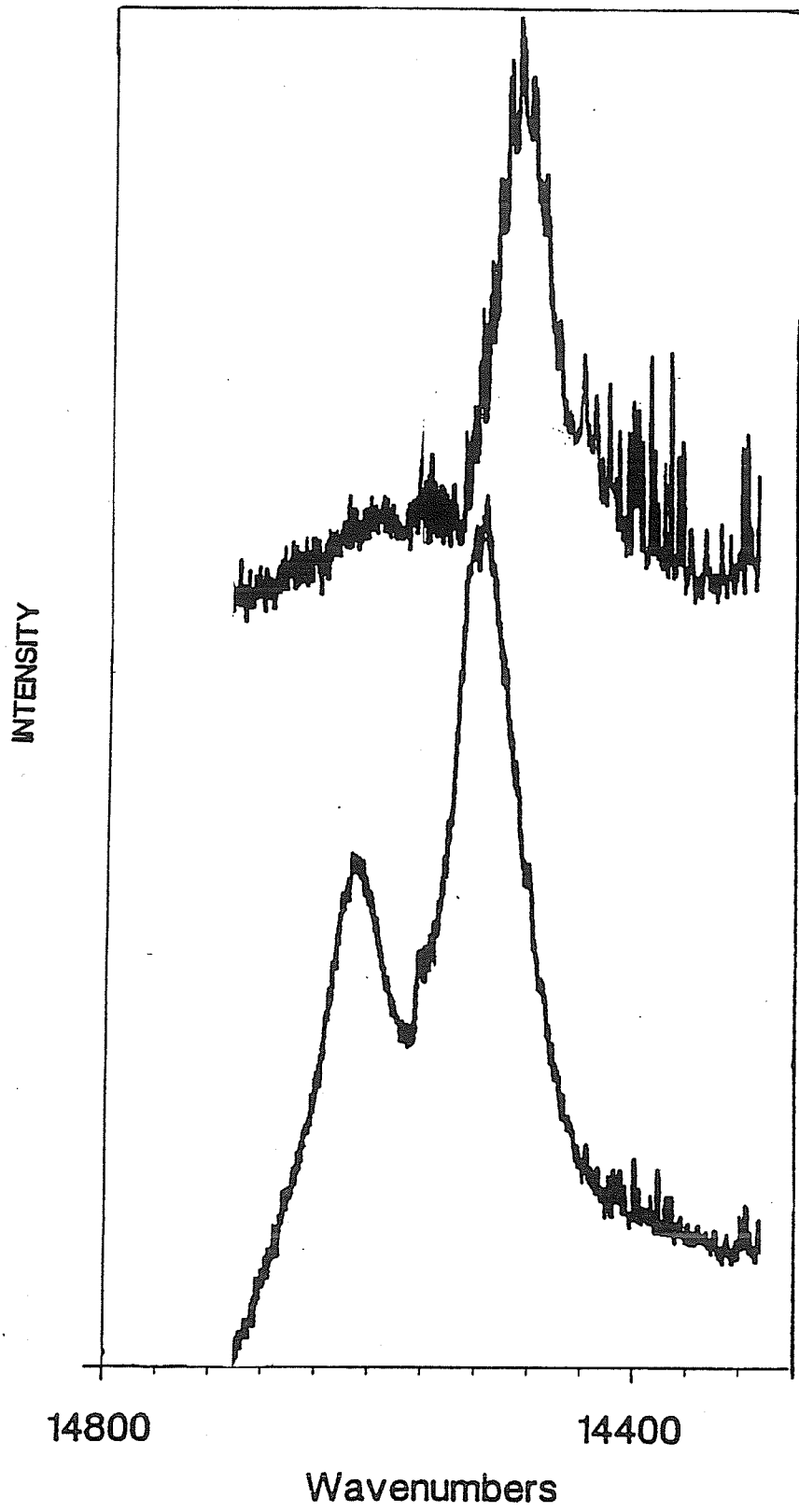


**FIGURE 9.12**

Gas phase photoacoustic overtone spectra of 2 methylfuran and 2,5 dimethylfuran in the aryl  $\Delta\nu_{\text{CH}} = 5$  region. Sample pressures of 110 and 68 Torr for 2 methylfuran and 2,5 dimethylfuran respectively were used in a 10 cm pathlength photoacoustic cell.



crossing of the overtone progressions associated with the nonequivalent oscillators. This will be discussed in more detail in Chapter 10. The assigned overtone peak positions of furan along with the zero order LM frequencies and anharmonicities are listed in table 9.2.

The aryl overtone progressions of thiophene and furan do not follow the same behaviour as the progressions of substituted benzenes. The difference is the most obvious in furan. Figure 9.13 shows the Birge-Sponer plot of the furan progressions. Figure 9.13 clearly shows the overtone progressions associated with the nonequivalent oscillators growing less distinct with increasing CH stretch excitation energy. The trend is less in thiophene than furan but still very different from that displayed by the progressions of substituted benzene systems. In benzene systems, overtone transitions associated with nonequivalent aryl oscillators become increasingly resolved at higher energy overtone regions. In view of the anomalous behaviour of the overtone progressions of furan and thiophene, additional evidence supporting our assignment and interpretations of the behaviour are warranted.

As corroboration of the zero order assignment, the isolated

---

**TABLE 9.2**

Liquid Phase Aryl CH Stretching Overtone Peak Positions and  
Zero Order Local Mode Parameters of Furan.

---

v	Position of Overtone Maxima ( cm <sup>-1</sup> )	
	C(2)H(2)	C(3)H(3)
1	3159	3129
2	6206	6158
3	9106	9044
4	11896	11835
5	14560	14476

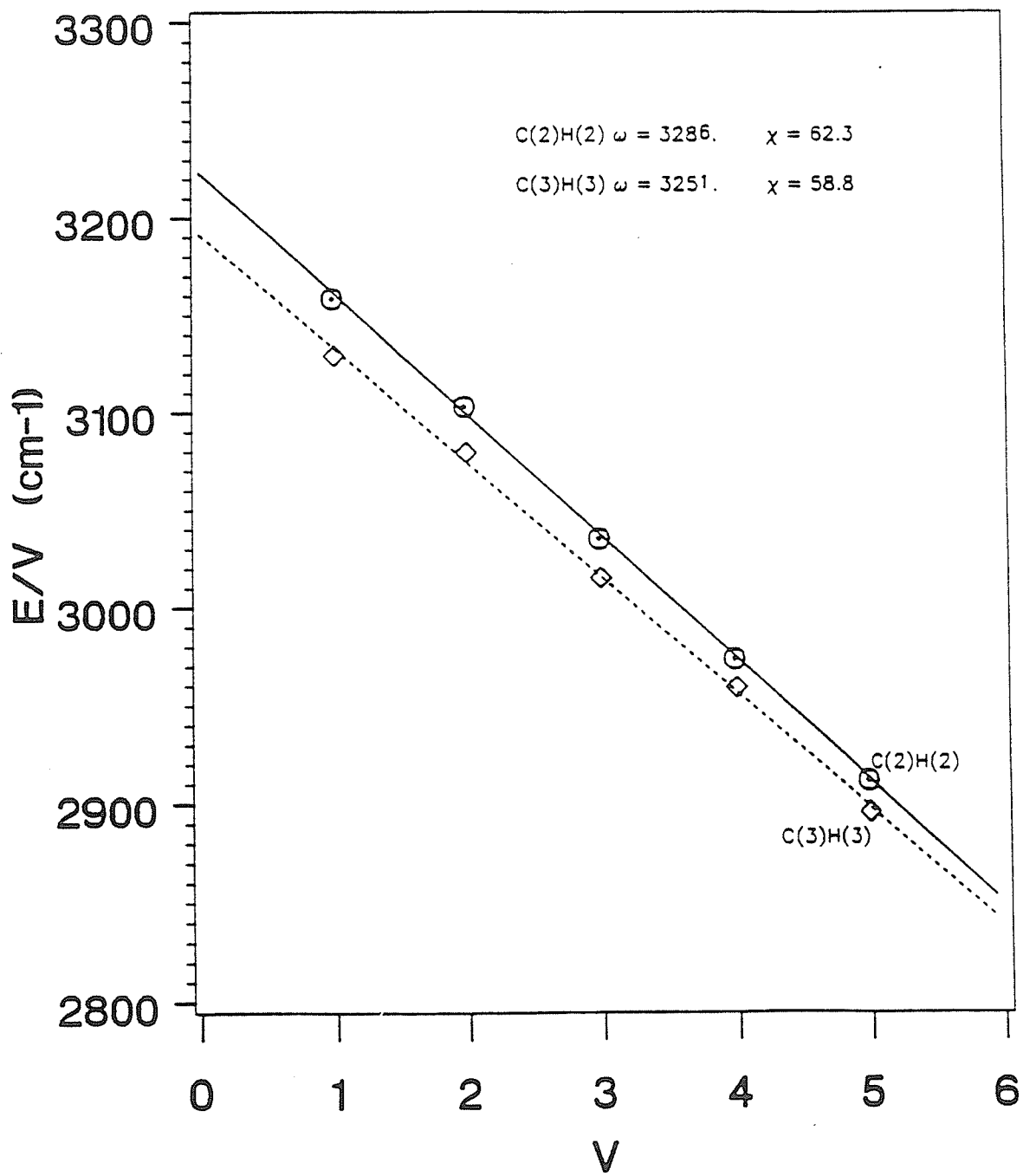
---

$\omega$	$3286 \pm 2.9$	$3251 \pm 4.3$
$\chi$	$62.3 \pm 0.9$	$58.7 \pm 1.3$
corr. coef.	-0.9997	-0.9993

---

**FIGURE 9.13**

Birge-Sponer plot of the liquid phase aryl CH stretching overtone progressions of furan.



oscillator harmonic frequencies and anharmonicities of thiophene, furan and pyrrole are calculated from the diagonal CH stretching terms of the partial anharmonic *ab initio* force field. The diagonal CH stretching force constants for furan, thiophene, and pyrrole at various basis set levels are listed in table 9.3. Consistent with the LM approach, the CH stretching modes are treated as isolated anharmonic oscillators. The modes are approximated as quartic oscillators,

$$V(q_i) = \frac{1}{2} f_{ii} q_i^2 + \frac{1}{6} f_{iii} q_i^3 + \frac{1}{24} f_{iiii} q_i^4 \quad (9.1)$$

In order to compare the spectroscopic parameterization of the isolated Morse potential with the diagonal *ab initio* anharmonic surface (9.1), the Morse potential is expanded as a truncated power series about the equilibrium CH bondlength.

$$V_{\text{MORSE}}(q_i) = a_i^2 D_i \left[ q_i^2 - a_i q_i^3 + \frac{7}{12} a_i^2 q_i^4 \right] \quad (9.2)$$

**TABLE 9.3**

The *Ab initio* Local Coordinate Aryl CH Stretching  
Force Field Parameters<sup>‡</sup> of Furan and Thiophene.

	Basis Sets			
	STO-3G	3-21G	6-31G	6-31G*
thiophene				
f <sub>22</sub>	7.663	6.544	6.575	6.473
f <sub>222</sub>	39.44	38.23	37.33	-
f <sub>33</sub>	7.648	6.353	6.360	6.335
f <sub>333</sub>	38.09	37.33	36.56	-
furan				
f <sub>22</sub>	7.663	6.544	6.575	6.473
f <sub>222</sub>	39.44	38.23	37.33	-
f <sub>33</sub>	7.648	6.353	6.360	6.335
f <sub>333</sub>	38.09	37.33	36.56	-

<sup>‡</sup> Quadratic and cubic force constants reported in mdynes Å<sup>-1</sup> and mdynes Å<sup>-2</sup> respectively.

The quality of the fit of the Morse potential to the anharmonic stretching progressions suggests that it has a good functional form. The quartic oscillator expansion (9.1) is equated term by term with the Morse oscillator expansion (9.2). This places a restriction on the value of the diagonal quartic force constant.

$$f_{iiii} = \frac{7}{9} \left( \frac{f_{iii}^2}{f_{ii}} \right) \quad (9.3)$$

Using the Morse oscillator restriction, the first and second order energy corrections to the zero order harmonic oscillator energy are determined in a harmonic oscillator basis for the quartic and cubic perturbations respectively. The zero, first and second order one dimensional oscillator energies are:

$$\epsilon_i^{(0)} (\text{cm}^{-1}) = \frac{\left( g_{ii} f_{ii} \right)^{\frac{1}{2}}}{2\pi c} \left( n + \frac{1}{2} \right) \quad (9.4a)$$

$$\epsilon_i^{(1)} (\text{cm}^{-1}) = \frac{7 h g_{ii}}{1152 \pi^2 c} \left( \frac{f_{iii}}{f_{ii}} \right)^2 (2n^2 + 2n + 1) \quad (9.4b)$$

$$\epsilon_i^{(2)} (\text{cm}^{-1}) = - \frac{h g_{ii}}{1152 \pi^2 c} \left( \frac{f_{iii}}{f_{ii}} \right)^2 (36n^2 + 36n - 15) \quad (9.4c)$$

Summing these energies, equations (9.4) can be expressed in terms of the parameters  $\omega_i$  and  $\chi_i$  of equation (1.9). The *ab initio* isolated oscillator frequencies and anharmonicities are listed in table 9.4.

The *ab initio* isolated oscillator frequencies and anharmonicities lend support to the zero order LM assignment of the aryl CH stretching progressions of furan, thiophene, and pyrrole. The magnitudes of the isolated frequencies and the calculated normal mode frequencies at a given basis set differ by at most 0.2% or about 6 cm<sup>-1</sup>. This is indicative of a good partitioning of the harmonic CH stretching potential in valence coordinates. Remember, this near valence coordinate separability is essential for a good LM description of the motion. The predicted frequencies are consistently higher than the experimental parameters. The *ab initio* frequencies computed at the experimental reference geometry are

TABLE 9.4

The *Ab initio* Isolated Oscillator Aryl CH Stretching  
Parameters of Furan, Pyrrole and Thiophene.

	Basis Sets							
	STO-3G		3-21G		6-31G		6-31G*	
	$\omega$	$\chi$	$\omega$	$\chi$	$\omega$	$\chi$	$\omega$	
	( cm <sup>-1</sup> )							
thiophene								
C(2)H(2)	3740	53.4	3456	68.7	3464	65.0		3437
C(3)H(3)	3736	50.0	3406	69.5	3408	66.6		3401
furan								
C(2)H(2)	3749	49.0	3487	70.0	3502	50.9		3472
C(3)H(3)	3766	48.3	3455	68.4	3456	53.5		3440
pyrrole								
C(2)H(2)	-	-	3399	69.9	-	-		3442
C(3)H(3)	-	-	3387	69.9	-	-		3425

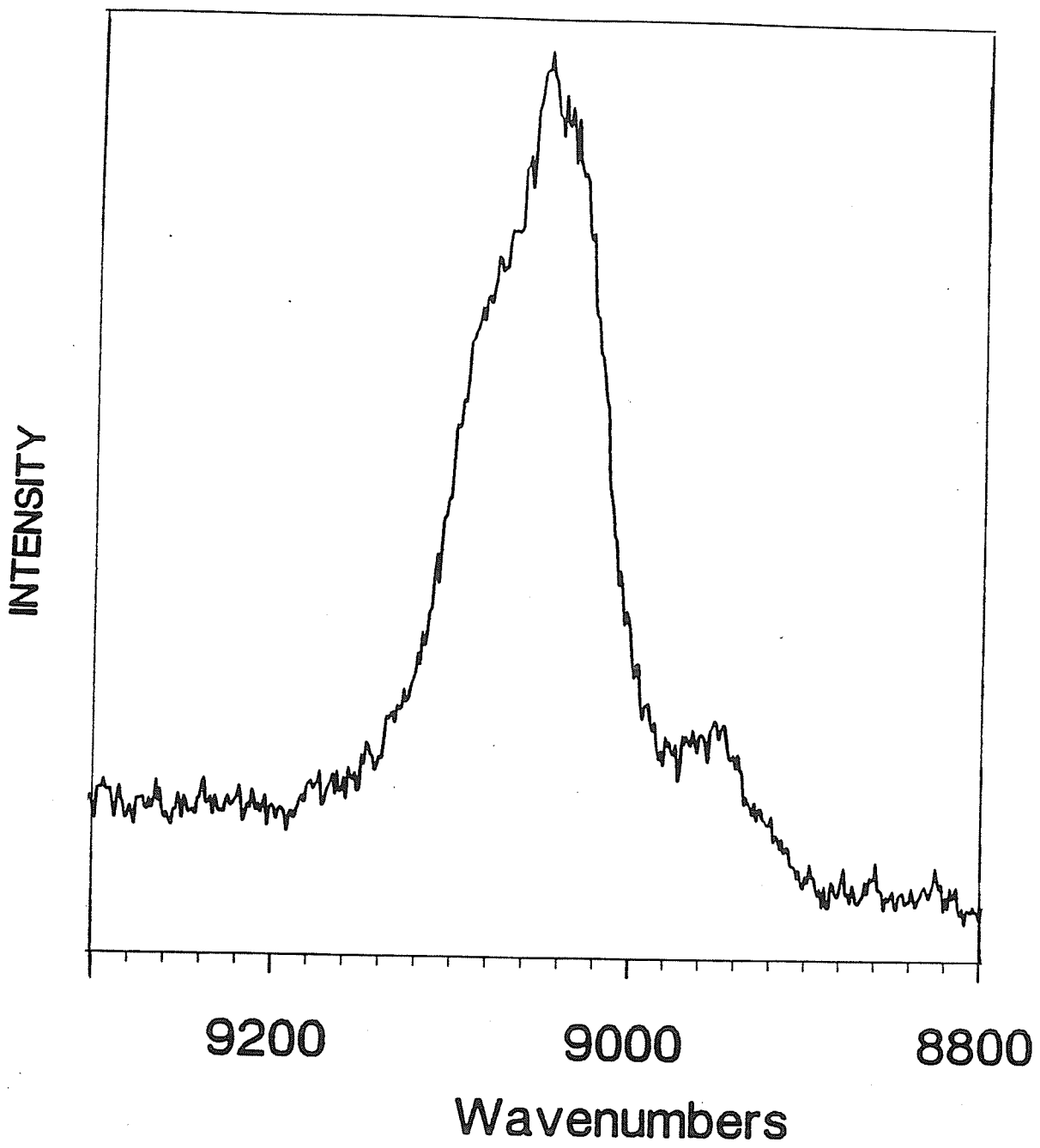
however closer in magnitude to the experimental values. The relative magnitudes of the *ab initio* parameters agree with the LM parameters. Notable exceptions are the values obtained from minimal basis set, STO-3G, potential energy surfaces. The relative ordering of the frequencies, furan > pyrrole > thiophene are reproduced by the split valence calculations. All the split valence results predict that the oscillators adjacent to the heteroatom have a higher frequency than those at the three and four positions of the ring. The frequency differences between the two sets of chemically nonequivalent oscillators are remarkably well predicted. The oscillators in furan and thiophene are predicted to have roughly the same frequency difference while the difference in pyrrole is predicted to be considerably smaller. Comparing the 6-31G\* parameters, the C(2)H(2) and C(3)H(3) frequencies differ by 32 and 36 cm<sup>-1</sup> in furan and thiophene but the difference is only 16 cm<sup>-1</sup> for pyrrole. The respective experimental frequency differences are 32 and 31 for furan and thiophene. The overtone progressions of pyrrole are not sufficiently resolved to give reliable experimental frequencies and anharmonicities. This is evident in the gas phase  $\Delta\nu_{\text{CH}} = 3$  spectrum of pyrrole where the two CH stretching overtones

are only poorly resolved (see Figure 9.14).

The relative agreement between the experimental and predicted anharmonicities is less impressive. The *ab initio* anharmonicities are very sensitive to the stepsize in the numerical force field calculation. This is especially true when the geometries were tightly optimized. The experimentally determined anharmonicities for the two sets of chemically nonequivalent oscillators in thiophene are nearly equal. Furan however is exceptional, particularly the liquid phase parameters. According to the assignment, the furan oscillators are more anharmonic than those of pyrrole and thiophene. In addition, the anharmonicities of the two oscillator types differ substantially in furan with the higher frequency C(2)H(2) oscillators having the larger anharmonicity. The results of the *ab initio* anharmonicity calculations are ambiguous. The trend in anharmonicities between thiophene, pyrrole, and furan is not predicted. Indeed, the calculations suggest that furan is more harmonic or at least not more anharmonic than both thiophene and pyrrole. At 3-21G, the predicted trend between the anharmonicities of the nonequivalent oscillators is somewhat consistent with the experimental values. However the limited numerical stability of

**FIGURE 9.14**

Gas phase overtone absorption spectrum of pyrrole in the aryl  $\Delta\nu_{\text{CH}} = 3$  region. The spectrum was recorded at a temperature of 85°C and with a 15.25 m pathlength.



computed anharmonicities suggests that small predicted differences are not reliable. *Ab initio* calculations are capable of providing accurate relative isolated oscillator frequencies but the calculated anharmonicities are of little predictive value. The small split valence basis sets employed in these calculations seem to be incapable of predicting the more subtle aspects of the CH stretching potential.

Comparing the overtone spectra of furan and thiophene with those of substituted species unequivocally identifies the CH stretching progressions in the spectra of the parent molecules. The experimental zero order LM parameters derived from the assignment are somewhat unusual as compared to those encountered in benzene ring systems. In particular, a trend between frequency and anharmonicity which is observed in overtone spectra of benzene systems is not strictly adhered to by the aromatic heterocycles. This is particularly true for furan and substituted furans. This has important consequences when discussing the structural significance of the overtone spectra of these molecules. The qualitative agreement between the experimental and computed *ab initio* frequencies provides further support for the zero order assignment

of the overtone regions of the aromatic heterocycles.

## ii.) Substituent Effects on LM Parameters

The main aspect of this study concerns itself with the chemical and structural interpretations of the XH-stretching vibrations. Again due to their simpler nature, chemical and structural trends can be more easily observed in the overtone regions. The role of substituents on the aryl CH-stretching overtones of the molecules is investigated and compared with the substituent effects observed in substituted benzenes. The study of substituent effects leads to a correlation of the overtone frequency shifts with differences in CH bondlengths. Bondlength - overtone frequency correlations have been studied extensively for a number of systems<sup>22,75,99,124,125</sup> including substituted benzenes<sup>130-134</sup>.

In the previous section the correspondence between the overtone features of symmetrically disubstituted furans and thiophenes was used to provide a zero order LM assignment of the overtone spectra of the parent furan and thiophene molecules. Closer comparison of the spectra reveals that there are small shifts between the corresponding overtone features of the parent and substituted species. For instance, the overtone peaks in the

dihalothiophene spectra in Figures 9.4 and 9.5 are shifted to the high energy side of the corresponding peak in the thiophene spectrum. A shift in the opposite direction is observed in the aryl CH stretching transitions of methyl substituted furans and thiophenes (Figures 9.12, 9.15, 9.16). These same trends have been observed in the aryl CH stretching overtone regions of substituted benzenes and have been rationalized in simple chemical terms<sup>126</sup>.

The shifting of CH stretching overtone frequencies by substituents has been known for some time. In the early 1927 overtone study by Barnes and Fulweiler, the shift in overtone band maxima of alkyl substituted benzenes was correlated with the mass of the substituent<sup>127</sup>. Since then, studies have concentrated on correlating the electronic effects of the substituent with the small overtone shifts<sup>128,129</sup>. In the early eighties, Mizugai and Katayama<sup>126</sup> recorded the liquid phase  $\Delta\nu_{\text{CH}} = 6$  overtone regions of thirty monosubstituted benzenes by thermal lensing spectroscopy. They correlated shifts in the band maxima with  $\sigma_I$ , the inductive part of the Hammett sigma. The experimental results showed that the greater the  $\sigma_I$  value of the substituent, the larger the shift of the overtone peak maximum. They concluded that the  $\pi$ -electron

**FIGURE 9.15**

Liquid phase overtone absorption spectra of 2,5 dimethylthiophene, 3 methyl and 2 methyl thiophene in the  $\Delta\nu_{\text{CH}} = 4$  region. An absorption cell of 10 cm pathlength was used for all the samples.

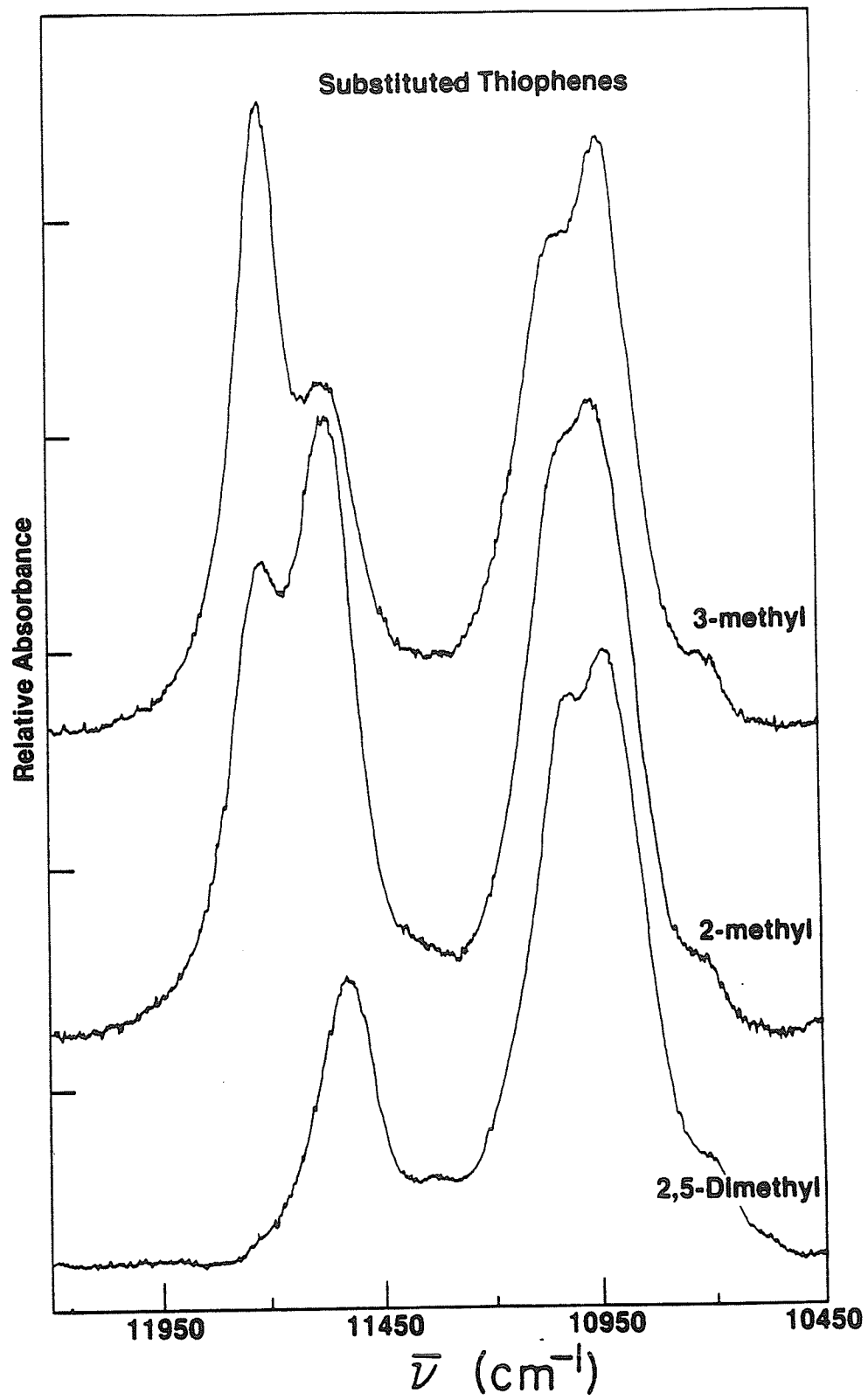
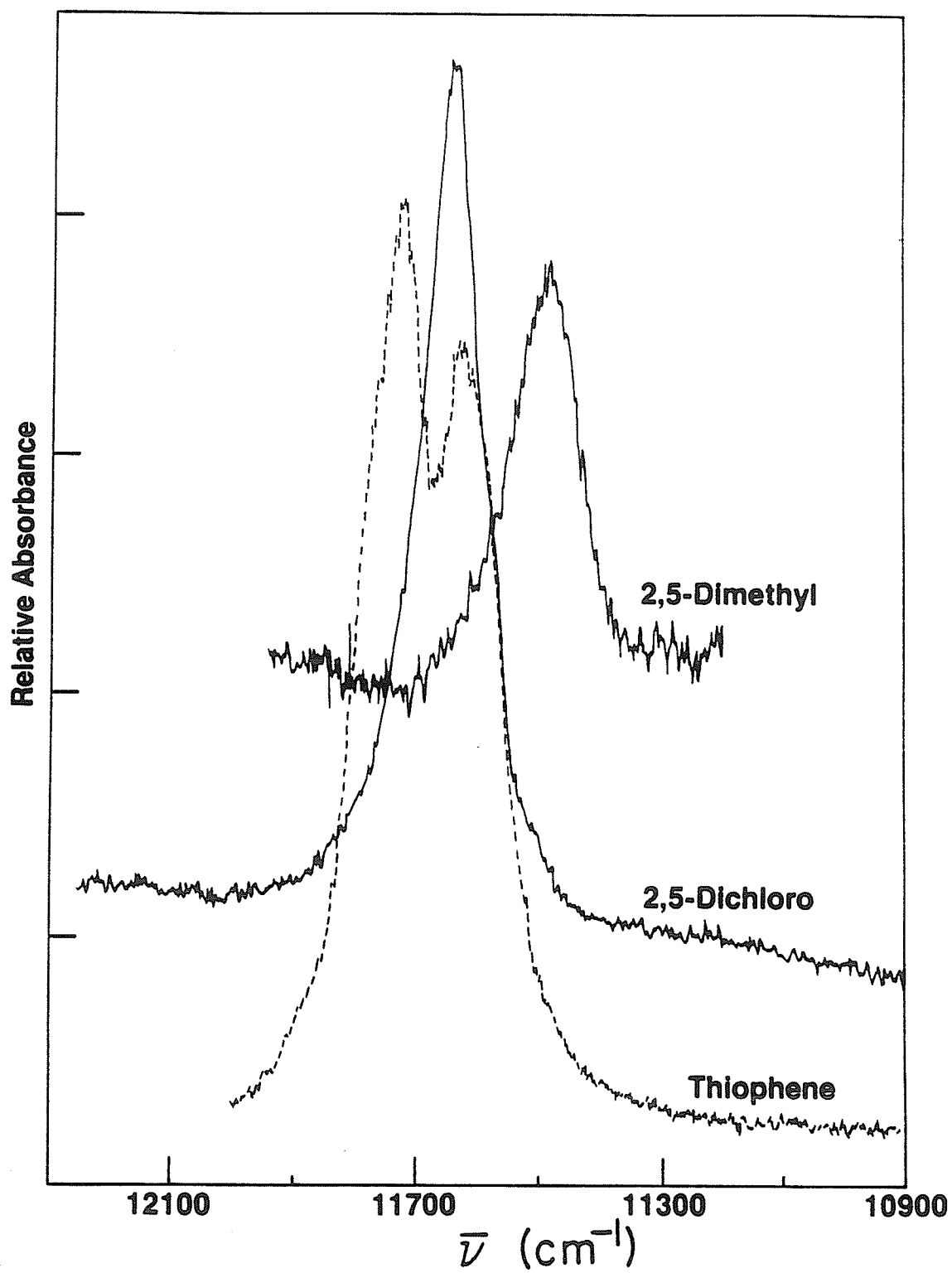


**FIGURE 9.16**

A comparison of the effects of halo and methyl substituents on aryl overtone position. Liquid phase overtone absorption spectra of 2,5 dichlorothiophene and 2,5 dimethylthiophene in the aryl  $\Delta\nu_{CH} = 4$  region. The spectra were recorded using 5 and 10 cm sample cell pathlengths respectively.



withdrawing strength of the substituent determined the amount the CH stretching transition was shifted to higher energy.

Substituent effects on the liquid phase overtone spectra of di and polysubstituted benzenes were further explored by Mizugai et al<sup>130</sup>, Gough<sup>131</sup> and Gough and Henry<sup>132</sup>. Again the substituent effects could be understood in terms of the electron withdrawing and donating properties of the substituent. These liquid phase investigations were extended to the gas phase. The overtone spectra of fluoro and methyl benzenes were reported by Gough and Henry<sup>133,134</sup>. The narrower overtone bandwidths encountered in the gas phase due to the decreased intermolecular interactions permitted partial resolution of the overtone features associated with the structurally nonequivalent oscillators of the molecule. Based on the gas phase overtone intensities and further evidence from liquid phase studies, it was concluded that the positions of the overtone bands associated with the oscillator immediately adjacent to the site of substitution were the most affected by the substituent. In the fluorobenzenes, fluorine being a good electron withdrawer shifted the overtone bands of the oscillator ortho to the substituent to higher energy relative to benzene. In methylbenzenes

a smaller shift was observed but in the opposite direction. This is consistent with the idea that methyl groups act as weak electron donors relative to hydrogens. The simple idea of relating the substituent induced shift in overtone maxima with the electron withdrawing or donating character of the substituent works very well, at least at a qualitative level for substituted benzenes.

Although the geometry and symmetry of the aromatic ring system grossly differ between benzene and 5-membered aromatic heterocycles, there is considerable evidence for similar electronic effects of substituents in these molecules<sup>135</sup>. The Hammett equation holds well for the  $pK_a$  of substituent heterocyclic carboxylic acids<sup>136</sup>. Electrophilic substitution of thiophenes follows a linear free energy relationship<sup>137</sup>. The proton chemical shifts<sup>138</sup>, CH deformation frequencies<sup>139</sup> and ring stretching intensities<sup>140</sup> of furans and thiophenes have also been related to the Hammett sigma parameters. The ideas governing the shifts in the maxima of CH stretching transitions of substituted benzenes seem to be directly applicable to the understanding of the substituent effects observed for the aromatic heterocycles. Despite the usefulness of this concept, it really in no way explains the effect in the language of a

physical model of molecular vibration. Instead we have to ask how the electronic rearrangement accompanying substitution affects the molecular potential energy surface. In spite of our intuitive rationalization of the phenomenon, the zero order LM parameterization of the stretching progressions suggests that substitution has very specific effects on the molecular force field. Does our chemically intuitive description of substituent effects and our spectroscopic parameterization of the effect have any common basis and additional support?

In an attempt to answer such questions, Gough and Henry<sup>133</sup> appealed to the results of *ab initio* molecular orbital calculations. In particular they examined the calculated Mulliken electron populations centered on the carbon and hydrogen atoms. The Mulliken populations suggested that the ionic contributions to the CH bond were altered considerably upon substitution. In other words, an electron withdrawing substituent ortho to a CH bond tended to increase the charge difference centered on the C and H atom which manifests itself as an increase in bond strength. An electron donating substituent had the opposite effect. These predictions are consistent with simple chemical ideas of charge flow. The increase

or decrease in CH bond strength was reflected in a change in the predicted CH bondlength. This led to the very fruitful investigations of the correlation of CH bondlength differences and shifts in overtone maxima<sup>131,133,134</sup>. This correlation will be discussed in more depth in the next section of this Chapter.

The ideas of Gough and Henry still need to be extended one step further to relate the substituent effects to the LM parameterization of the overtone spectra. The zero order LM parameterization of a progression of CH stretching transitions fits the observed maxima of the transitions to the anharmonic oscillator equation (1.9). In the parameterization of substituted benzenes, the shifts in maxima are largely absorbed in the LM frequency parameters. The anharmonicity parameter was often found to be largely unaffected by substitution<sup>131</sup>. This parameterization implies that the small shift in overtone maxima predominantly arises from a change in the diagonal quadratic valence CH stretching force constant. Higher order diagonal anharmonic terms play little or no role. Also, since the effect is parameterized within the zero order LM model, the quadratic and higher order interaction terms in the kinetic and potential energy are ignored by the treatment. Does the substituent

effect on overtone maxima in aromatic heterocycles, display the same LM parameterization as the benzenes? In addition are the LM parameters supported by the *ab initio* results?

The liquid phase peak positions for the assigned overtone transitions and the zero order LM parameters of methyl and halo substituted furans and thiophenes are listed in tables 9.5 and 9.6. The computed *ab initio* isolated oscillator frequencies are given in table 9.7. The LM frequencies and anharmonicities are both modified upon substitution on the heterocyclic ring. The frequency shift relative to the parent molecule is in the expected direction for the substituted molecules with the exception of 3,4 dibromothiophene. The LM CH stretching frequency is lower in this molecule than the frequency of the corresponding oscillator in thiophene. The oscillator anharmonicities increase upon substitution. Again 3,4 dibromothiophene is exceptional. The split valence *ab initio* results out perform the minimal basis set numbers. A comparison of the 3-21G frequencies shows that both the direction and magnitude of the frequency shift in 2,5 dichlorothiophene, methyl thiophenes, and methyl furans agree closely with the experimental results. The STO-3G values are often unable to predict the correct direction of the

**TABLE 9.5**  
 Liquid Phase Aryl CH Stretching Overtone Peak Positions  
 and Zero Order Local Mode Parameters  
 of Symmetrically Disubstituted Thiophenes.

v	Position of Overtone Maxima ( cm <sup>-1</sup> )			
	3,4 dibromo	2,5 dibromo	2,5 dichloro	2,5 dimethyl
1	3101	3096	3102	3066
2	6126	6068	6088	6014
3	9020	8908	8902	8828
4	11759	11640	11673	11524
5	-	-	14287	-
$\omega$	3217 ± 13	3220 ± 2	3224 ± 7	3191 ± 1.9
$\chi$	54.0 ± 4.6	62.2 ± 0.7	61.5 ± 2.2	61.9 ± 0.7

TABLE 9.6

Liquid Phase Aryl CH Stretching Overtone Peak Positions  
and Zero Order Local Mode Parameters of some Substituted Furans

v	Position of Overtone Maxima ( cm <sup>-1</sup> )		
	2 methyl		2,5 dimethyl
	C(5)H(5)	C(3,4)H(3,4)	
2	6199	6147	6122
3	9069	9025	9011
4	11876	11796	11711
5	14536	14442	14421
$\omega$	3284 ± 12	3256 ± 3	3242 ± 15
$\chi$	63.1 ± 3.2	61.5 ± 0.9	60.6 ± 4.2

TABLE 9.7

The *Ab initio* Isolated Oscillator Aryl CH Stretching  
Parameters of Some Substituted Thiophenes and Furans.

	Basis Sets		
	STO-3G	3-21G	6-31G
( cm <sup>-1</sup> )	$\omega$	$\omega$	$\omega$
3,4 dibromothiophene			
C(2)H(2)	3741	3374	-
2,5 dibromothiophene			
C(3)H(3)	3738	3200	-
2,5 dichlorothiophene			
C(3)H(3)	-	3429	3430
2,5 dimethylthiophene			
C(3)H(3)	3732	3390	3390
2,5 dimethylfuran			
C(3)H(3)	3764	3446	3444

shift in overtone maxima. The 3-21G frequencies of the dibromothiophenes are 80 and 200  $\text{cm}^{-1}$  lower than the respective parameters for thiophene. Although the frequency of the CH oscillators in 3,4 dibromothiophene is predicted to be higher than the frequency of the oscillators in the 2,5 dibromo species, the frequency difference of 174  $\text{cm}^{-1}$  is totally inconsistent with the observed spectra. The trends in anharmonicity are only poorly reproduced by the minimal and split valence basis set calculations and are not reported here.

The expectation that these low levels of molecular orbital theory should predict such subtle changes in the potential energy surface is perhaps too high. This seems particularly true for the bromothiophenes where the small basis sets undoubtedly provide only a crude electronic description of the molecules. Larger basis sets incorporating polarization functions are no doubt essential for an adequate electronic description of molecules with such heavy atoms. Despite the small basis sets employed, the parameters obtained from 3-21G split valence computations for the methyl and chloro substituted species lend support to the LM assignment of the substituent induced shift in the aryl CH stretching maxima.

Although anharmonicity is modified upon substitution, perhaps not unexpectedly, frequencies are more sensitive to substitution. This sensitivity is supported by the split valence *ab initio* isolated oscillator frequencies. The magnitude of the substituent effect on the diagonal quadratic aryl CH stretching force constants can largely account for the shift in the overtone maxima. This corroborates the experimental parameterization of substituent induced shifts in the aryl CH stretching transitions in both benzene and aromatic heterocyclic ring systems.

### iii.) Bondlength-Frequency Correlations

Relationships between the equilibrium length of a bond and its stretching frequency have been proposed many times in the literature<sup>141-148</sup>. The central concept behind these proposals has been the idea of bond strength. The stronger an oscillator is bound, the higher its resonant oscillation frequency. Intuitively, the stronger the oscillator pairs are bound, the shorter the separation between the point masses. An inverse relation between stretching frequency and bondlength is intuitively appealing.

Perhaps the best known empirical relation derived for diatomics is Badger's rule<sup>141</sup>. This rule along with other variants have the general form

$$f_e \left( q_e - d_{ij} \right)^n = C_{ij} \quad (9.5)$$

where  $f_e$  and  $q_e$  are the harmonic force constant and equilibrium bondlength respectively. For Badger's rule  $n=3$ , but in other proposed relations<sup>142-146</sup> it ranges from 2 to 6. The terms  $d_{ij}$  and  $C_{ij}$  are

constants which depend on the constituent atoms of the diatomic. Other empirical formulas<sup>147</sup> have utilized relationships of the form

$$q_e \omega_e = \text{constant} \quad (9.6)$$

Relations based on equations of the form of 9.5 and 9.6 have been found to be applicable in a crude sense. Other more useful or universal relationships have been sought.

Over the past fifteen years McKean and coworkers<sup>99,125</sup> have developed and extensively tested empirical expressions correlating shifts in the isolated fundamental XH stretching transitions of polyatomic molecules with the dissociation energy and the equilibrium length of the XH bond. In their approach, all but a single specific proton are replaced by deuterium. This effectively isolates the single XH stretching mode from the remaining vibrational degrees of freedom of the molecule. The correlation between bondlength difference and the shift in the fundamental band is remarkably good. Using the CH bondlength of benzene as a reference, an expression relating CH bondlength,  $r_{CH}$ , and the isolated CH

stretching frequency has been established.

$$r_{\text{CH}} (\text{\AA}) = 1.3982 - 0.0001023 \omega_{\text{CH}}^{\text{iso}} \quad (9.7)$$

Hayward and Henry<sup>22</sup> reported a good correlation between the isolated stretching frequency and the energies of the  $\Delta\nu_{\text{CH}} = 5$  stretching overtone transitions of a number of hydrocarbons. More extensive studies by Mizugai and Katayama<sup>126</sup> led to a bondlength - overtone frequency correlation for the  $\Delta\nu_{\text{CH}} = 6$  region. Wong and Moore<sup>124</sup> correlated gas phase  $\Delta\nu_{\text{CH}} = 6$  overtone positions with isolated CH stretching frequencies and bondlengths obtained from 4-31G split-valence basis set *ab initio* molecular orbital calculations.

$$r_{\text{CH}}^0 (4\text{-}31\text{G}) (\text{\AA}) = (1.319 \pm 0.022) - (1.426 \pm 0.134) \times 10^{-5} \nu_{\Delta\nu=6} \quad (9.8)$$

Incorporating the results of McKean, Wong and Moore, and Mizugai and

Katayama, Gough and Henry<sup>132-134</sup> developed a general CH bondlength - frequency correlation equation.

$$r_{\text{CH}}^{\text{LM}} (\text{\AA}) = 1.084 - \left( \frac{\Delta\nu}{11\nu} \right) \times (0.001) \quad (9.9)$$

This equation states that a shift in the position of the CH stretching fundamental or overtone transition by  $11\nu \text{ cm}^{-1}$ , where  $\nu$  is the total quanta of CH stretch, corresponds to a bondlength change of  $0.001\text{\AA}$ . Again in equation 9.9 the CH bondlength of benzene ( $1.084\text{\AA}$ ) is used as a reference and shifts in fundamental and overtone positions are measured relative to the position of the corresponding transition of benzene ( $\Delta\nu \text{ cm}^{-1}$ ). *Ab initio* calculations in conjunction with gas and liquid phase overtone spectroscopic studies of a large number of substituted benzenes support the general correlation equation<sup>131</sup> of Gough and Henry.

The correlation equation of McKean's for the fundamental CH stretching region of selectively deuterated molecules along with the related equations developed for the overtone regions raise questions

of both basic and practical interest. The first aspect of interest concerns the relationship between the anharmonic oscillator model of the CH stretching mode and the correlations. The two parameter anharmonic oscillator equation (1.9) typically provides a good fit to the CH stretching fundamental-overtone progression. In establishing the validity of the general correlation equation (9.9), Gough cautioned that the magnitudes of the LM anharmonicities of the oscillators would have to be comparable<sup>131</sup> for the correlation to hold. In fact, the correlation equation which at a given level of CH stretch excitation relates a difference in the maxima of CH stretching transitions to a difference in CH bondlength, requires that the two anharmonic oscillator parameters not be independent. The quartic expansion of the Morse oscillator (equations 9.3 and 9.4) offers a means of investigating the relationship between frequency and anharmonicity. Both the frequency and anharmonicity parameters contain a contribution from the diagonal quadratic force constant. In the frequency term the contribution is in the numerator while it is in the denominator in the expression for the anharmonicity. In the previous section, substituent induced shifts in overtone maxima were largely attributed to changes in the diagonal

quadratic force constant. If the higher order diagonal force constants are fixed, an increase in oscillator frequency results in a decrease in the anharmonicity. This anharmonicity mismatch between high and low frequency XH oscillators results in an increasing separation between the overtone transitions associated with the respective oscillators at increasing levels of XH stretch excitation. This trend is commonly observed in CH stretching progressions and is imbedded in the shift-bondlength correlation equations. This is particularly evident in equation (9.9). The point to note is that implicitly contained within the correlation equations is a specific relationship between the frequency and anharmonicity. The equations can only be expected to hold in circumstances where the particular relationship is closely satisfied. The stated accuracy and universality of the correlation equations should be viewed more cautiously. The study of the aryl CH stretching overtone progressions of the aromatic heterocycles offers a good counter example of the generality of the established frequency-bondlength correlations.

From the assigned zero order LM parameters the applicability of a particular correlation equation can be tested. The

anharmonicities and frequencies of the aromatic heterocycles do not nicely follow the constraints imposed by the general overtone-bondlength correlation equation. Theoretical calculations support the anomalous frequency - anharmonicity relation particularly for the furans. Unlike the substituted benzenes, quantitatively the general CH bondlength - frequency correlations fail for the aromatic heterocycles. Qualitatively however, many of the general features of the overtone spectra of the furans and thiophenes can still be understood in terms of relative CH bondlength differences. For example, the oscillators adjacent to the ring heteroatom are shorter than the oscillators at the three and four positions on the ring<sup>149-152</sup>. *Ab initio* bondlengths of some furans and thiophenes are reported in tables 9.8 and 9.9. According to an inverse frequency-bondlength relation, at a given level of excitation, the overtone associated with the 2,5 oscillators should be at higher energy than the overtone of the 3,4 oscillators. This is indeed observed. A comparison between the CH stretching frequencies of furan, pyrrole and thiophene shows the inverse frequency-bondlength trend. Substituent induced frequency shifts also follow predicted bondlength trends. Chlorine substitution is predicted to shorten the CH bond(s) adjacent to the

**TABLE 9.8**

Predicted Aryl CH Bondlengths of Selected Thiophenes

(Å)	Basis Sets			
	STO-3G	3-21G	6-31G	6-31G*
thiophene				
C(2)H(2)	1.0789	1.0652	1.0664	1.0709
C(3)H(3)	1.0803	1.0692	1.0707	1.0735
3,4 dibromo				
C(2)H(2)	1.0794	1.0714	-	-
2,5 dibromo				
C(3)H(3)	1.0806	1.0886	-	-
2,5 dichloro				
C(3)H(3)	1.0807	1.0675	1.0691	-
2,5 dimethyl				
C(3)H(3)	1.0801	1.0704	1.0720	-

TABLE 9.9

Predicted Aryl CH Bondlengths of Selected Furans

(Å)	Basis Sets			
	STO-3G	3-21G	6-31G	6-31G*
furan				
C(2)H(2)	1.0820	1.0618	1.0628	1.0681
C(3)H(3)	1.0774	1.0647	1.0664	1.0702
2,5 dimethyl				
C(3)H(3)	1.0769	1.0652	1.0673	-
2 methyl				
C(3)H(3)	1.0768	1.0618	1.0668	-
C(4)H(4)	1.0774	1.0649	1.0667	-
C(5)H(5)	1.0818	1.0649	1.0630	-

substitution site thus shifting the associated overtone transition(s) to higher energy. A methyl substituent lengthens the adjacent aryl CH oscillators and hence shifts the overtones to lower energy. Again these trends are observed in the spectra. Thus although the established bondlength-frequency correlations are of little use at a quantitative level, qualitatively the concept of a frequency-bondlength relationship is still a very useful predictive tool.

The source of the breakdown of the correlation equations for the aryl CH bondlengths of the aromatic heterocycles lies in the strange behaviour of the aryl CH stretching overtone progressions. Rather than the overtones associated with the nonequivalent oscillators dramatically becoming increasingly resolved at higher levels of excitation, the resolution increases only moderately. This is apparent in the slopes of the Birge - Spomer plots for furan and thiophene (see Figures 9.6 and 9.13). In the zero order LM assignment, the behaviour of the progressions is displayed in the zero order LM parameters. The anharmonicities of the aryl CH oscillators of the aromatic heterocycles do not display the typical inverse frequency dependence observed for most other CH oscillators. To ensure correct assignment of the progressions, the

spectra of the parent molecule were compared to the spectra of symmetrically disubstituted molecules. As further evidence of a correct assignment and LM parameterization, theoretical *ab initio* isolated oscillator parameters were calculated. Their agreement with LM parameters strongly suggest that the relative magnitudes of the aryl CH stretching frequencies and anharmonicities of the aromatic heterocycles are in part responsible for the behaviour of the overtone progressions. Are there other contributing factors? In the next Chapter, other factors influencing the aryl overtone progressions of the aromatic heterocycles are explored. The role of these factors on the LM dynamics is stressed as well as their contribution to the breakdown of bondlength - frequency correlation equations.

## CHAPTER 10 : LOCAL MODE DYNAMICS OF THE AROMATIC HETEROCYCLES

### i.) Deviations From Zero Order LM Predictions

Overall, the vibrational overtone spectra of the 5-member aromatic heterocycles are reasonably well described by the zero order LM model. However, there are some notable exceptions and some unusual behaviour. The most unusual behaviour cited in the previous Chapter was the tendency for the resolved aryl overtone progressions to become less distinct at higher energies. This is in contrast to the behaviour found in a wide variety of substituted benzenes. With support from theoretical calculations, it was argued that the behaviour observed in the 5-member aromatic heterocycles was a result of the higher frequency oscillators having higher than normal anharmonicities relative to the lower frequency oscillators. Typically, anharmonicities scale inversely with oscillator frequency. It was also argued that due to the opposite frequency - anharmonicity trend found in the aromatic heterocycles, the general

bondlength - frequency correlation equation could not be quantitatively applied to the 5-member aromatic heterocycles. Implicit in the correlation equations is a relationship between the frequency and anharmonicity of the CH oscillator.

For the most part, the unusual trend in the aryl CH stretching overtone progressions of the aromatic heterocycles can be rationalized in terms of the behaviour of the zero order LM parameters. However there are dramatic perturbations along these progressions which cannot be explained with simple zero order ideas. The  $\Delta\nu_{\text{CH}} = 4$  region of furan (see Figure 9.8) is one such region. At  $\Delta\nu_{\text{CH}} = 4$ , there is a coalescence of the two peak structure into a single peak. The two peak pattern re-emerges in the  $\Delta\nu_{\text{CH}} = 5,6$  (see Figures 9.10 and 9.11) gas phase spectra but is only partially resolved in the liquid phase (see Figure 9.9). Such a coalescence and reemergence can be rationalized in a zero order description if the overtone progressions associated with the two sets of nonequivalent oscillators cross at some point. The unusual trend in anharmonicities in the heterocycles are suggestive of such a crossing. However, the comparison of the overtone progressions of the parent molecule and symmetrically disubstituted species

indicate that such a crossing does not occur. From  $\Delta\nu_{\text{CH}} = 1-6$ , the fundamental or overtone transition associated with the oscillators adjacent to the heteratom appear at higher energy than the corresponding transition associated with the oscillators at the 3 and 4 positions on the ring. The quality of the Birge-Sponer fits to the aryl overtone progressions also suggests that crossing does not occur. If crossing can be eliminated, such a coalescence followed by re-emergence of the overtone pattern can not be readily explained by the simple LM model.

The aryl overtone progressions of thiophene display some dramatic non-zero order features. At both  $\Delta\nu_{\text{CH}} = 3$  and 5 the familiar two-peak structure is abruptly perturbed. There are three dominant features in the liquid phase  $\Delta\nu_{\text{CH}} = 3$  spectrum of thiophene (Figure 10.1). Several shoulders at low energy are also apparent. In the gas phase, features are more clearly resolved (Figure 10.2). The intensity of the central dominant feature drops relative to the higher and lower energy main features. Residual splittings in the high energy and central features are resolved in the gas phase. The gas phase spectrum at  $\Delta\nu_{\text{CH}} = 5$  (Figure 10.3) has a similar appearance to the  $\Delta\nu_{\text{CH}} = 3$  spectra. Here again three peaks dominate the spectrum;

a low energy peak and a higher energy doublet. Like the coalescence of the overtone progressions of furan at  $\Delta\nu_{\text{CH}} = 4$ , these abrupt perturbations of the overtone progressions of thiophene cannot be explained by zero order LM ideas.

**FIGURE 10.1**

Liquid phase overtone absorption spectrum of thiophene in the  $\Delta\nu_{\text{CH}} = 3$  region. A sample cell of pathlength 5 cm was used.

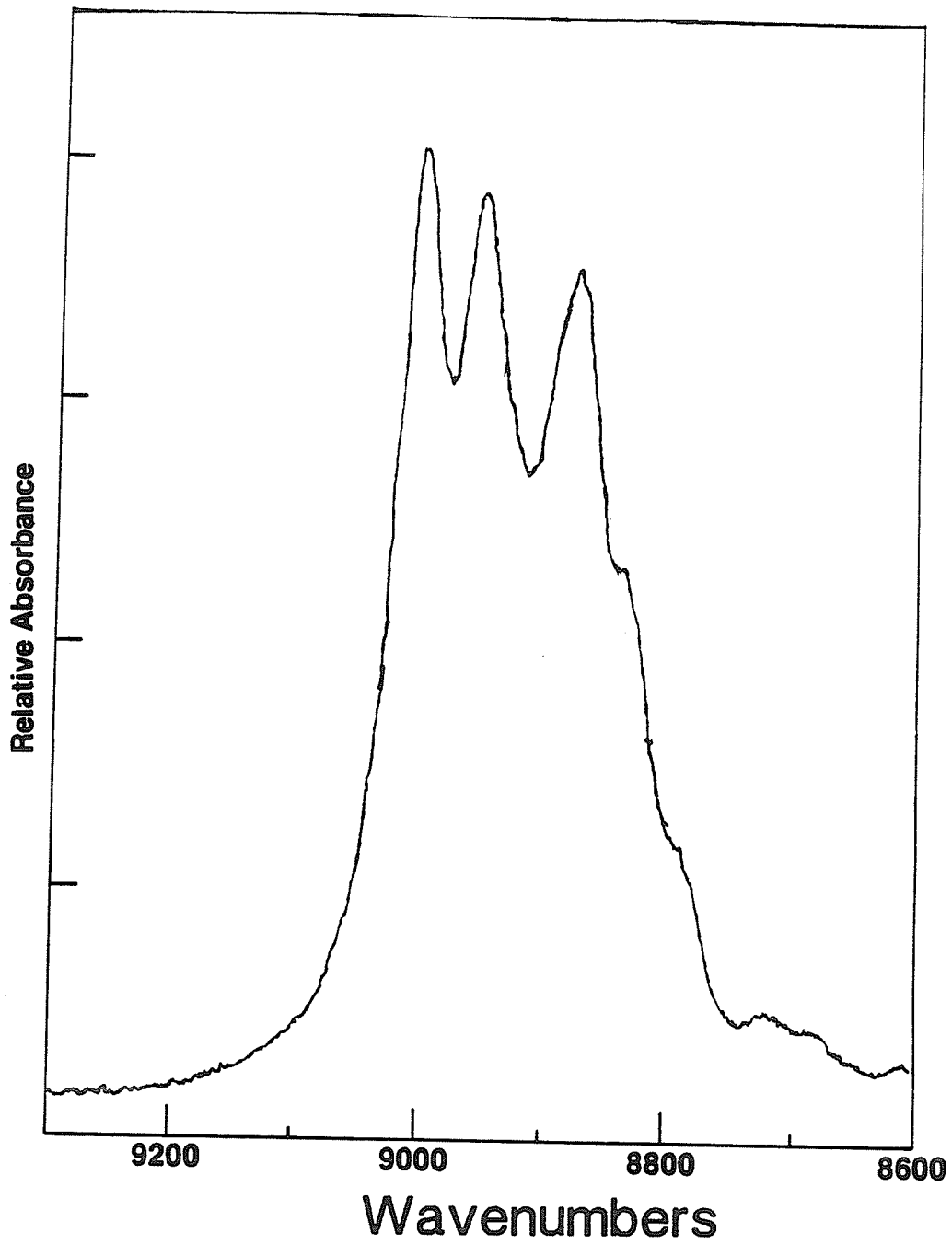


**FIGURE 10.2**

Gas phase overtone spectrum of thiophene in the  $\Delta\nu_{\text{CH}} = 3$  region. The thiophene spectrum was measured at a pressure of 60 Torr with a 11.25 m pathlength cell.

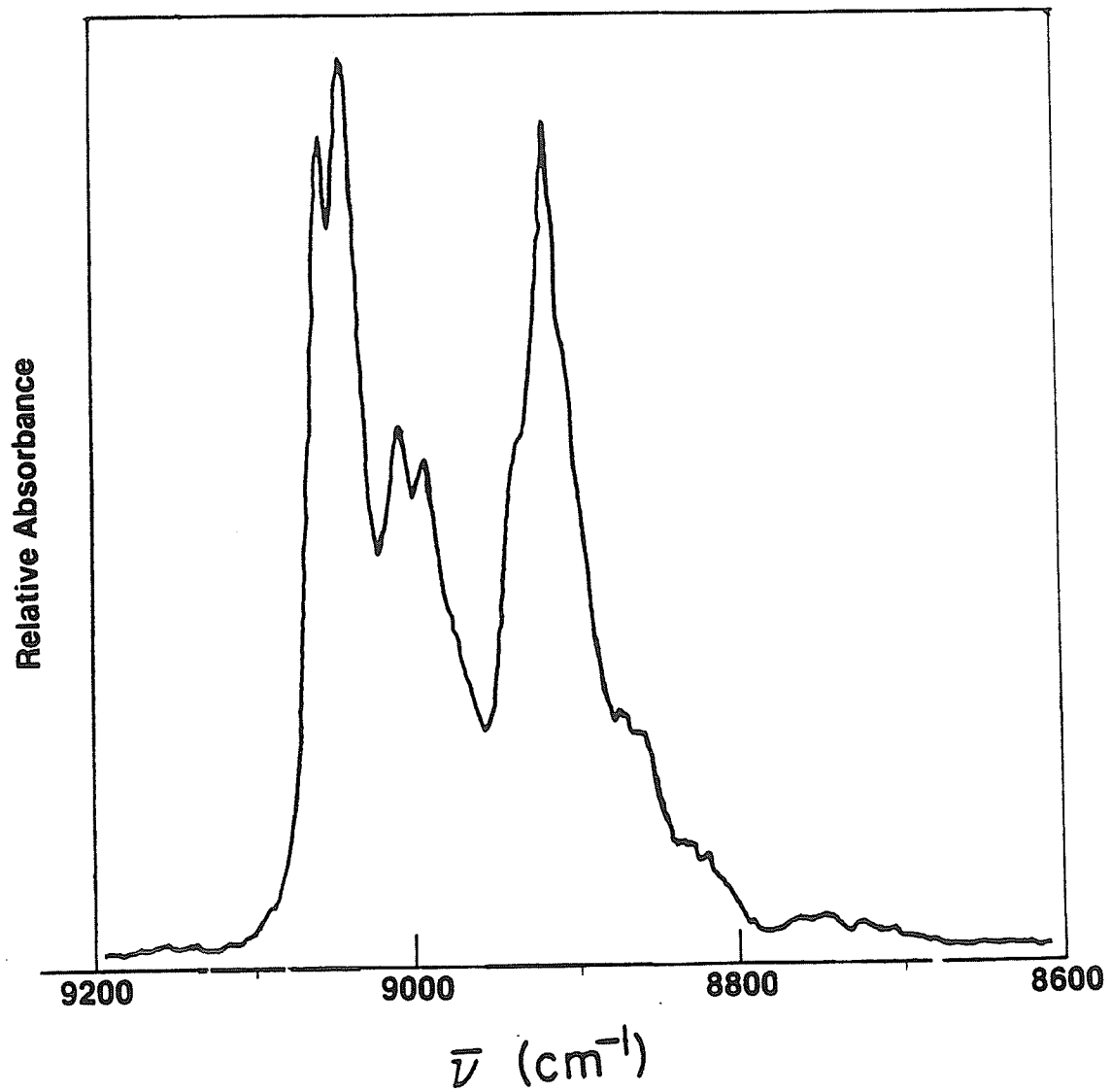
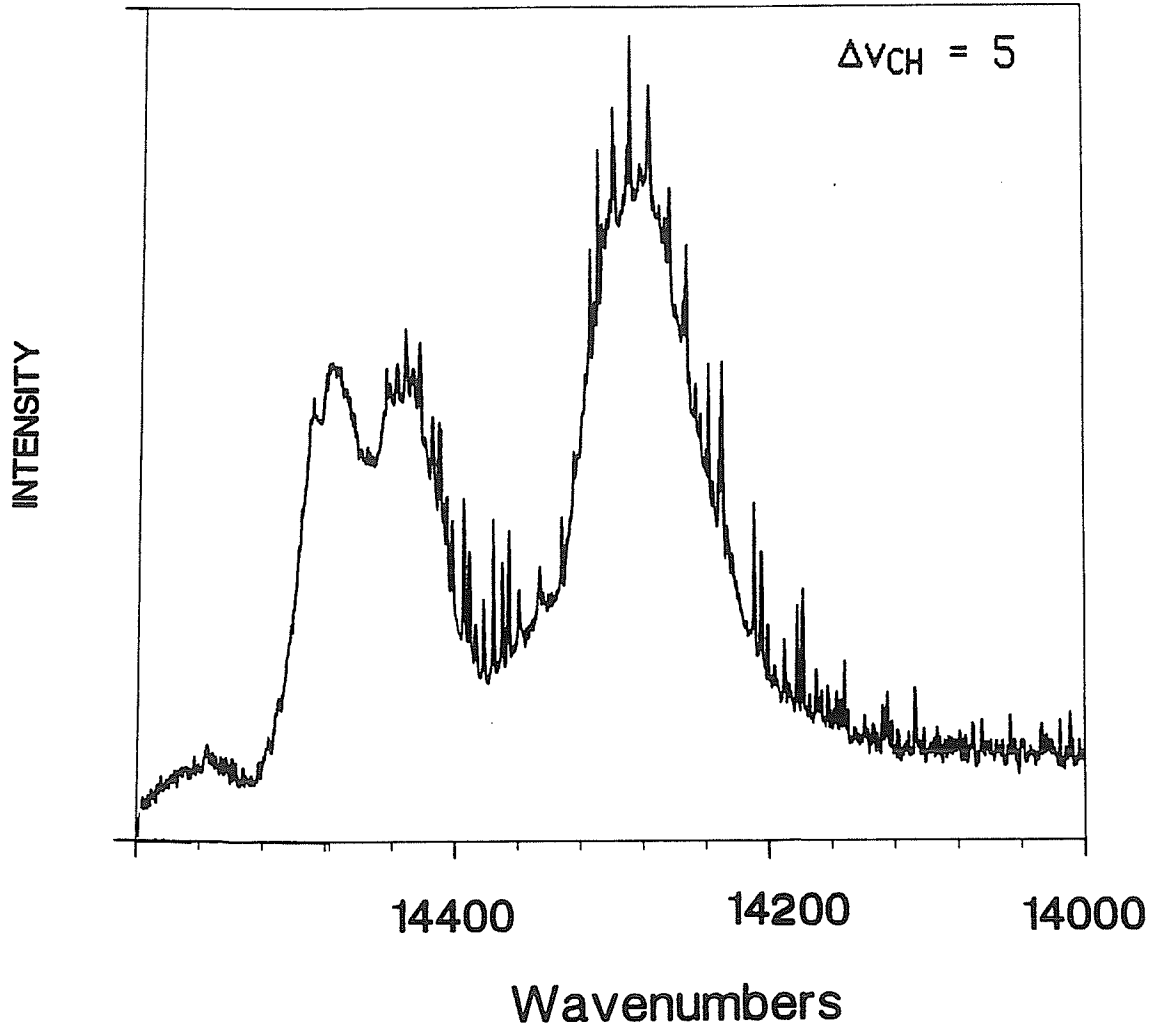


**FIGURE 10.3**

Gas phase photoacoustic overtone spectrum of thiophene in the  $\Delta\nu_{CH} = 5$  region. The thiophene spectrum was measured at a pressure of 60 Torr with a 10 cm pathlength cell.



## ii.) Fermi Resonance and Internal Vibrational Energy Redistribution

The harmonic coupling extension to the zero order local mode model was introduced in section iv of Chapter 1. The model extension considered only the quadratic interactions, approximated in terms of harmonic oscillator ladder operators, between the XH stretching modes . The quadratic couplings between XH stretching and other modes were ignored on the basis of a large energy mismatch between the states coupled by the ladder operators. In polyatomic systems, vibrational state densities increase enormously with increasing energy. States built on various modes with favourable energy matches with the XH stretching states become the norm rather than the exception at the high overtone regions. In the harmonic oscillator ladder operator formalism, these states couple to XH overtone states through higher order anharmonic coupling terms. However, weakly coupled near resonant states can interact strongly giving rise to large spectral perturbations. Interactions of this type were first recognized by Fermi<sup>153</sup> and hence they are called

Fermi resonant interactions. In addition to the spectral manifestations of Fermi resonances, Fermi resonant interactions are also believed to play a central role in the dynamics of internal vibrational energy redistribution (IVR) in polyatomic systems.

Understanding the dynamics of highly vibrationally excited states of polyatomic systems is an extremely complicated problem. As a first step to understanding the process, the interplay between XH stretching motion and the other vibrational and rotational degrees of freedom of the molecule must be addressed. Fermi resonance type interactions are considered to be a crucial component in overtone dynamics. In the mid-infrared region vibrational state densities are sparse. However, at the high energy overtone regions, the XH stretching states are imbedded in a quasi-continuum of vibrational states. Zero order LM overtone states,  $|\phi_{XH}\rangle$ , carry the oscillator strength from the ground state. If totally decoupled,  $|\phi_{XH}\rangle$  is an eigenstate and the spectrum would consist of a single line at the excitation energy of this state. If however  $|\phi_{XH}\rangle$  is weakly coupled to the quasi-continuum of nearby states,  $|\phi_{XH}\rangle$  is not an eigenstate but instead made up of many molecular eigenstates,  $|\psi_i\rangle$ , each

carrying some oscillator strength from the ground state.

Polyatomic molecules display broad (30-200  $\text{cm}^{-1}$ ) overtone linewidths. The peak maxima of an overtone progression are well described by the anharmonic oscillator equation (1.9). Both the overtone linewidths and the behaviour of the overtone maxima can be understood in terms of Fermi resonant type arguments. Coupling of the overtone state to the quasi-continuum of surrounding states spreads the probability of being in a "bright" overtone state over eigenstates spanning a large energy range. The spectrum associated with the LM overtone state would consist of a dense set of lines. Homogeneous and inhomogeneous broadening contributions wash-out the dense line structure to give a broad envelop in the overtone region.

In the typical two-state Fermi resonance observed in the low vibrational state density regime, the resonance interaction is characterized by both a redistribution of transition intensities and energy shifts of the zero order states. Even at the low overtone regions, the zero order LM XH stretching overtone state is embedded in a dense set of near resonant states. A very large number of interactions arise from the weak coupling of the zero order LM state

to the quasi-continuum. The overtone is coupled to states over a wide energy range both above and below the energy of the overtone state. The distribution of the coupled states is such that there is no preferential direction of energy shift and thus the overtone peak maxima are not significantly shifted from their expected positions. From this interpretation, overtone peak maxima are expected to follow the anharmonic oscillator equation despite the fact that they are significantly coupled to surrounding states. This interpretation also suggests that the overtone features and their linewidths should be relatively insensitive to small shifts in energy. We shall see that this is not the case and more restrictive Fermi resonance coupling schemes must be applied to understand these subtleties.

For some time now there has been a debate over the relative importance of homogeneous and inhomogeneous contributions to overtone linewidths<sup>154-166</sup>. Very rapid IVR rates accompanying overtone excitation can account for the large overtone linewidths. However some authors have stressed inhomogeneous contributions, hot-band structure in particular<sup>166</sup>, as an important source of overtone linewidths in polyatomic systems. In order to distinguish between homogeneous and inhomogeneous broadening, the spectra of

molecules with low internal temperatures are required. Supersonic molecular beam expansions generate internally very cold (vibrational temperatures of 10K are not unusual), isolated gas phase molecules. Despite the recent advances in supersonic molecular beam expansion methodologies, such techniques are very difficult to apply in the study of highly vibrationally excited states due to weakness of the overtone transitions. A few limited examples exist. The jet-cooled vibrational overtone spectra of water<sup>167</sup>, tetra-methyldioxetane (TMD)<sup>168</sup>, hydrogen peroxide<sup>169</sup>, t-butylperoxide<sup>170</sup>, and benzene<sup>171</sup> have been reported. In addition, low temperature photoacoustic overtone absorption spectra of methane, deuterio-methanes, ethylene, ethane, propyne, propane, cyclopropane, dimethyl ether, and isobutane at temperatures between 77 and 189 K have been reported<sup>172</sup>. The small molecular systems, water, methane, and hydrogen peroxide show dramatic cooling effects. The larger molecules show only modest changes in the overtone regions upon cooling. However the recent work by Page, Shen, and Lee<sup>171</sup> reveal dramatic cooling effects in the jet-cooled spectra fundamental and low overtone regions ( $\Delta\nu_{\text{CH}} \leq 3$ ) of benzene. They resolve a number of lines with relatively narrow widths (1 to 3  $\text{cm}^{-1}$ ) in the

fundamental and low overtone regions as opposed to a single homogeneously broadened overtone transition. Unfortunately with their technique, Page et al were unable to observe the weaker, higher overtone regions of benzene. In an earlier study of the  $\Delta\nu_{\text{CH}} = 5$  spectra of crystalline benzene and durene at 1.8 K, Perry and Zewail<sup>173</sup> were unable to observe any significant decrease in the overtone linewidths due to cooling.

The experimental results suggest two limits for IVR. The limits are often termed the "small" and "large" molecule limit. The "small" molecule limit is characterized by a sparse vibrational state density whereas the "large" molecule limit concerns the case where the state density approaches a continuum. It should be noted that despite the names of the limits, molecular size alone does not determine which is the applicable limit. In fact a single molecule could obey both limits. At low enough energy, the molecule may behave in the "small" molecule limit whereas at higher energies the dynamics may be better described by the "large" molecule limit. For benzene, it has been suggested<sup>50,171</sup> that transition between the two limits lies between  $\Delta\nu_{\text{CH}} = 3$  and 4.

To understand overtone dynamics in the "large" molecule limit,

Sage and Jortner<sup>154</sup> proposed a statistical model. In the statistical model, the "bright" LM overtone state weakly couples to the full density of surrounding vibrational states. The intramolecular relaxation process is based on the conventional Fermi golden rule<sup>174</sup> formulation,

$$\Gamma = 2\pi |V_c|^2 \rho \quad (10.1)$$

Here  $\Gamma$  is the IVR rate,  $|V_c|$  is the average coupling matrix element, and  $\rho$  is the vibrational state density. Equation 10.1 predicts that the IVR rate should increase along an XH overtone progression due to the rapid increase of  $\rho$  with XH stretching quantum number,  $\nu_{XH}$ . Also since the average coupling matrix element between LM overtone states and other zero order molecular states is relatively independent of the molecular system,  $\Gamma$  should increase with the size of the molecule. The high vibrational state densities encountered in the XH stretching overtone regions play an important role but not a singular role in the IVR process. The linewidths of CH stretching

fundamental - overtone transitions generally increase from  $\Delta v = 1$  to 3. Also, the overtone linewidths of small tri and tetra-atomic systems are much narrower than larger molecules. However, overall the overtone linewidths do not scale directly with state densities. At  $\Delta v_{CH} \geq 3$  overtone linewidths do not necessarily increase with increasing  $\Delta v_{CH}$ . This was specifically investigated in benzene<sup>50</sup> and neopentane<sup>175</sup> and is observed in a number of other systems. Linewidths also do not necessarily scale with the size of the molecule. For example, the overtone linewidths observed for neopentane are significantly narrower than those of benzene<sup>175</sup>. The narrower neopentane linewidths arise despite the fact that at any given energy the density of states in neopentane is considerably greater than for benzene. Again this same phenomenon has been observed in a number of systems.

An early coupling model introduced by Heller and Mukamel<sup>156a</sup> considered the interoscillator XH stretch-stretch interactions as the dominant dynamical couplings. The model cannot successfully account for linewidth trends in the high overtone regions. However, it is now well established that XH stretch - stretch couplings are largely responsible for the energy shifts and intensity redistribution

observed in the XH stretching fundamental and low overtone regions. In the LM coupling model, the important overtone couplings are to combination states in which only one quantum of XH stretch is redistributed (  $|v,0,0,\dots\rangle \rightarrow |v-1,1,0,\dots\rangle$  ). Restricting the couplings to this form, is equivalent to the intramanifold harmonic coupling extension discussed in section iii of Chapter 1. The interoscillator couplings are clearly important. The spectroscopy emphatically tells us of their importance particularly in the lower energy regimes ("small" molecule limit). However the dynamics of overtone excitation cannot be adequately explained by these interstate couplings alone. There are two rather obvious shortcomings of such a model. The anharmonicity defect of XH oscillators increases the energy separation between the overtone and the important combination states at high quanta of XH stretch. If the LM overtone - combination couplings dominated the dynamics, overtone linewidths would be expected to decrease with increasing  $v_{XH}$ . The second serious shortcoming concerns magnitudes of interoscillator couplings. Aromatic CH oscillators are separated by one carbon linkage from each other. Therefore the interoscillator coupling is weak and hence coupling splittings are not typically

resolved in the fundamental or low overtone regions. The oscillators in a methyl group share a central carbon atom and are significantly coupled. The spectroscopic features arising from the interoscillator coupling in a methyl group are discussed at some length in Part D of this thesis. The low overtone features of neopentane are indicative of significant interoscillator coupling. However, the linewidths of neopentane are much narrower than those of benzene, despite the stronger interoscillator couplings.

The statistical coupling scheme and harmonic interoscillator coupling model represent two extremes. The statistical model considers all interstate couplings on an equal footing while the latter model considers the interoscillator interactions as the dominant interstate couplings and ignores the importance of the remaining couplings. In attempting to understand the overtone linewidths of benzene, Reinhardt, Sibert, and Hynes<sup>160</sup> (RSH) introduced a more structured interstate coupling model. Like the model of Heller and Mukamel, certain states were singled out to preferentially couple to the overtone states. These states were in turn coupled to other states and so on. Thus in the RSH description there is a hierarchy of states coupled to the overtone states. The

initial tier of coupled states have often been called the "doorway" states. In the RSH model, the XH-stretching energy flows into the bath of surrounding vibrational states through specific channels or doorways. In these types of descriptions, the overtone lifetime depends on the overall vibrational state densities as well as the zero order energies and overtone coupling matrix elements of the doorway states.

Extending a coupling scheme suggested by Stannard and Gelbart<sup>157</sup>, RSH identified the CCH in-plane deformation and to some extent the CC stretch as the important doorway states in the description of benzene CH stretching overtone dynamics. Tarr<sup>176</sup> and Tarr and Henry<sup>175,177</sup> applied these ideas to the overtone linewidth data of neopentane. Like those of benzene and deuterio-benzene, the linewidths of neopentane and its deuterated derivatives do not scale with vibrational CH stretch quantum number. Comparison between undeuterated and deuterated systems shows that the overtone linewidths of neopentane and benzene do not scale with state densities. Like benzene, the neopentane linewidths could be rationalized on the basis of interstate couplings between the methyl CH stretching overtone  $|v,0,0\rangle$  and the "doorway" combination states

of the form  $| \nu-1,0,0 \rangle | 2 \nu_N \rangle$ . In the neopentane case the Fermi resonance interaction involved the CH stretching overtone states and combinations involving the CH<sub>3</sub> deformational overtone. This explanation could also account for the surprising linewidth difference between neopentane and benzene. The combinations built on the in-plane CH deformations of benzene are more closely resonant with the CH stretching overtones through the regions  $\Delta\nu_{CH} = 3 - 6$  than the corresponding CH<sub>3</sub> deformation combinations in neopentane. The better resonance match between overtone and "door-way" states in benzene was cited as the reason for the wider benzene overtone linewidths.

The aryl CH stretching overtone linewidths of the aromatic heterocycles are difficult to rationalize on statistical grounds: The overtone widths do not scale with CH stretching quantum number, the linewidths are relatively insensitive to substitution, and the linewidths of the furans are consistently wider than the corresponding transitions in the thiophenes. Based on the success of the RSH Fermi resonance interpretation of the overtone linewidths of benzene and neopentane, it seems worthwhile to apply these ideas to the aromatic heterocycles.

In the RSH Fermi resonance interpretation overtone broadening arises from the near resonance interaction between the zero order overtone and "door-way" state. In benzene and neopentane the important interstate couplings were between zero order states of the form  $|v,0,0\rangle \longleftrightarrow |v-1,0,0\rangle |2v_N\rangle$  where  $|2v_N\rangle$  is the first overtone of a mid-frequency mode. The variation in overtone linewidth along the overtone progression is interpreted as being dictated by the quality of the resonance match between the overtone and the "door-way" states in that region. The various "door-way" states "tune-in" and "tune-out" of resonance along the overtone progression. The harmonic frequencies of the mid-frequency modes of furan<sup>117</sup> and thiophene<sup>118</sup> are reproduced in table 10.1. The prospective "door-way" states of the form  $|v-1,0,0\rangle |2v_N\rangle$  in the  $\Delta\nu_{CH} = 1 - 6$  region for the aromatic heterocycles involve the overtone of the ring stretching and in-plane CH deformational modes. The best resonance match involving these modes occurs at  $\Delta\nu_{CH} = 4$  in furan. Ignoring the anharmonicity of the  $\nu_4$  ring stretching mode, the  $|3,0\rangle_{2,5} |2\nu_4\rangle$  and  $|3,0\rangle_{3,4} |2\nu_4\rangle$  combinations are only 2 and 10  $\text{cm}^{-1}$  higher in energy than the respective zero order overtone

**TABLE 10.1**

Fundamental Vibrational Frequencies of the mid-Frequency  
 $A_1$  and  $B_1$  Modes of Furan<sup>117</sup> and Thiophene<sup>118</sup>.

Mode	Approximate Description	$C_{2v}$	Furan	Thiophene
$\nu_5$	Ring stretch	$A_1$	1491	1408
$\nu_4$	Ring stretch	$A_1$	1384	1360
$\nu_6$	CH in-plane deformation	$A_1$	1140	1081
$\nu_7$	CH in-plane deformation	$A_1$	1066	1033
$\nu_3$	Ring stretch	$A_1$	995	833
$\nu_8$	Ring in-plane deformation	$A_1$	871	606
$\nu_{14}$	Ring stretch	$B_1$	1556	1506
$\nu_{15}$	CH in-plane deformation	$B_1$	1267	1250
$\nu_{16}$	CH in-plane deformation	$B_1$	1180	1081
$\nu_{17}$	Ring (def + stretch)	$B_1$	1040	871
$\nu_{18}$	In-plane ring deformation	$B_1$	873	750

state. The anharmonicity of the  $\nu_4$  mode would tend to improve the resonance match. In the RSH Fermi resonance broadening model, the excellent resonance match between the  $\Delta\nu_{\text{CH}} = 4$  overtones and the "door-way" states could account for the coalescence of the furan overtone progressions at that region. This would seem to be an encouraging result. However, the model is unsuccessful in predicting the other linewidth trends. The resonance match between prospective "door-way" states and overtones over  $\Delta\nu_{\text{CH}} = 1 - 6$  does not suggest a reason for the difference in overtone linewidths between thiophene and furan. In addition, there is no favourable energy match at  $\Delta\nu_{\text{CH}} = 3$  between prospective "door-way" states and overtone states for thiophene. The best match occurs at  $\Delta\nu_{\text{CH}} = 2$  involving the overtone of the  $\nu_{14}$  ring stretching mode. The next best energy matches, 56 and 77  $\text{cm}^{-1}$ , involve the  $\nu_4$  and  $\nu_5$  ring stretching modes at  $\Delta\nu_{\text{CH}} = 4$  and 5 respectively. The  $\Delta\nu_{\text{CH}} = 3$  and 5 regions of thiophene cannot be readily explained like the coalescence of the  $\Delta\nu_{\text{CH}} = 4$  overtone region of furan. The limited success of the RSH Fermi resonance broadening model is further discussed in the next section. The thiophene overtone regions

provide an intriguing example of the importance of Fermi resonance in the highly excited vibrational states.

### iii.) Tuning Near Resonance Interactions Through Substitution

The tiered coupling scheme of RSH does not suggest reasons for the anomalous features in the  $\Delta\nu_{\text{CH}} = 3$  and 5 overtone regions of thiophene. From the available force fields, no obvious overtone - "doorway" state resonance matches can be found. In fact, the behaviour of thiophene is inconsistent with the RSH interpretation of IVR line broadening. In the line broadening mechanism, the "doorway" state is effectively coupled to the quasicontinuum of nearby states. The "door-way" state character is distributed over the quasicontinuum of states. The bright overtone state couples to the quasicontinuum through the "door-way" state. Such an interpretation is not consistent with the thiophene data. Rather, the abrupt perturbations at  $\Delta\nu_{\text{CH}} = 3$  and 5 in the zero order LM spectral pattern of thiophene are suggestive of the 2:1 Fermi resonant features often found in the low vibrational density of states environment of the mid-infrared region.

A 2:1 Fermi resonance in the infrared region corresponds to a situation where the first overtone of a mode is in near resonance with

the fundamental of another mode. The perturbed splittings between the states and the anomalous intensities caused by these resonances has a characteristic pattern. The Fermi states are said to "repel" each other and the overtone is said to "steal" intensity from the fundamental. The closer the zero order energies of the states, the stronger the effects of the interaction. These effects arise from the strong mixing of the zero order states. In this example, the fundamental carries the oscillator strength while the other Fermi state gains intensity from mixing with the fundamental. Since state mixing is the source of intensity for the interacting state, it cannot be more intense than the fundamental. The state mixing manifests itself in a shifting of levels and a redistribution of transition intensities. Under conditions of strong mixing, zero order state labels lose their meaning. Instead the Fermi resonant states are often dubbed a "Fermi doublet". Although in our discussion of Fermi resonant interactions the states involved will often be referred to by the zero order labels, strong state mixing is acknowledged.

Spectral perturbations with the characteristic Fermi resonance pattern appear at the  $\Delta\nu_{\text{CH}} = 3$  and 5 overtone regions of the thiophene spectrum (see Figures 10.1-10.3). The higher energy of

the two overtone transitions has been associated with the aryl oscillators adjacent to the heteroatom. This overtone state is involved in a Fermi resonance with a nearby state. The Fermi resonance features are very sensitive to the resonance condition. For example, in the gas phase the thiophene  $\Delta\nu_{CH} = 5$  features are perturbed by a near resonance interaction while the liquid phase spectrum displays the usual two-peak structure at that overtone. The small differences in the frequencies and anharmonicities of the interacting modes between the gas and liquid phases are sufficient to "tune" and "de-tune" the resonance interaction. The sensitivity of the overtone features to the resonance condition is very clearly shown in the study of substituted thiophenes.

Figures 10.4 and 10.5 compare the  $\Delta\nu_{CH} = 3$  liquid phase spectra of some symmetrically disubstituted thiophenes. At  $\Delta\nu_{CH} = 2$  and 4, the spectrum of 3,4 dibromothiophene consists of a single peak closely corresponding to the higher energy of the two peaks observed in the parent thiophene spectrum. At  $\Delta\nu_{CH} = 3$  the higher energy thiophene peak appears as a Fermi doublet. At the same overtone, the 3,4 dibromothiophene spectrum appears as a doublet but with a smaller splitting than observed for thiophene. In both the

**FIGURE 10.4**

Liquid phase overtone absorption spectrum of 2,5 and 3,4 dibromothiophene overlaid on the thiophene spectrum in the  $\Delta\nu_{\text{CH}} = 3$  region. A sample cell pathlength of 5 cm was used.

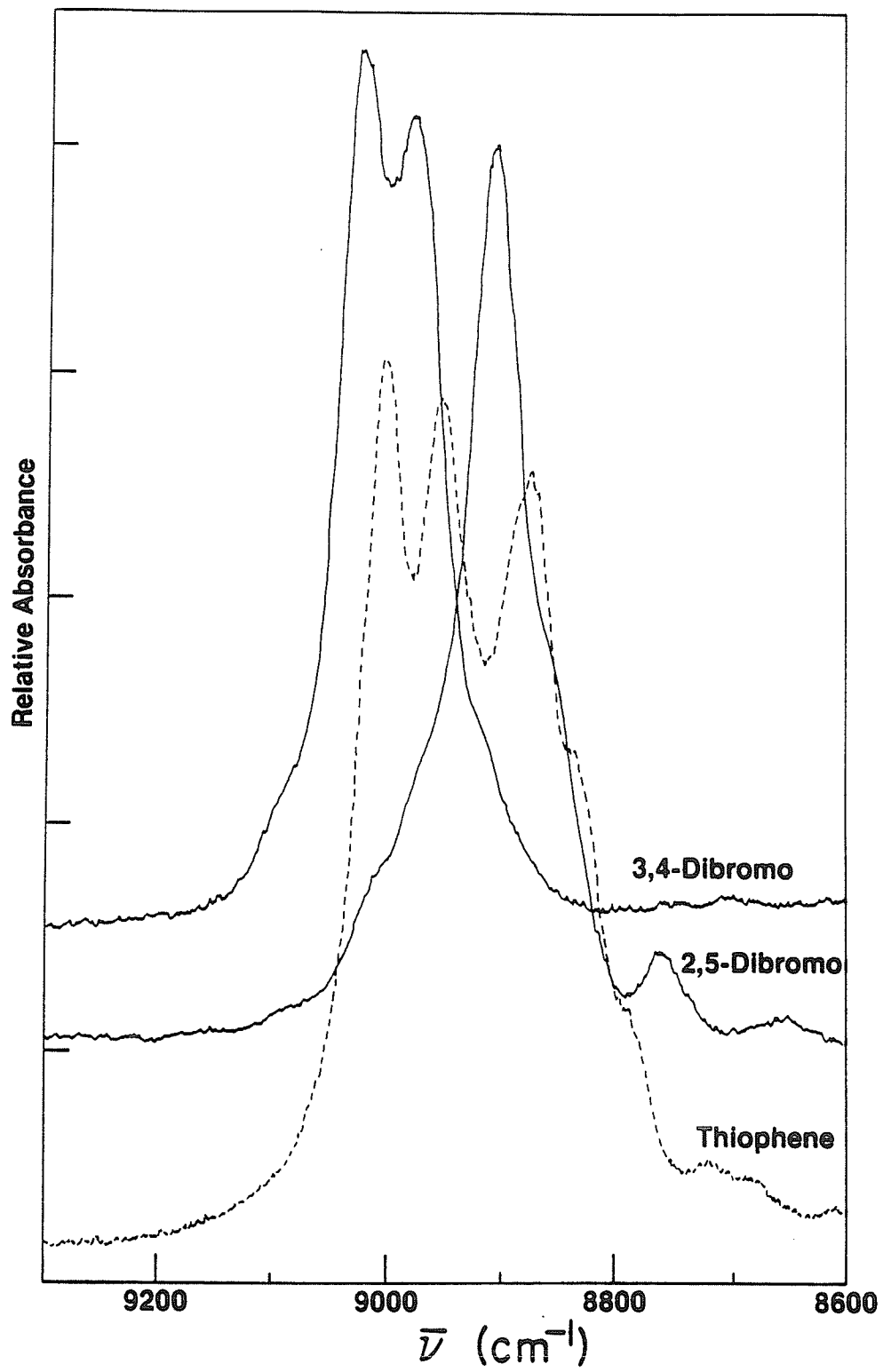
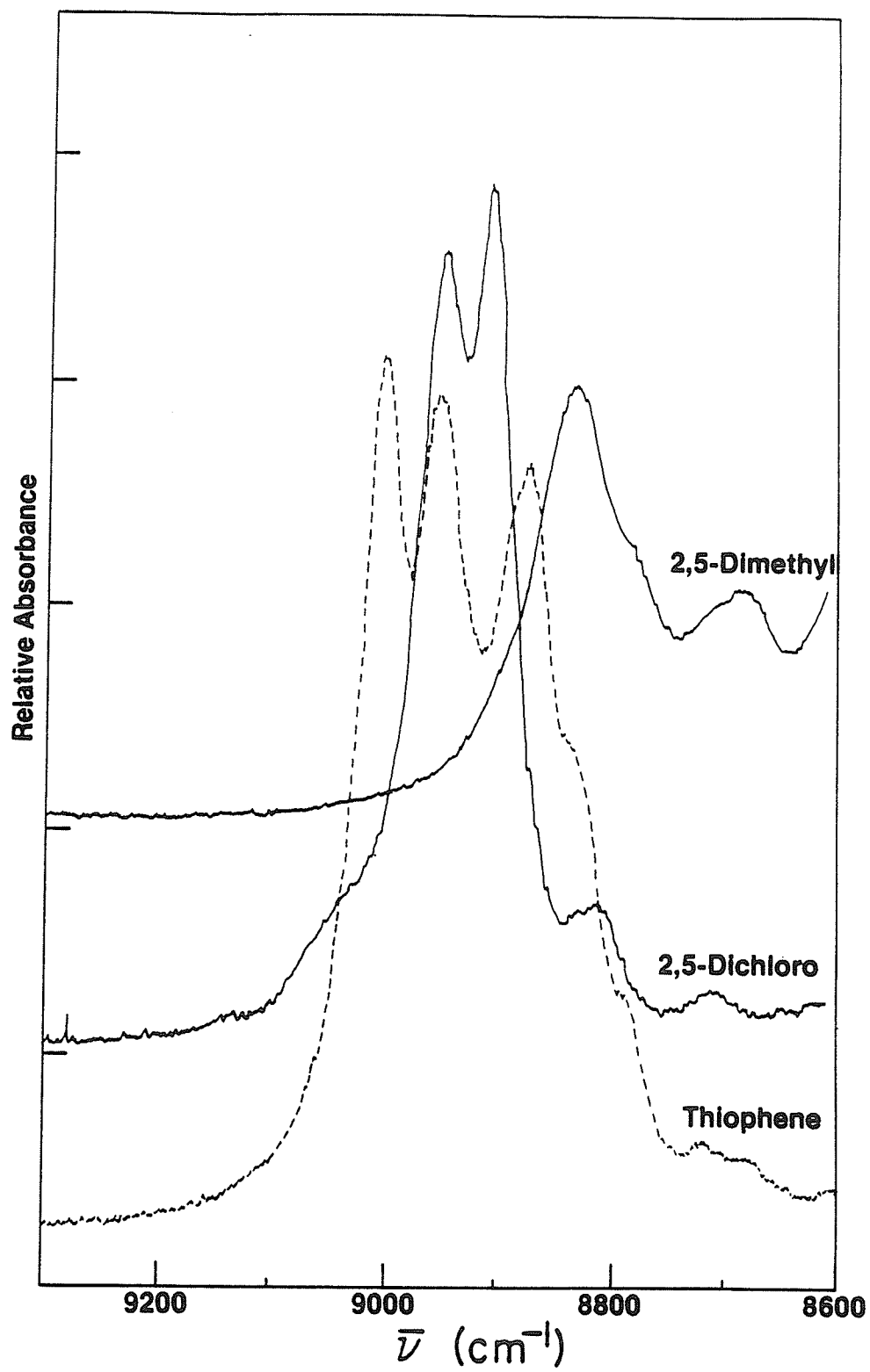


**FIGURE 10.5**

Liquid phase overtone absorption spectrum of 2,5 diclorothiophene and 2,5 dimethylthiophene overlayed on the thiophene spectrum in the  $\Delta\nu_{\text{CH}} = 3$  region. A sample cell pathlength of 5 cm was used.



$\Delta\nu_{\text{CH}} = 3$  spectra of thiophene and 3,4 dibromo-thiophene the lower intensity Fermi peak is on the low energy side of the doublet. The  $\Delta\nu_{\text{CH}} = 3$  spectra of 2,5 dibromo and 2,5 dimethylthiophene consist of a single major peak closely corresponding to the lower energy peak appearing in the parent molecule spectrum. However, a Fermi doublet feature appears in the  $\Delta\nu_{\text{CH}} = 3$  spectrum of 2,5 dichlorothiophene. Now the lower intensity peak is on the high energy side of the Fermi doublet.

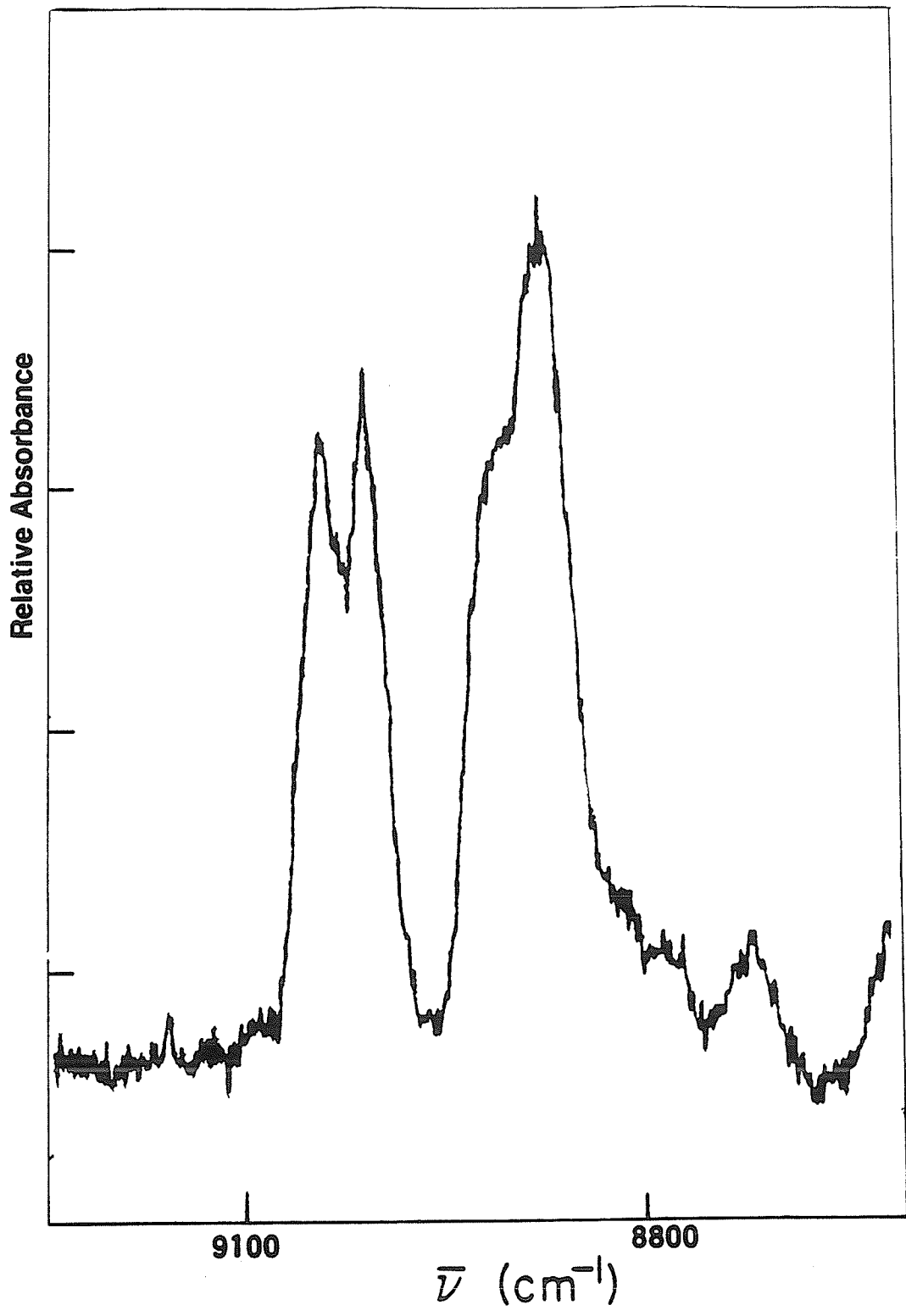
In the previous Chapter, the effects of substitution on the frequency and anharmonicity of the aryl CH stretching modes were discussed. Halogens tend to increase the frequency of CH oscillators adjacent to the site of substitution. The substituent induced shift in overtone position due to chlorine was found to be greater than bromine. Methyl groups shifted the overtone position to lower energy by decreasing the oscillator frequency. The decreased doublet splitting in 3,4 dibromo compared to thiophene is a result of the small substituent induced overtone shift to higher energy which slightly detunes the Fermi interaction. In 2,5 dichlorothiophene, the chlorine substituent effect is large enough to shift the overtone into near resonance with the Fermi state. Note that the intensity

distribution of the doublet is consistent with this explanation. The substituent induced overtone frequency shift of bromine is small enough that no Fermi doublet appears in the spectrum of 2,5 dibromothiophene. In 2,5 dimethylthiophene the substituent induced shift is in the opposite direction, and the aryl overtone is well out of resonance with the Fermi state. However, the Fermi resonance is operative in the monomethylthiophenes. The high energy overtone which is absent in the symmetrically 2,5 disubstituted species appears as a Fermi doublet at  $\Delta\nu_{\text{CH}} = 3$  (see Figure 10.6). The point to note from this preliminary discussion is that the Fermi resonance patterns are easily understood in terms of the established frequency shift characteristics of the various substituents.

These results clearly show the sensitivity of the non-zero order overtone features to substitution. Resonance tuning in the  $\Delta\nu_{\text{CH}}=3$  region is particularly evident in the spectra of the substituted thiophenes. The sensitivity of the thiophene features to the resonance condition is inconsistent with the RSH interpretation. The dramatic "tuning-in" and "tuning-out" of the effect along the overtone progression or with substitution is consistent with very mode specific interactions rather than the diffuse interaction

**FIGURE 10.6**

Gas phase overtone spectrum of 2 methylthiophene in the  $\Delta\nu_{\text{CH}} = 3$  region. The 2 methylthiophene spectrum was measured at a pressure of 18 Torr with a 9.75 m pathlength cell.

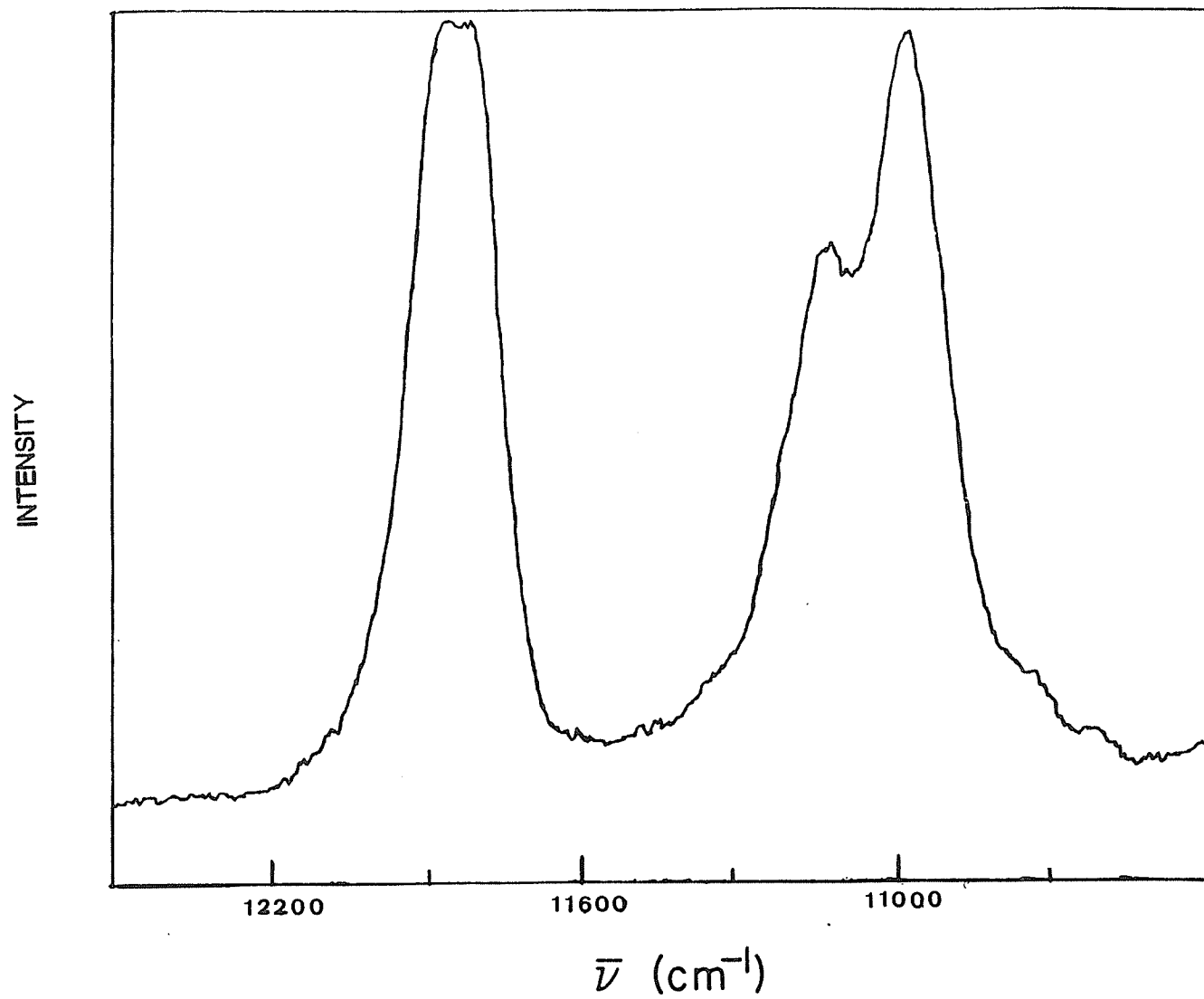


interpretation of RSH. Differing degrees of frequency and anharmonicity between the specific interacting modes tend to move the various Fermi states in and out of resonance as a function of the energy or substitution resulting in the "tuning-in" and "tuning-out" effect.

The difference in behaviour between furan and thiophene generates many interesting questions. The spectroscopic results seem to suggest different IVR dynamics between furan and thiophene despite their similarities. The  $\Delta\nu_{CH} = 3 - 6$  overtone regions of furan like those of benzene and neopentane seem best described by the RSH interpretation of the "large" molecule limit. No features with the characteristic Fermi doublet structure appear in the furan overtone spectrum. Coalescence of the overtone features at  $\Delta\nu_{CH} = 4$  is relatively insensitive to substitution. The liquid phase  $\Delta\nu_{CH} = 4$  and 5 aryl regions of 2-methylfuran are reported in Figures 10.7 and 10.8. In contrast to the furans, the thiophenes appear to behave much like small molecules in the  $\Delta\nu_{CH} = 1 - 6$  regions. Spectral perturbations in the  $\Delta\nu_{CH} = 3$  and 5 regions are highly sensitive to substitution and differ between the liquid and gas phase. This suggests that a much more mode selective interaction is operative in

**FIGURE 10.7**

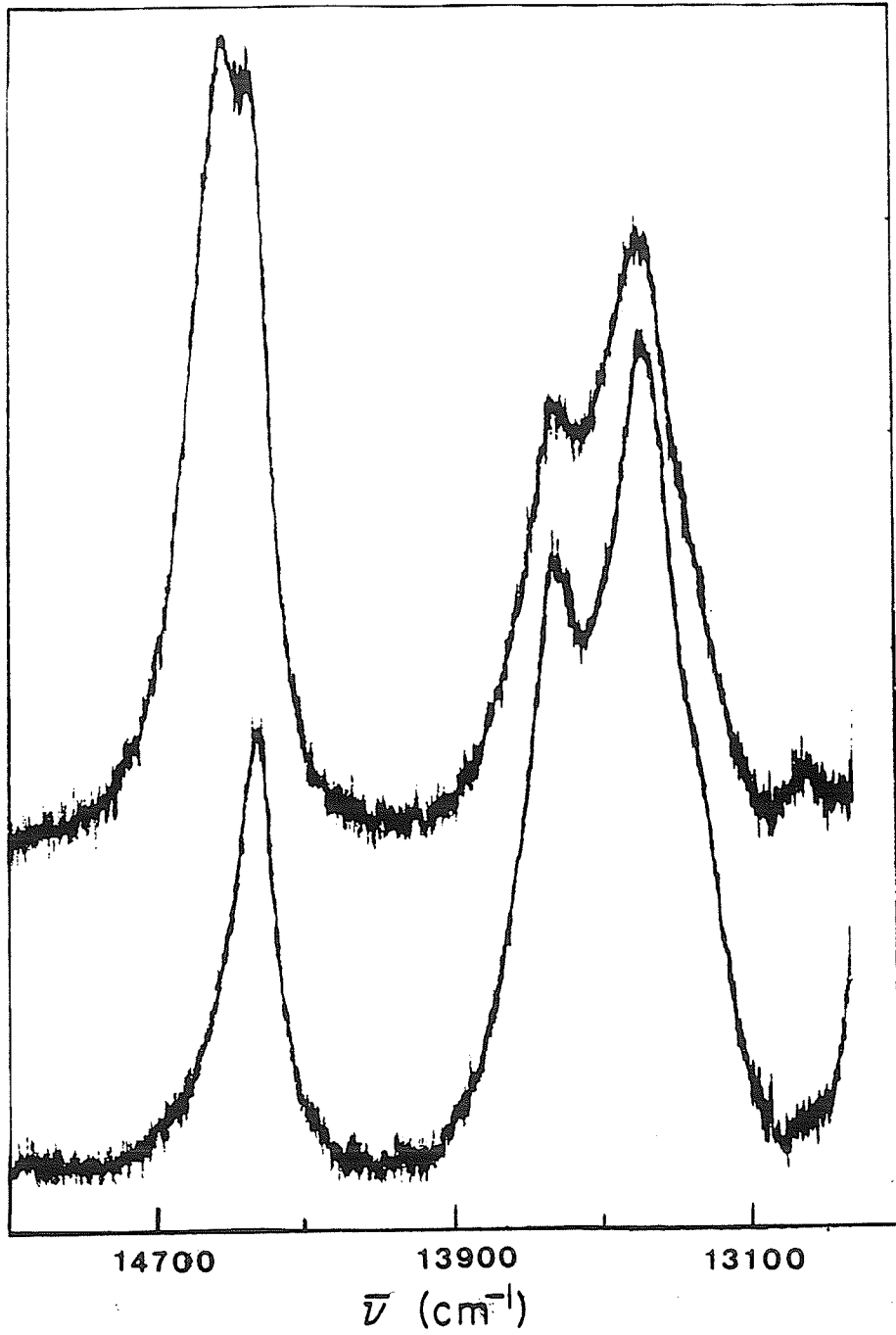
Liquid phase overtone absorption spectrum of 2-methylfuran in the  $\Delta\nu_{\text{CH}} = 4$  region. A sample cell pathlength of 10 cm was used.



**FIGURE 10.8**

Liquid phase overtone absorption spectra of 2 methylfuran (top trace) and 2,5 dimethylfuran (bottom trace) in the  $\Delta\nu_{\text{CH}} = 5$  region. Sample cell pathlengths of 10 cm were used.

Relative Absorbance



the thiophenes. The question remains, what are the interacting zero order states? With the available thiophene force field data, there are no obvious near resonance matches between zero order overtone states and combinations involving overtones of the mid-frequency modes built on overtone states of the next lower manifold. Even if combinations involving two mid-frequency modes are included as prospective "door-way" states, no dramatic resonance match is apparent at  $\Delta\nu_{CH} = 3$  and 5. If the experimental thiophene harmonic force field is deficient in the mid-frequency region or the mid-frequency modes have a higher anharmonicity than usual, the absence of a resonance match at  $\Delta\nu_{CH} = 3$  and 5 can be explained. It is also very likely that the overtone dynamics are much more complicated than existing models suggest.